

Cosmology with cosmic shear observations: a review

Martin Kilbinger

Laboratoire AIM, CEA Saclay - CNRS - Paris 6, Irfu/SAP, F-91191 Gif-sur-Yvette, France

E-mail: martin.kilbinger@cea.fr

Abstract.

Cosmic shear is the distortion of images of distant galaxies due to weak gravitational lensing by the large-scale structure in the Universe. Such images are coherently deformed by the tidal field of matter inhomogeneities along the line of sight. By measuring galaxy shape correlations, we can study the properties and evolution of structure on large scales as well as the geometry of the Universe. Thus, cosmic shear has become a powerful probe into the nature of dark matter and the origin of the current accelerated expansion of the Universe. Over the last years, cosmic shear has evolved into a reliable and robust cosmological probe, providing measurements of the expansion history of the Universe and the growth of its structure.

We review here the principles of weak gravitational lensing and show how cosmic shear is interpreted in a cosmological context. Then we give an overview of weak-lensing measurements, and present the main observational cosmic-shear results since it was discovered 15 years ago, as well as the implications for cosmology. We then conclude with an outlook on the various future surveys and missions, for which cosmic shear is one of the main science drivers, and discuss promising new weak cosmological lensing techniques for future observations.

Keywords: weak gravitational lensing, cosmology, large-scale structure of the universe

Contents

1	Introduction	3
2	Cosmological background	4
2.1	Standard cosmological model	4
2.2	Structure formation	5
2.3	Modified gravity models	6
3	Weak cosmological lensing formalism	7
3.1	Light deflection and the lens equation	7
3.2	Light propagation in the universe	7
3.3	Linearized lensing quantities	8
3.4	Projected overdensity	10
3.5	Estimating shear from galaxies	11
3.6	E- and B-modes	11
3.7	The lensing power spectrum	12
3.8	The shear correlation function	14
3.9	Derived second-order functions	15
3.9.1	E-/B-mode mixing	17
3.10	Shear tomography and 3D lensing	17
3.10.1	Tomographic redshift binning	18
3.10.2	3D lensing	19

3.11	Intrinsic alignment	19
3.12	Galaxy-galaxy lensing	20
3.13	The lensing bispectrum	22
3.14	Higher-order corrections	23
3.15	Weak-lensing mass maps	24
4	Numerical simulations	25
4.1	The necessity of simulations for weak lensing	25
4.2	Principles of ray-shooting and ray-tracing	26
4.2.1	Projecting the density field	26
4.2.2	Tracing the photons	26
4.2.3	Approximations	27
4.2.4	Further methods	27
4.2.5	Full-sky lensing simulations	27
4.3	Dark matter and hydro-dynamical simulations	27
4.4	Baryonic effects on lensing observables	28
5	Cosmology from cosmic shear	28
5.1	Covariance estimation	28
5.1.1	The Gaussian approximation	29
5.1.2	Non-Gaussian contributions	29
5.2	The likelihood function	30
5.3	Parameter estimation	31
6	Measuring weak lensing	32
6.1	Data analysis methods for weak lensing	32
6.2	Galaxy shape measurement	32
6.2.1	Direct estimation methods	33
6.2.2	Model-fitting methods	34
6.2.3	Further approaches	34
6.2.4	Shape measurement biases	35
6.3	PSF correction	35
6.3.1	The PSF model	36
6.3.2	Colour effects	36
6.4	Image simulations	37
6.5	Photometric redshifts	37
6.6	Error modelling and residual systematics	39
7	Observational results and cosmological constraints	39
7.1	Basic results	39
7.1.1	Early era, 2000 - 2006	39
7.1.2	Consolidating era, 2007 - 2012	42
7.1.3	Survey era, 2013 - present	43
7.2	Third-order correlations	47
7.3	Follow-up publications	47
7.4	Convergence and mass maps	48
7.5	3D lensing	48
7.6	Other weak-lensing techniques in a cosmological context	49

7.6.1	Shear-ratio geometry test	49
7.6.2	Galaxy-galaxy lensing	49
7.7	Intrinsic alignment	50
8	Future cosmic shear expectations and forecasts	51
8.1	Upcoming and future surveys	51
8.1.1	Ground-based surveys	51
8.1.2	Space-based surveys	52
8.1.3	Further ideas	53
8.2	Radio lensing	53
8.3	3D mass reconstruction	53
8.4	Magnification	54
8.5	Cosmic flexion	55
8.6	Peak statistics	55
8.7	Outlook	56
	References	57

1. Introduction

On May, 29, 1919, during a solar eclipse, the deflection of light rays of stars due to the Sun’s gravitational field was measured (Dyson et al. 1920), marking the first successful test of the theory of general relativity (GR; Einstein 1916). Then, the first discovery of extra-galactic gravitational lensing was obtained in 1979, with the detection of a doubly-imaged quasar lensed by a galaxy (Walsh et al. 1979). Lensing distortions have been known since 1987 with the observation of giant arcs — strongly distorted galaxies behind massive galaxy clusters (Soucail et al. 1987). Three years later in 1990, weak gravitational lensing was detected for the first time as statistical tangential alignments of galaxies behind massive clusters (Tyson et al. 1990). It took another 10 years until, in 2000, coherent galaxy distortions were measured in blind fields, showing the existence of weak gravitational lensing by the large-scale structure, or cosmic shear (Bacon et al. 2000, Kaiser et al. 2000, Van Waerbeke et al. 2000, Wittman et al. 2000). And so, nearly 100 years after its first measurement, the technique of gravitational lensing has evolved into a powerful tool for challenging GR on cosmological scales.

All observed light from distant galaxies is subject to gravitational lensing. This is because light rays propagate through a universe that is inhomogeneous due to the ubiquitous density fluctuations at large scales. These fluctuations create a tidal gravitational field that causes light bundles to be deflected differentially. As a result, images of light-emitting galaxies that we observe are distorted. The direction and amount of distortion is directly related to the size and shape of the matter distribution projected along the line of sight. The deformation of high-redshift galaxy images in random lines of sight therefore provides a measure of the large-scale structure (LSS) properties, which consists of a network of voids, filaments, and halos. The larger the amplitude of the inhomogeneity of this cosmic web is, the larger the deformations are. This technique of *cosmic shear*, or *weak cosmological lensing* is the topic of this review.

The typical distortions of high-redshift galaxies by the cosmic web are on the order of a few percent, much smaller than the width of the intrinsic shape and size distribution. Thus, for an individual galaxy, the lensing effect is not detectable, placing cosmic shear into the regime of *weak gravitational lensing*. The presence of a tidal field acting as a gravitational lens results in a coherent

alignment of galaxy image orientations. This alignment can be measured statistically as a correlation between galaxy shapes.

Cosmic shear is a very versatile probe of the LSS. It measures the clustering of the LSS from the highly non-linear, non-Gaussian sub-megaparsec (Mpc) regime, out to very large, linear scales of more than a hundred Mpc. By measuring galaxy shape correlations between different redshifts, the evolution of the LSS can be traced, enabling us to detect the effect of dark energy on the growth of structure. Together with the ability to measure the geometry of the Universe, cosmic shear can potentially distinguish between dark energy and modified gravity theories (Hu 1999). Since gravitational lensing is not sensitive to the dynamical state of the intervening masses, it yields a direct measure of the total matter, dark plus luminous. By adding information about the distribution of galaxies, cosmic shear can shed light on the complex relationship between galaxies and dark matter.

Since the first detection over a few square degrees of sky area a decade and a half ago, cosmic shear has matured into an important tool for cosmology. Current surveys span hundreds of square degrees, and thousands of square degrees more to be observed in the near future. Cosmic shear is a major science driver of large imaging surveys from both ground and space.

Various past reviews of weak gravitational lensing have covered the topic of this review, e.g. Bartelmann & Schneider (2001), Schneider et al. (2006), Hoekstra & Jain (2008), Munshi et al. (2008), and Bartelmann (2010). Here, we will present derivations of much of the basics of weak cosmological lensing, then give an overview of the results of cosmic shear observations along with their implications for cosmology.

2. Cosmological background

This section provides a very brief overview of the cosmological concepts and equations relevant for cosmic shear. Detailed derivations of the following equations can be found in standard cosmology textbooks, e.g. Peebles (1980), Coles & Lucchin (1996), Dodelson (2003).

2.1. Standard cosmological model

In the standard cosmological model, the field equations of General Relativity (GR) describe the relationship between space-time geometry and the matter-energy content of the Universe governed by gravity. A solution to these non-linear differential equations exists representing a homogeneous and isotropic universe.

To quantify gravitational lensing, however, we need to consider light propagation in an inhomogeneous universe. For a general metric that describes an expanding universe including first-order perturbations, the line element ds is given as

$$ds^2 = \left(1 + \frac{2\Psi}{c^2}\right) c^2 dt^2 - a^2(t) \left(1 - \frac{2\Phi}{c^2}\right) dl^2, \quad (1)$$

where the scale factor a is a function of cosmic time t (we set a to unity at present time $t = t_0$), and c is the speed of light. The spatial part of the metric is given by the comoving coordinate l , which remains constant as the Universe expands. The two Bardeen gravitational potentials Ψ and Φ are considered to describe weak fields, $\Psi, \Phi \ll c^2$. The potential of a lens with mass M and radius R can be approximated by $GM/R = (c^2/2)(R_S/R)$, where G is Newton's gravitational constant and R_S is the Schwarzschild radius. The weak-field condition is fulfilled for most mass distributions, excluding only those very compact objects whose extent R is comparable to their Schwarzschild radius.

In GR, and in the absence of anisotropic stress which is the case on large scales, the two potentials are equal, $\Psi = \Phi$. If the perturbations vanish, (1) reduces to the Friedmann-Lemaître-Robertson-Walker (FLRW) metric.

The spatial line element dl^2 can be separated into a radial and angular part, $dl^2 = d\chi^2 + f_K^2(\chi)d\omega$. Here, χ is the comoving coordinate and f_K is the comoving angular distance, the functional form of which is given for the three distinct cases of three-dimensional space with curvature K as

$$f_K(\chi) = \begin{cases} K^{-1/2} \sin(K^{1/2}\chi) & \text{for } K > 0 \text{ (spherical)} \\ \chi & \text{for } K = 0 \text{ (flat)} \\ (-K)^{-1/2} \sinh[(-K)^{1/2}\chi] & \text{for } K < 0 \text{ (hyperbolic)}. \end{cases} \quad (2)$$

that are characterised by their corresponding equation-of-state relation between pressure p and density ρ , given by the parameter w as

$$p = w c^2 \rho. \quad (3)$$

The present-day density of each species is further scaled by the present-day critical density of the Universe $\rho_{c,0} = 3H_0^2/(8\pi G)$, for which the Universe has a flat geometry. The Hubble constant $H_0 = H(a=1) = (\dot{a}/a)_{t=t_0} = 100 h \text{ km s}^{-1} \text{ Mpc}^{-1}$ denotes the present-day value of the Hubble parameter H , and the parameter $h \sim 0.7$ characterizes the uncertainty in our knowledge of H_0 . The density parameter of non-relativistic matter is $\Omega_m = \rho_{m,0}/\rho_{\text{crit},0}$, which consists of cold dark matter (CDM), baryonic matter, and possibly heavy neutrinos as $\Omega_m = \Omega_c + \Omega_b + \Omega_\nu$ †. Relativistic matter (Ω_r) consists of photons, with the main contributors being the cosmic microwave background (CMB) radiation, and light neutrinos. Finally, the component driving the accelerated expansion (“dark energy”) is denoted by Ω_{de} . Lacking a well-motivated physical model, the dark-energy equation-of-state parameter w is often parametrized by the first or first few coefficients of a Taylor expansion, e.g. $w(a) = w_0 + w_1(1-a)$ (Chevallier & Polarski 2001, Linder 2003). In the case of the cosmological constant, $\Omega_{\text{de}} \equiv \Omega_\Lambda$ and $w = -1$.

The sum of all density parameters defines the *curvature density parameter* Ω_K , with $\Omega_m + \Omega_{\text{de}} + \Omega_r = 1 - \Omega_K$, where $\Omega_K = -(c/H_0)^2 K$ has opposite sign compared to the curvature K .

Alternative parametrizations of the density of a species x are the *physical density parameters*, which are defined as $\omega_x = \Omega_x h^2$.

2.2. Structure formation

In an expanding universe, density fluctuations evolve with time. Tiny quantum fluctuations in the primordial inflationary cosmos generate small-amplitude density fluctuations. Subsequently, these fluctuations grow into the large structures we see today, in the form of clusters, filaments, and galaxy halos.

At early enough times or on large enough scales, those density fluctuations are small, and their evolution can be treated using linear perturbation theory. Once those fluctuations grow to become non-linear, other approaches to describe them are necessary — for example higher-order perturbation theory, renormalization group mechanisms, analytical models of gravitational collapse, the so-called halo model, or N -body simulations (see Sect. 4).

Fluctuations of the density ρ around the mean density $\bar{\rho}$ are parametrized by the density contrast

$$\delta = \frac{\rho - \bar{\rho}}{\bar{\rho}}. \quad (4)$$

For non-relativistic perturbations in the matter-dominated era on scales smaller than the horizon, i.e. the light travel distance since $t = 0$, Newtonian physics suffices to describe the evolution of δ (Peebles 1980). The density contrast of an ideal fluid of zero pressure is related to the gravitational potential via the Poisson equation,

$$\nabla^2 \Phi = 4\pi G a^2 \bar{\rho} \delta. \quad (5)$$

† Unless written as function of a , density parameters are interpreted at present time; the subscript ‘0’ is omitted.

The differential equation describing the evolution of δ typically has to be solved numerically, although in special cases analytical solutions exist. The solution that increases with time is called *growing mode*. The time-dependent function is the *linear growth factor* D_+ , which relates the density contrast at time a to an earlier, initial epoch a_i , with $\delta(a) \propto D_+(a)\delta(a_i)$. In a matter-dominated Einstein-de-Sitter Universe, D_+ is proportional to the scale factor a . The presence of dark energy results in a suppressed growth of structures.

In the early Universe, when radiation is the dominant species, perturbations with comoving scales smaller than the horizon do not grow. Super-horizon perturbations grow as $\delta \propto a^2$ until the time when, due to the expansion of the Universe, these perturbations “enter the horizon”. This leads to a difference of growth as a function of perturbation scale, which is quantified in the transfer function T , expressed as a function of the scale k in Fourier space. T describes the evolution of the density contrast at scale k compared to the super-horizon case at an arbitrary large scale $k = 0$ (Eisenstein & Hu 1998),

$$T(k) = \left(\frac{\tilde{\delta}(k, a = 1)}{\tilde{\delta}(k, a_i)} \right) / \left(\frac{\tilde{\delta}(k = 0, a = 1)}{\tilde{\delta}(k = 0, a_i)} \right). \quad (6)$$

Here, the tilde denotes Fourier transform. On large scales, $T(k \rightarrow 0)$ approaches unity, since at early enough time all perturbations live outside the horizon. At small scales, $T(k) \propto k^{-2}$. The details of this function depend on the matter content and its equation of state (3) (Bardeen et al. 1986, Sugiyama 1995, Eisenstein & Hu 1998).

2.3. Modified gravity models

A very general, phenomenological characterisation of deviations from GR is to add parameters to the Poisson equation, and to treat the two Bardeen potentials as two independent quantities. This leads to two modified, distinct Poisson equations, which, expressed in Fourier space, are (Uzan 2007, Amendola et al. 2008)

$$k^2 \tilde{\Psi}(k, a) = 4\pi G a^2 [1 + \mu(k, a)] \rho \tilde{\delta}(k, a); \quad (7)$$

$$k^2 [\tilde{\Phi}(k, a) + \tilde{\Psi}(k, a)] = 8\pi G a^2 [1 + \Sigma(k, a)] \rho \tilde{\delta}(k, a). \quad (8)$$

Non-zero values of the free functions μ and Σ represent deviations from GR. This flexible parametrization can account for a variety of modified gravity models, for example a change in the gravitational force from models with extra-dimensions as in DGP (Dvali, Gabadadze & Porrati 2000), massive gravitons (Zhytnikov & Nester 1994), $f(R)$ extensions of the Einstein-Hilbert action (de Felice & Tsujikawa 2010), or Tensor-Vector-Scalar (TeVeS) theories (Skordis 2009). Non-zero anisotropic stress is predicted from a variety of higher-order gravity theories, but also expected from models of clustered dark energy (Hu 1998, Calabrese et al. 2011). See Clifton et al. (2012) and Yoo & Watanabe (2012) for further models of modified gravity.

The above-introduced parametrization has the advantage of separating the effect of the metric on non-relativistic particles (which are influenced by density fluctuations through (7)), and light deflection (which is governed by both geometry and density fluctuations via (8), see e.g. Uzan & Bernardeau (2001), Jain & Zhang (2008)). Thus, data from galaxy clustering, redshift-space distortions, and velocity fields (testing the former relation on the one hand) and weak-lensing observations (testing the latter equation on the other hand) are complementary in their ability to constrain modified gravity models.

Alternative parametrizations for modifying GR have also been used, such as: the ratio of potentials $\zeta = 1 - \Phi/\Psi$ (“gravitational slip”); the growth index γ defined by $d \ln D_+ / d \ln a = \Omega_m^\gamma(a)$; the parameter E_G , which is a galaxy-bias-independent ratio of the matter–galaxy correlation, the

galaxy auto-correlation, and the redshift distortion parameter β (Zhang et al. 2007). All those parametrizations can be expressed in terms of μ and Σ (Simpson et al. 2013).

3. Weak cosmological lensing formalism

This section introduces the basic concepts of cosmic shear, and discusses the relevant observables and their relationships to theoretical models of the large-scale structure. More details about those concepts can be found in e.g. Bartelmann & Schneider (2001).

3.1. Light deflection and the lens equation

There are multiple ways to derive the equations describing the deflection of light rays in the presence of massive bodies. An intuitive approach is the use of Fermat's principle of minimal light travel time (Schneider et al. 1992, Schneider 1985, Blandford & Narayan 1986).

Photons propagate on null geodesics, given by a vanishing line element ds . In the case of GR we get the light ray travel time from the metric (1) as

$$t = \frac{1}{c} \int \left(1 - \frac{2\Phi}{c^2} \right) dr, \quad (9)$$

where the integral is along the light path in physical or proper coordinates dr . Analogous to geometrical optics, the potential acts as a medium with variable refractive index $n = 1 - 2\Phi/c^2$ (with $\Phi < 0$), changing the direction of the light path. (This effect is what gives gravitational *lensing* its name.) We can apply Fermat's principle, $\delta t = 0$, to get the Euler-Lagrange equations for the refractive index. Integrating these equations along the light path results in the *deflection angle* $\hat{\alpha}$ defined as the difference between the directions of emitted and received light rays,

$$\hat{\alpha} = -\frac{2}{c^2} \int \nabla_{\perp}^p \Phi dr. \quad (10)$$

The gradient of the potential is taken perpendicular to the light path, with respect to physical coordinates. The deflection angle is twice the classical prediction in Newtonian dynamics if photons were massive particles (von Soldner 1804).

3.2. Light propagation in the universe

In this section we quantify the relation between light deflection and gravitational potential on cosmological scales. To describe differential propagation of rays within an infinitesimally thin light bundle, we consider the difference between two neighbouring geodesics, which is given by the *geodesic deviation equation*. In a homogeneous FLRW Universe, the transverse comoving separation \mathbf{x}_0 between two light rays as a function of comoving distance from the observer χ is proportional to the comoving angular distance

$$\mathbf{x}_0(\chi) = f_K(\chi)\boldsymbol{\theta}, \quad (11)$$

where the separation vector \mathbf{x}_0 is seen by the observer under the (small) angle $\boldsymbol{\theta}$ (Schneider et al. 1992, Seitz et al. 1994).

This separation vector is modified by density perturbations in the Universe. We have already seen (10) that a light ray is deflected by an amount $d\hat{\alpha} = -2/c^2 \nabla_{\perp} \Phi(\mathbf{x}, \chi') d\chi'$ in the presence of the potential Φ at distance χ' from the observer. Note that this equation is now expressed in a comoving frame, as well as the gradient. From the vantage point of the deflector the induced change in separation vector at source comoving distance χ is $d\mathbf{x} = f_K(\chi - \chi') d\hat{\alpha}$ (see Fig. 1 for a sketch). The total separation is obtained by integrating over the line of sight along χ' . Lensing deflections

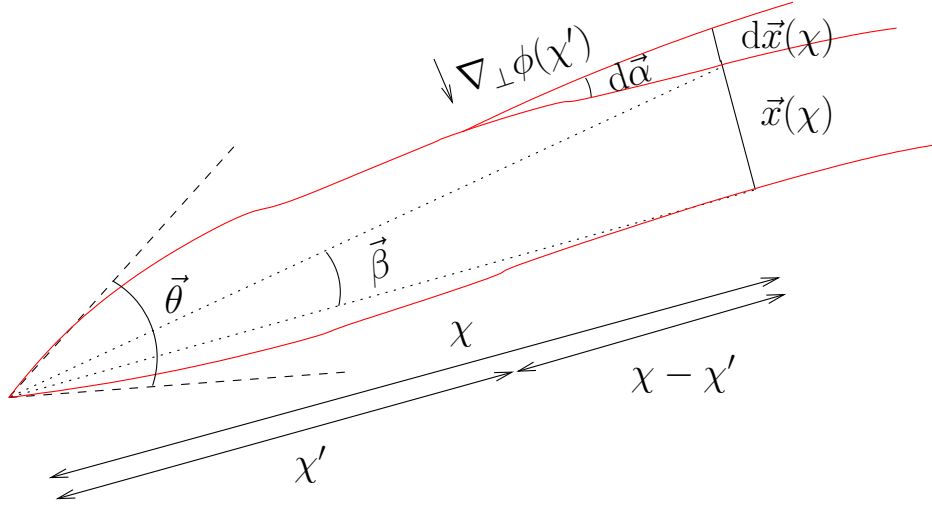


Figure 1. Propagation of two light rays (red solid lines), converging on the observer on the left. The light rays are separated by the transverse comoving distance \mathbf{x} , which varies with distance χ from the observer. An exemplary deflector at distance χ' perturbs the geodesics proportional to the transverse gradient $\nabla_{\perp}\phi$ of the potential. The dashed lines indicate the apparent direction of the light rays, converging on the observer under the angle θ . The dotted lines show the unperturbed geodesics, defining the angle β under which the unperturbed transverse comoving separation \mathbf{x} is seen.

modify the path of both light rays, and we denote with the superscript (0) the potential along the second, fiducial ray. The result is

$$\mathbf{x}(\chi) = f_K(\chi)\boldsymbol{\theta} - \frac{2}{c^2} \int_0^{\chi} d\chi' f_K(\chi - \chi') [\nabla_{\perp}\Phi(\mathbf{x}, \chi'), \chi'] - \nabla_{\perp}\Phi^{(0)}(\chi'). \quad (12)$$

In the absence of lensing the separation vector \mathbf{x} would be seen by the observer under an angle $\beta = \mathbf{x}(\chi)/f_K(\chi)$. The difference between the apparent angle θ and β is the total, scaled deflection angle α , defining the *lens equation*

$$\beta = \theta - \alpha, \quad (13)$$

with

$$\alpha = \frac{2}{c^2} \int_0^{\chi} d\chi' \frac{f_K(\chi - \chi')}{f_K(\chi)} [\nabla_{\perp}\Phi(\mathbf{x}, \chi'), \chi'] - \nabla_{\perp}\Phi^{(0)}(\chi'). \quad (14)$$

Equation (13) is analogous to the standard lens equation in the case of a single, thin lens, in which case β is the source position.

3.3. Linearized lensing quantities

The integral equation (12) can be approximated by substituting the separation vector \mathbf{x} in the integral by the 0th-order solution $\mathbf{x}_0(\chi) = f_K(\chi)\boldsymbol{\theta}$ (11). This corresponds to integrating the potential gradient along the unperturbed ray, which is called the *Born approximation* (see Sect. 3.14 for higher-order corrections). Further, we linearise the lens equation (13) and define the (inverse) amplification matrix as the Jacobian $\mathbf{A} = \partial\beta/\partial\theta$, which describes a linear mapping from lensed (image) coordinates $\boldsymbol{\theta}$ to unlensed (source) coordinates β ,

$$\begin{aligned} A_{ij} &= \frac{\partial\beta_i}{\partial\theta_j} = \delta_{ij} - \frac{\partial\alpha_i}{\partial\theta_j} \\ &= \delta_{ij} - \frac{2}{c^2} \int_0^{\chi} d\chi' \frac{f_K(\chi - \chi')f_K(\chi')}{f_K(\chi)} \frac{\partial^2}{\partial x_i \partial x_j} \Phi(f_K(\chi')\boldsymbol{\theta}, \chi'). \end{aligned} \quad (15)$$

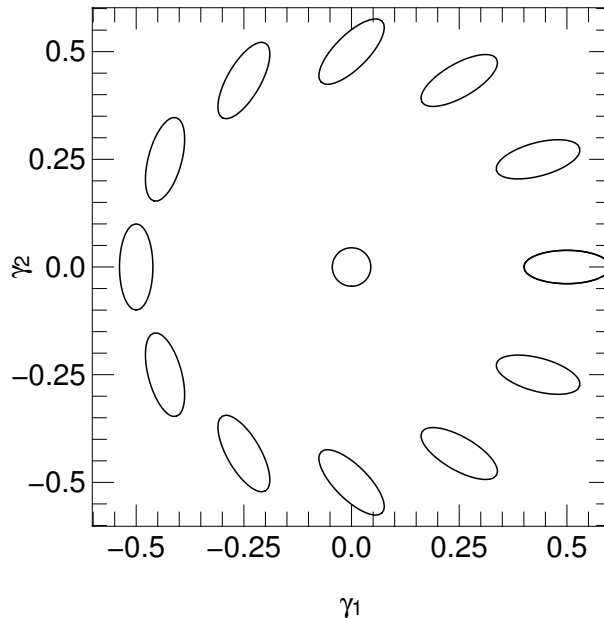


Figure 2. The orientation of the ellipses given by the Cartesian coordinates γ_1 and γ_2 of the shear. While the polar angle φ passes through the range $[0; 2\pi]$, the shear ellipse rotates around π .

The second term in (14) drops out since it does not depend on the angle $\boldsymbol{\theta}$.

In this approximation the deflection angle can be written as the gradient of a 2D potential, the *lensing potential* ψ ,

$$\psi(\boldsymbol{\theta}, \chi) = \frac{2}{c^2} \int_0^\chi d\chi' \frac{f_K(\chi - \chi')}{f_K(\chi)f_K(\chi')} \Phi(f_K(\chi')\boldsymbol{\theta}, \chi'). \quad (16)$$

With this definition, the Jacobi matrix can be expressed as

$$A_{ij} = \delta_{ij} - \partial_i \partial_j \psi, \quad (17)$$

where the partial derivatives are understood with respect to $\boldsymbol{\theta}$. The symmetrical matrix \mathbf{A} is parametrized in terms of the scalar *convergence*, κ , and the two-component spin-two *shear*, $\boldsymbol{\gamma} = (\gamma_1, \gamma_2)$, as

$$\mathbf{A} = \begin{pmatrix} 1 - \kappa - \gamma_1 & -\gamma_2 \\ -\gamma_2 & 1 - \kappa + \gamma_1 \end{pmatrix}. \quad (18)$$

This defines the convergence and shear as second derivatives of the potential,

$$\kappa = \frac{1}{2} (\partial_1 \partial_1 + \partial_2 \partial_2) \psi = \frac{1}{2} \nabla^2 \psi; \quad \gamma_1 = \frac{1}{2} (\partial_1 \partial_1 - \partial_2 \partial_2) \psi; \quad \gamma_2 = \partial_1 \partial_2 \psi. \quad (19)$$

The inverse Jacobian \mathbf{A}^{-1} describes the local mapping of the source light distribution to image coordinates. The convergence, being the diagonal part of the matrix, is an isotropic increase or decrease of the observed size of a source image. Shear, the trace-free part, quantifies an anisotropic stretching, turning a circular into an elliptical light distribution.

It is mathematically convenient to write the shear as complex number, $\boldsymbol{\gamma} = \gamma_1 + i\gamma_2 = |\boldsymbol{\gamma}| \exp(2i\varphi)$, with φ being the polar angle between the two shear components. Shear transforms as a spin-two quantity: a rotation about π is the identity transformation of an ellipse (see Fig. 2 for an illustration).

In the context of cosmological lensing by large-scale structures, images are very weakly lensed, and the values of κ and $\boldsymbol{\gamma}$ are on the order of a few percent or less. Each source is mapped uniquely onto one image, there are no multiple images, and the matrix \mathbf{A} is indeed invertible.

We can factor out $(1 - \kappa)$ from \mathbf{A} (18), since this multiplier only affects the size but not the shape of the source. Cosmic shear is based on the measurement of galaxy shapes (see Sect. 6.2), and therefore the observable in question is not the shear γ but the *reduced shear*,

$$g = \frac{\gamma}{1 - \kappa}, \quad (20)$$

which has the same spin-two transformation properties as shear. Weak lensing is the regime where the effect of gravitational lensing is very small, with both the convergence and the shear much smaller than unity. Therefore, shear is a good approximation of reduced shear to linear order (see Sect. 3.14 for its validity). Magnification, which is an estimator of κ , will be discussed in Sect. 8.4.

3.4. Projected overdensity

Since the convergence κ is related to the lensing potential ψ (16) via a 2D Poisson equation (19), it can be interpreted as a (projected) surface density. To introduce the 3D density contrast δ , we apply the 2D Laplacian of the lensing potential (16) to the 3D potential Φ and add the second-order derivative along the comoving coordinate, $\partial^2/\partial\chi^2$. This additional term vanishes, since positive and negative contributions cancel out to a good approximation when integrating along the line of sight. Next, we replace the 3D Laplacian of Φ with the over-density δ using the Poisson equation (5), and $\bar{\rho} \propto a^{-3}$. Writing the mean matter density in terms of the critical density, we get

$$\kappa(\boldsymbol{\theta}, \chi) = \frac{3H_0^2\Omega_m}{2c^2} \int_0^\chi \frac{d\chi'}{a(\chi')} \frac{f_K(\chi - \chi')}{f_K(\chi)} f_K(\chi') \delta(f_K(\chi')\boldsymbol{\theta}, \chi'). \quad (21)$$

This expression is a projection of the density along comoving coordinates, weighted by geometrical factors involving the distances between source, deflector, and observer. In the case of a flat universe, the geometrical weight $(\chi - \chi')\chi'$ is a parabola with maximum at $\chi' = \chi/2$. Thus, structures at around half the distance to the source are most efficient to generate lensing distortions.

The mean convergence from a population of source galaxies is obtained by weighting the above expression with the galaxy probability distribution in comoving distance, $n(\chi)d\chi$,

$$\kappa(\boldsymbol{\theta}) = \int_0^{\chi_{\text{lim}}} d\chi n(\chi) \kappa(\boldsymbol{\theta}, \chi). \quad (22)$$

The integral extends out to the limiting comoving distance χ_{lim} of the galaxy sample. Inserting (21) into (22) and interchanging the integral order results in the following expression,

$$\kappa(\boldsymbol{\theta}) = \frac{3H_0^2\Omega_m}{2c^2} \int_0^{\chi_{\text{lim}}} \frac{d\chi}{a(\chi)} q(\chi) f_K(\chi) \delta(f_K(\chi)\boldsymbol{\theta}, \chi). \quad (23)$$

The lens efficiency q is defined as

$$q(\chi) = \int_\chi^{\chi_{\text{lim}}} d\chi' n(\chi') \frac{f_K(\chi' - \chi)}{f_K(\chi')}, \quad (24)$$

and indicates the lensing strength at a distance χ of the combined background galaxy distribution. Thus, the convergence is a linear measure of the total matter density, projected along the line of sight with dependences on the geometry of the universe via the distance ratios, and the source galaxy distribution $n(\chi)d\chi = n(z)dz$. The latter is usually obtained using photometric redshifts (Sect. 6.5). We will see in Sects. 3.10 and 8.3 how to recover information in the redshift direction.

By construction, the expectation value of shear and convergence are zero, since $\langle\delta\rangle = 0$. The first non-trivial statistical measure of the distribution of κ and γ are second moments. Practical estimators of weak-lensing second-order statistics in real and Fourier-space are discussed in Sects. 3.7 and 3.8.

3.5. Estimating shear from galaxies

In the case of cosmic shear, not the convergence but the shear is measured from the observed galaxy shapes, as discussed in this section. Theoretical predictions of the convergence (23) can be related to the observed shear using the relations (19). Further, a convergence field can be estimated by reconstruction from the observed galaxy shapes, see Sect. 3.15. Alternatively, the convergence can be estimated using *magnification*, as discussed in Sect. 8.4.

We can attribute an intrinsic, complex *source ellipticity* ε^s to a galaxy. Cosmic shear modifies this ellipticity as a function of the complex reduced shear, which depends on the definition of ε^s . If we define this quantity for an image with elliptical isophotes, minor-to-major axis ratio b/a , and position angle ϕ , as $\varepsilon = (a - b)/(a + b) \times \exp(2i\phi)$, the observed ellipticity ε (for $|g| \leq 1$) is given as (Seitz & Schneider 1997)

$$\varepsilon = \frac{\varepsilon^s + g}{1 + g^* \varepsilon^s}. \quad (25)$$

The asterisk “*” denotes complex conjugation. In the weak-lensing regime, this relation is approximated to

$$\varepsilon \approx \varepsilon^s + \gamma. \quad (26)$$

If the intrinsic ellipticity of galaxies has no preferred orientation, the expectation value of ε^s vanishes, $\langle \varepsilon^s \rangle = 0$, and the observed ellipticity is an unbiased estimator of the reduced shear,

$$\langle \varepsilon \rangle = g. \quad (27)$$

This relation breaks down in the presence of intrinsic galaxy alignments (Sect. 3.11).

Another commonly used ellipticity estimator has been proposed by (Schneider & Seitz 1995). This estimator has a slightly simpler dependence on second moments of galaxy images, which have been widely used for shape estimation, see Sect. 6.2. However, it does not provide an unbiased estimator of g , but explicitly depends on the intrinsic ellipticity distribution.

In the weak-lensing regime, the shear cannot be detected from an individual galaxy. With distortions induced by the LSS of the order $\gamma \sim 0.03$, and the typical intrinsic ellipticity rms of $\sigma_\varepsilon = \langle |\varepsilon|^2 \rangle^{1/2} \sim 0.3$, one needs to average over a number of galaxies N of at least a few hundred to obtain a signal-to-noise ratio $S/N = \gamma \times N^{1/2}/\sigma_\varepsilon$ of above unity.

3.6. E- and B-modes

The Born approximation introduced in Sect. 3.3 results in the definition of the convergence and shear to be functions of a single scalar potential (16). The two shear components defined in that way (19) are not independent, and the shear field cannot have an arbitrary form. We can define a vector field \mathbf{u} as the gradient of the “potential” κ , $\mathbf{u} = \nabla \kappa$. By definition, the curl of this gradient vanishes, $\nabla \times \mathbf{u} = \partial_1 u_2 - \partial_2 u_1 = 0$. Inserting the relations between κ, γ and ψ (19) into this equality results in second-derivative constraints for γ . A shear field fulfilling those relations is called an *E-mode* field, analogous to the electric field. In real life however, \mathbf{u} obtained from observed data is in general not a pure gradient field but has a non-vanishing curl component. The corresponding convergence field can be decomposed into its E-mode component, κ^E , and B-mode, κ^B , given by $\nabla^2 \kappa^E = \nabla u$ and $\nabla^2 \kappa^B = \nabla \times u$. The *B-mode* component can have various origins:

- (i) Higher-order terms in the light-propagation equation (12), e.g. lens-lens coupling and integration along the perturbed light path (18) (Krause & Hirata 2010).
- (ii) Other higher-terms beyond usual approximations of relations such as between shear and reduced shear, or between shear and certain ellipticity estimators (see Sect. 6.2) (Krause & Hirata 2010).

- (iii) Lens galaxy selection biases, such as size and magnitude bias (Wyithe et al. 2003, Schmidt et al. 2009a), or clustering of lensing galaxies (Bernardeau 1998, Schneider et al. 2002b).
- (iv) Correlations of the intrinsic shapes of galaxies with each other, and with the structures that induce weak-lensing distortions (intrinsic alignment, Sect. 3.11) (Crittenden et al. 2002).
- (v) Image and data analysis errors such as PSF correction residuals, systematics in the astrometry.

The astrophysical effects (i) - (iv) cause a B-mode at the percent-level compared to the E-mode. The intrinsic alignment B-mode amplitude is the least well-known since the model uncertainty is large (Capranico et al. 2013). Up to now, cosmic shear surveys do not have the statistical power to reliably detect those B-modes. Until recently, the amplitude of a B-mode detection has exclusively been used to assess the quality of the data analysis, assuming that (v) is the only measurable B-mode contributor. While this is a valid approach, it only captures those systematics that create a B-mode. A B-mode non-detection might render an observer over-confident to believe that also the E-mode is uncontaminated by systematics. Further, the ratio of B- to E-mode should not be used to judge the data quality, since this ratio is not cosmology-independent and can bias the cosmological inference of the data.

3.7. The lensing power spectrum

The basic second-order function of the convergence (23) is the two-point correlation function (2PCF) $\langle \kappa(\boldsymbol{\vartheta})\kappa(\boldsymbol{\vartheta} + \boldsymbol{\theta}) \rangle$. The brackets denote ensemble average, which can be replaced by a spatial average over angular positions $\boldsymbol{\vartheta}$. With the assumption that the density field δ on large scales is statistically homogeneous and isotropic, which follows from the cosmological principle, the same holds for the convergence. The 2PCF is then invariant under translation and rotation, and therefore a function of only the modulus of the separation vector between the two lines of sight θ . Expressed in Fourier space, the two-point correlation function defines the convergence power spectrum P_κ with

$$\langle \tilde{\kappa}(\boldsymbol{\ell})\tilde{\kappa}^*(\boldsymbol{\ell}') \rangle = (2\pi)^2 \delta_{\text{D}}(\boldsymbol{\ell} - \boldsymbol{\ell}') P_\kappa(\ell). \quad (28)$$

Here, δ_{D} is the Dirac delta function. The complex Fourier transform $\tilde{\kappa}$ of the convergence is a function of the 2D wave vector $\boldsymbol{\ell}$, the Fourier-conjugate of $\boldsymbol{\theta}$. Again due to statistical homogeneity and isotropy, the power spectrum only depends on the modulus ℓ . For simplicity, we ignore the curvature of the sky in this expression. For lensing on very large scales, and for 3D lensing (Sect. 3.10), the curvature has to be accounted for by more accurate expressions (Loverde & Afshordi 2008), or by applying spherical harmonics instead of Fourier transforms.

If the convergence field is decomposed into an E-mode κ^{E} and B-mode component κ^{B} , two expressions analogous to (28) define the E- and B-mode power spectra, P_κ^{E} and P_κ^{B} .

Taking the square of (23) in Fourier space, we get the power spectrum of the density contrast, P_δ , on the right-hand side of the equation. Inserting the result into (28) we obtain the convergence power spectrum in terms of the density power spectrum as

$$P_\kappa(\ell) = \frac{9}{4} \Omega_{\text{m}}^2 \left(\frac{H_0}{c} \right)^4 \int_0^{\chi_{\text{lim}}} d\chi \frac{g^2(\chi)}{a^2(\chi)} P_\delta \left(k = \frac{\ell}{f_K(\chi)}, \chi \right). \quad (29)$$

This simple result can be derived using a few approximations: the Limber projection is applied, which only collects modes that lie in the plane of the sky, thereby neglecting correlations along the line of sight (Limber 1953, Kaiser 1992, Simon 2007, Giannantonio et al. 2012). In addition, the small-angle approximation (expanding to first order trigonometric functions of the angle) and the flat-sky limit (replacing spherical harmonics by Fourier transforms) are used. A further assumption is the absence of galaxy clustering, therefore ignoring source-source (Schneider et al. 2002b), and source-lens (Bernardeau 1998, Hamana et al. 2002) clustering. Theoretical predictions for the power

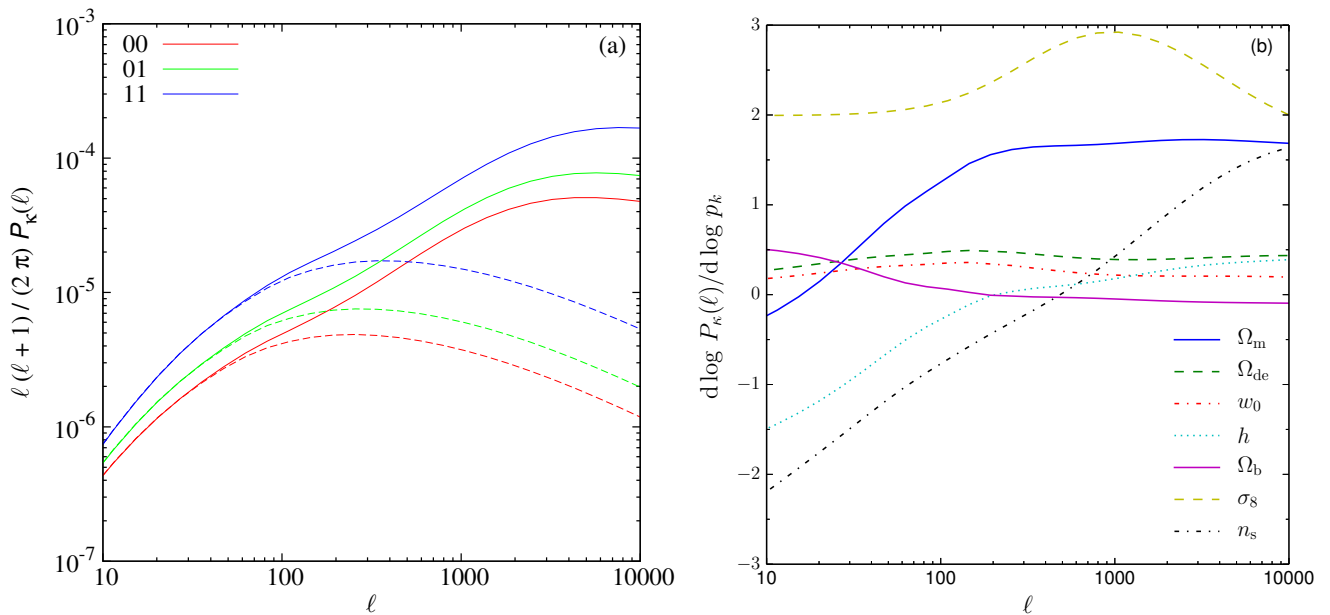


Figure 3. (a) The scaled tomographic convergence auto- and cross-power spectrum $\ell(\ell+1)/(2\pi)P_{\kappa,ij}(\ell)$ for two redshift bins i, j with redshift ranges $z = [0.5; 0.7]$, and $[0.9; 1.1]$, respectively. Solid (dashed) lines correspond to the non-linear (linear) model. (b) Derivatives $d \log P_{\kappa} / d \log p_k$ of the convergence power spectrum with respect to various cosmological parameters p_k , as indicated in the figure. The corresponding redshift bin is $[0.9; 1.1]$.

spectrum are shown in Fig. 3, using linear theory, and the non-linear fitting formulae of Takahashi et al. (2012). See Sect. 3.10 for the definition of the tomographic redshift bins.

The projection (29) mixes different 3D k -modes into 2D ℓ wavemodes along the line-of-sight integration, thereby washing out many features present in the 3D density power spectrum. For example, baryonic acoustic oscillations are smeared out and are not seen in the lensing spectrum (Simpson 2006, Zhang et al. 2009). This reduces the sensitivity of P_{κ} with respect to cosmological parameters, for example compared to the CMB anisotropy power spectrum. Examples for some parameters are shown in Fig. 3. Then two main response modes of P_{κ} for changing parameters are an amplitude change, caused by σ_8 , Ω_m , and w_0 , and a tilt, generated by n_s , and h (and, consequently, shifts are seen when varying the physical density parameters ω_m and ω_b). The parameter combination that P_{κ} is most sensitive to is $\sigma_8 \Omega_m^\alpha$, with $\alpha \approx 0.75$ in the linear regime (Bernardeau et al. 1997).

Writing the relations between κ , γ and the lensing potential ψ (19) in Fourier space, and using complex notation for the shear, one finds for $\ell \neq 0$

$$\tilde{\gamma}(\boldsymbol{\ell}) = \frac{(\ell_1 + i \ell_2)^2}{\ell^2} \tilde{\kappa}(\boldsymbol{\ell}) = e^{2i\beta} \tilde{\kappa}(\boldsymbol{\ell}), \quad (30)$$

with β being the polar angle of the wave-vector $\boldsymbol{\ell} = (\ell_1, \ell_2)$, written as complex quantity. Therefore, we get the very useful fact that the power spectrum of the shear equals the one of the convergence, $P_{\gamma} = P_{\kappa}$.

The shear power spectrum can in principle be obtained directly from observed ellipticities (e.g. Hu & White 2001), or via pixellised convergence maps in Fourier space that have been reconstructed (see Sect. 3.15) from the observed ellipticities, e.g. Seljak (1998). However, the simplest and most robust way to estimate second-order shear correlations are in real space, which we will discuss in the following section.

3.8. The shear correlation function

The most basic, non-trivial cosmic shear observable is the real-space shear two-point correlation function (2PCF), since it can be estimated by simply multiplying the ellipticities of galaxy pairs and averaging.

The two shear components of each galaxy are conveniently decomposed into *tangential component*, γ_t , and cross-component, γ_\times . With respect to a given direction vector $\boldsymbol{\theta}$ whose polar angle is ϕ , they are defined as

$$\gamma_t = -\Re(\gamma e^{-2i\phi}); \quad \gamma_\times = -\Im(\gamma e^{-2i\phi}). \quad (31)$$

The minus sign, by convention, results in a positive value of γ_t for the tangential alignment around a mass overdensity. Radial alignment around underdensities have a negative γ_t . A positive cross-component shear is rotated by $+\pi/4$ with respect to the tangential component.

Three two-point correlators can be formed from the two shear components, $\langle\gamma_t\gamma_t\rangle$, $\langle\gamma_\times\gamma_\times\rangle$ and $\langle\gamma_t\gamma_\times\rangle$. The latter vanishes in a parity-symmetric universe, where the shear field is statistically invariant under a mirror transformation. Such a transformation leaves γ_t invariant but changes the sign of γ_\times . The two non-zero two-point correlators are combined into the two components of the shear 2PCF (Miralda-Escude 1991*b*),

$$\begin{aligned} \xi_+(\theta) &= \langle\gamma\gamma^*\rangle(\theta) = \langle\gamma_t\gamma_t\rangle(\theta) + \langle\gamma_\times\gamma_\times\rangle(\theta); \\ \xi_-(\theta) &= \Re[\langle\gamma\gamma\rangle(\theta)e^{-4i\phi}] = \langle\gamma_t\gamma_t\rangle(\theta) - \langle\gamma_\times\gamma_\times\rangle(\theta). \end{aligned} \quad (32)$$

The two components are plotted in Fig. 4. We note here that from the equality of the shear and convergence power spectrum and Parseval's theorem, it follows that ξ_+ is identical to the two-point correlation function of κ .

An estimator of the 2PCF (Schneider et al. 2002*a*) is

$$\hat{\xi}_\pm(\theta) = \frac{\sum_{ij} w_i w_j (\varepsilon_{t,i} \varepsilon_{t,j} \pm \varepsilon_{\times,i} \varepsilon_{\times,j})}{\sum_{ij} w_i w_j}. \quad (33)$$

The sum extends over pairs of galaxies (i, j) at positions on the sky $\boldsymbol{\vartheta}_i$ and $\boldsymbol{\vartheta}_j$, respectively, whose separation $|\boldsymbol{\vartheta}_i - \boldsymbol{\vartheta}_j|$ lies in an angular distance bin around θ . Each galaxy has a measured ellipticity ε_i , and an attributed weight w_i , which may reflect the measurement uncertainty. Using the weak-lensing relation (26) and taking the expectation value of (33), we get terms of the following type, exemplarily stated for ξ_+ :

$$\langle\varepsilon_i^{(s)} \varepsilon_j^{(s)*}\rangle; \langle\varepsilon_i^{(s)} \gamma_j^*\rangle; \langle\gamma_i \varepsilon_j^{(s)*}\rangle; \quad \text{and} \quad \langle\gamma_i \gamma_j^*\rangle. \quad (34)$$

We discuss the first three terms in Sect. 3.11, in the context of intrinsic alignment (IA). In the absence of IA, those three terms vanish and the last term is equal to $\xi_+(|\boldsymbol{\vartheta}_i - \boldsymbol{\vartheta}_j|)$. The analogous case holds for ξ_- .

The main advantage of the simple estimator (33) is that it does not require the knowledge of the mask geometry, but only whether a given galaxy is within the masked area or not. For that reason, many other second-order estimators that we discuss in the following are based in this one.

Using (28) and (30), we write the 2PCF as Hankel transforms of the convergence power spectrum,

$$\begin{aligned} \xi_+(\theta) &= \frac{1}{2\pi} \int d\ell \ell J_0(\ell\theta) [P_\kappa^E(\ell) + P_\kappa^B(\ell)]; \\ \xi_-(\theta) &= \frac{1}{2\pi} \int d\ell \ell J_4(\ell\theta) [P_\kappa^E(\ell) - P_\kappa^B(\ell)]. \end{aligned} \quad (35)$$

These expressions can be easily and quickly integrated numerically using fast Hankel transforms (Hamilton 2000).

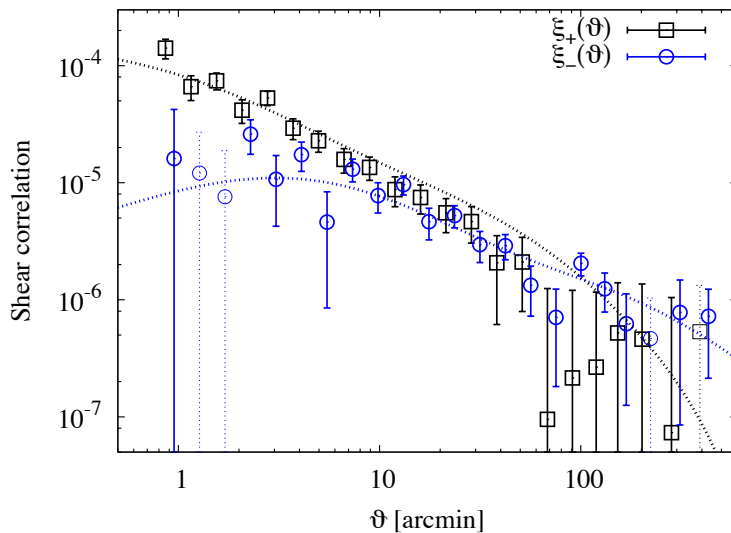


Figure 4. 2PCF components ξ_+ and ξ_- (32) measured in CFHTLenS. The dotted lines show the WMAP7 model prediction (Komatsu et al. 2011). From Kilbinger et al. (2013). Copyright 2013 Oxford University Press.

The two 2PCF components mix E- and B-mode power spectra in two different ways. To separate the two modes, a further filtering of the 2PCF is necessary, which will be discussed in the following section.

3.9. Derived second-order functions

Apart from the 2PCF (32), other, derived second-order functions have been widely used to measure lensing correlations in past and present cosmic shear surveys. The motivation for derived statistics are to construct observables that (1) have high signal-to-noise for a given angular scale, (2) show small correlations between different scales, and (3) separate into E- and B-modes. In particular the latter property is of interest, since the B-mode can be used to assess the level of (certain) systematics in the data as we have seen in Sect. 3.6.

All second-order functions can be written as filtered integrals over the convergence power spectrum, and the corresponding filter functions define their properties. In this section, we introduce the most widely used shear second-order functions, and briefly discuss their properties, see also Kilbinger et al. (2013) for an overview.

The *top-hat shear dispersion* is defined as the mean shear rms in an aperture of radius θ , $\langle |\gamma|^2 \rangle(\theta)$. The signal-to-noise of this measure for a given θ is high, since it is a broad low-pass band of P_κ , at the expense of exhibiting very strong correlations over the whole range of angular scales. This function has been used mainly in early cosmic-shear results, where the overall signal-to-noise was low.

Another popular statistic is the *aperture-mass dispersion*, denoted as $\langle M_{\text{ap}}^2 \rangle(\theta)$ (Fig. 5). First, one defines the *aperture mass* as mean tangential shear with respect to the centre $\boldsymbol{\vartheta}$ of a circular region, weighted by a filter function Q_θ with characteristic scale θ ,

$$M_{\text{ap}}(\theta, \boldsymbol{\vartheta}) = \int d^2\vartheta' Q_\theta(|\boldsymbol{\vartheta} - \boldsymbol{\vartheta}'|) \gamma_t(\boldsymbol{\vartheta}') = \int d^2\vartheta' U_\theta(|\boldsymbol{\vartheta} - \boldsymbol{\vartheta}'|) \kappa(\boldsymbol{\vartheta}'). \quad (36)$$

The second equality can be derived from the relations between shear and convergence, which defines the filter function U_θ in terms of Q_θ (Kaiser et al. 1994, Schneider 1996). The aperture mass is therefore closely related to the local projected over-density, and owes its name to this fact. The

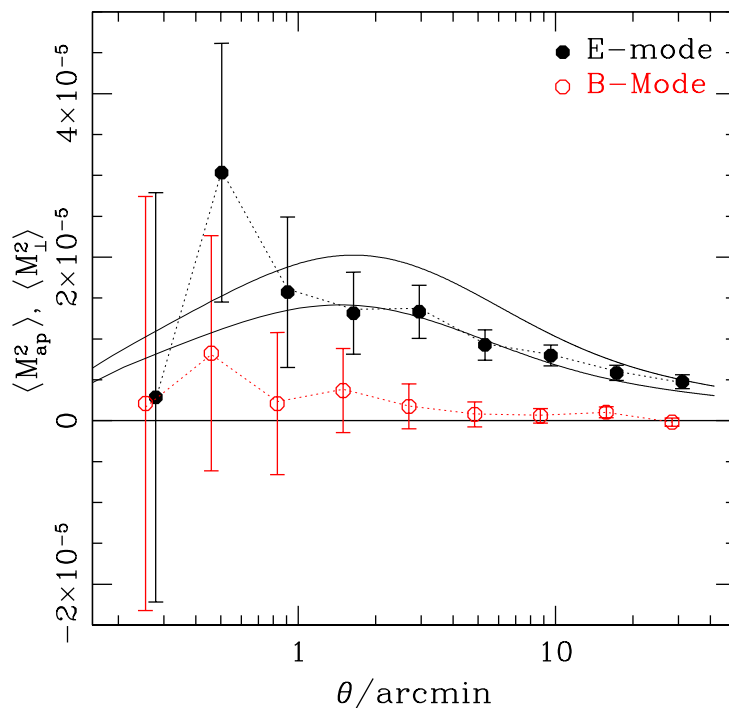


Figure 5. Aperture-mass dispersion measured in COSMOS. The two solid lines correspond to predictions with $\sigma_8 = 0.7$ and 0.8 , respectively. From Schrabback et al. (2010). Figure reproduced with permission from Schrabback et al. (2010), *A&A*, **516**, A63. © ESO.

function U_θ is compensated (i.e. the integral over its support vanishes, $\int d^2\vartheta U_\theta(\vartheta) = 0$), and filters out a constant mass sheet $\kappa_0 = \text{const}$, since the monopole mode ($\ell = 0$) is not recoverable from the shear (30). Two choices for the functions U_θ , and consequently Q_θ , have been widely used for cosmic shear, a fourth-order polynomial (Schneider et al. 1998), and a Gaussian function (Crittenden et al. 2002).

By projecting out the tangential component of the shear, M_{ap} is sensitive to the E-mode only. One defines M_\times by replacing γ_t with γ_\times in (36) as a probe of the B-mode only. The variance of (36) between different aperture centres defines the dispersion $\langle M_{\text{ap}}^2 \rangle(\theta)$, which can be interpreted as fluctuations of lensing strength between lines of sight, and therefore have an intuitive connection to fluctuations in the projected density contrast.

The prospect of E-/B-mode separation motivated another derived shear second-order functions, the *E- and B-mode correlation functions* $\xi_+^{\text{E,B}}$ and $\xi_-^{\text{E,B}}$ (Schneider et al. 2002b, Crittenden et al. 2002). Despite their name, they are also represented as integrals over the 2PCF.

Both top-hat shear rms and aperture-mass dispersion can in principle be estimated by averaging over many aperture centres ϑ . This is however not practical: The sky coverage of a galaxy survey is not contiguous, but has gaps and holes due to masking. Apertures with overlap with masked areas biases the result, and avoiding overlap results in a substantial area loss. This is particularly problematic for filter functions whose support extend beyond the scale θ . One possibility is to fill in the missing data, e.g. with inpainting techniques (Pires et al. 2009b), resulting in a pixelised, contiguous convergence map on which the convolution (36) can be calculated very efficiently (Leonard et al. 2012b). Alternatively, the dispersion measures can be expressed in terms of the 2PCF, and are therefore based on the estimator (33) for which the mask geometry does not play a role.

In fact, every second-order statistic can be expressed as integrals over the 2PCF because, as mentioned above, all are functions of P_κ , and the relation (35) can be inverted. In general, they do not contain the full information about the convergence power spectrum (Eifler et al. 2008), but

separate E- and B-modes.

The general expression for an E-/B-mode separating function $X_{\text{E,B}}$ is

$$X_{\text{E,B}} = \frac{1}{2\pi} \int_0^\infty d\ell \ell P_\kappa^{\text{E,B}}(\ell) \tilde{U}^2(\ell). \quad (37)$$

A practical estimator using (33) is

$$\hat{X}_{\text{E,B}} = \frac{1}{2} \sum_i \vartheta_i \Delta\vartheta_i \left[T_+(\vartheta_i) \hat{\xi}_+(\vartheta_i) \pm T_-(\vartheta_i) \hat{\xi}_-(\vartheta_i) \right]. \quad (38)$$

Here, $\Delta\vartheta_i$ is the bin width, which can vary with i , for example in the case of logarithmic bins. The filter functions T_\pm and \tilde{U}^2 are Hankel-transform pairs, given by the integral relation (Crittenden et al. 2002, Schneider et al. 2002b)

$$T_\pm(x) = \int_0^\infty dt t J_{0,4}(xt) \tilde{U}^2(t). \quad (39)$$

This implicit relation between T_+ and T_- guarantees the separation into E- and B-modes of the estimator (38).

In some cases of $X_{\text{E,B}}$, for example for the aperture mass and top-hat shear dispersion, the power-spectrum filter \tilde{U} is explicitly given as the Fourier transform of a real-space filter function U , see e.g. (36) for the aperture mass. In other cases the functions T_\pm are constructed first, and \tilde{U} is calculated by inverting the relation (39). Model predictions of X_{E} can be obtained from either (37), or (38). For the latter, one inserts a theoretical model for ξ_\pm , and does not need to calculate \tilde{U} .

3.9.1. E-/B-mode mixing None of the derived second-order functions introduced so far provide a pure E-/B-mode separation. They suffer from a leakage between the modes, on small scales, or large scales, or both. This mode mixing comes from the incomplete information on the measured shear correlation: On very small scales, up to 10 arc seconds or so, galaxy images are blended, preventing accurate shape measurements, and thus the shape correlation on those small scales is not sampled. Large scales, at the order of degrees, are obviously only sampled up to the survey size. This leakage can be mitigated by (i) extrapolating the shear correlation to unobserved scales using a theoretical prediction (thereby potentially biasing the result), or (ii) cutting off small and/or large scales of the derived functions (thereby losing information) (Kilbinger et al. 2006).

E-/B-mode mixing can be avoided altogether by defining derived second-order statistics via suitable filter functions. For a pure E-/B-mode separation, those filter functions need to vanish on scales where the shear correlation is missing. Corresponding derived second-order quantities are the *ring statistics* (Schneider & Kilbinger 2007), variations thereof (Eifler et al. 2010, Fu & Kilbinger 2010), and the so-called COSEBIs (Complete Orthogonal Sets of E-/B-mode integrals; Schneider et al. 2010), see Fig. 6 for an example. The latter quantities do not depend on a continuous angular scale parameter θ , but are a discrete set of modes $E_n, B_n, n = 1, 2, \dots$. Typically, fewer than 10 COSEBI modes are sufficient to capture all second-order E-mode information (Asgari et al. 2012).

3.10. Shear tomography and 3D lensing

The redshift distribution of source galaxies determines the redshift range over which the density contrast is projected onto the 2D convergence and shear. By separating source galaxies according to their redshift, we obtain lensing fields with different redshift weighting via the lens efficiency (24), thus probing different epochs in the history of the Universe with different weights. Despite the two-dimensional aspect of gravitational lensing, this allows us to recover a 3D *tomographic* view of the large-scale structure. In particular, it helps us to measure subtle effects that are projected out in 2D lensing, such as the growth of structures, or a time-varying dark-energy state parameter $w(z)$.

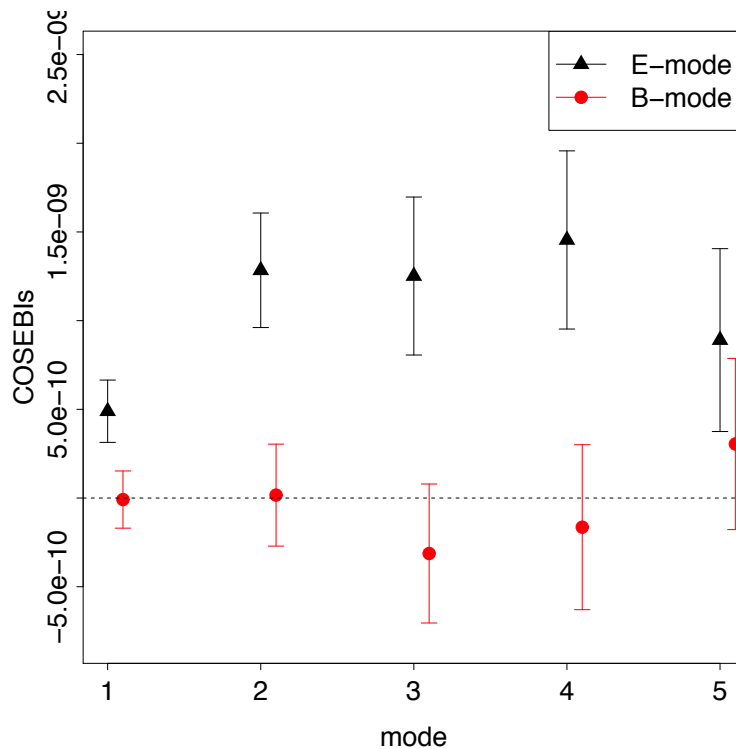


Figure 6. First five COSEBIs modes, measured in SDSS. From Huff et al. (2014a). Figure reproduced with permission from Huff et al. (2014a), *MNRAS*, **440**, 1322. Copyright 2014 Oxford University Press.

3.10.1. Tomographic redshift binning If we denote the redshift distribution in each of N_z bin with $p_i, i = 1 \dots N_z$, we obtain a new lensing efficiency q_i (24) for each case, and a resulting projected overdensity κ_i . This leads to $N_z(N_z - 1)/2$ convergence power spectra $P_{\kappa,ij}, 1 \leq i \leq j \leq N_z$, including not only the auto-spectra ($i = j$) but also the cross-spectra ($i \neq j$). In (29), q^2 is replaced by the product $q_i q_j$ (Seljak 1998, Hu 1999).

The lensing efficiency is a very broad function in comoving distance, or redshift, and therefore the tomographic power spectra are not independent: Parts of the large-scale structure, despite it being weighted differently by galaxies in different bins, contribute to all tomographic power spectra. Moreover, photometric redshift errors cause galaxy distributions in different redshift bins to overlap, increasing their correlation. Uncorrelated bins can be obtained by linear re-weighting of the galaxy redshift distribution (Huterer & White 2005, Schäfer & Heisenberg 2012, Bernardeau et al. 2014). These *nulling* techniques can also produce near-cancellations of power in certain regions of k -space, for example to exclude highly non-linear, baryon-effect dominated scales.

A relatively small number of redshift bins has been predicted to be sufficient for a large improvement on standard cosmological parameters (Hu 1999, Simon et al. 2004). When more parameters are included that have small effects on the growth rate, e.g. dark energy and its time variation, the number of necessary bins is higher. The photometric redshift uncertainty limits the number of useful sub-divisions of the galaxies into bins: A large dispersion washes out the binned redshift distribution resulting in information loss (Ma et al. 2006). Catastrophic redshift outliers, galaxies whose photometric redshift is many standard deviations away from its true redshift, set even higher requirements on photometric redshifts, and on their calibration from spectroscopic training samples (Huterer et al. 2006, Bernstein & Huterer 2010, Sun et al. 2009, Hearin et al. 2010). The presence of intrinsic alignment (see Sect. 3.11) significantly adds to the demands on photometric redshifts (Bridle & King 2007).

3.10.2. 3D lensing The technique of 3D lensing makes full use the redshift information of each galaxy individually, instead of binning into redshift slices. 3D lensing (Heavens 2003, Castro et al. 2005, Kitching et al. 2011b, Munshi et al. 2011) samples the three-dimensional shear field by performing a spherical harmonics transform of the field into ℓ -modes on the sky, and k -modes along the line of sight. In particular, it does not mix different k -modes by projecting onto the 2D sky, and allows for a clear cut directly in k -space, e.g. to exclude small, non-linear scales from the analysis.

3D lensing uses the shear (in harmonics space) as signal, the expectation of which is zero. The cosmological information is contained in the covariance, which depends on the shear power spectrum. This is analogous to CMB, where the temperature difference $\Delta T/T$ is the signal with zero mean, and the information is extracted from the signal covariance, the angular power spectrum C_ℓ . The advantages of this approach are that only the Gaussian part of the shear field is measured, involving statistics up to second order in γ (the covariance of γ), whereas for a traditional lensing analysis, with second-order correlations as the observed signal, terms up to order four in γ have to be included for signal covariance. This allows for a simple analytical calculation of the 3D lensing covariance without having to resort to realisations of N -body simulations, the number of which needs to be very large for an accurate estimation of the covariance (Sect. 5.1).

To practically estimate the covariance from data, the mask geometry has to be accounted for. Masked areas cause power to mix from scales affected by the mask to other scales, contaminating the cosmological analysis. This is done by either (i) applying the effect of the mask, expressed by a mixing matrix, to the theoretical prediction, for example with the pseudo- C_ℓ method (Hivon et al. 2002), or (ii) by correcting the data for the mask, requiring matrix inversion under a regularisation scheme. To successfully account for the mask, the survey area needs to be relatively large; a 3D lensing analysis of a survey of a few square degrees is very challenging. For this reason, the first comprehensive cosmological analysis was performed only recently, using about 120 square degrees of CFHTLenS (Kitching et al. 2014).

Unlike the case of the shear correlation function or power spectrum, the 3D lensing observables in general include a non-zero B-mode, in addition to the E-mode, due to mixing in presence of a mask and shear biases (Kitching et al. 2014). In the absence of systematics (instrumental or astrophysical), the B-mode is consistent with shot noise. This signal can be predicted using a reference cosmology.

3.11. Intrinsic alignment

Shapes of galaxies can be correlated in the absence of gravitational lensing, due to gravitational interactions between galaxies and the surrounding tidal fields. The *intrinsic alignment* (IA) of galaxy shapes adds an excess correlation to the cosmic shear signal that, if not taken into account properly, can bias cosmological inferences by tens of per cent. IA is difficult to account for, since it cannot simply be removed by a sophisticated galaxy selection, nor can it be easily predicted theoretically since it depends on details of galaxy formation. First predictions of IA came about around the time of the first detection of cosmic shear. These works used a wide range of methods, including analytical calculations (Crittenden et al. 2001, Catelan et al. 2001, Mackey et al. 2002) and N -body simulations of dark matter, measuring alignments from dark matter halos only (Croft & Metzler 2000, Heavens et al. 2000), or by populating halos with galaxies using simple, semi-analytic prescriptions for their shape correlations (Heavens et al. 2000). Unfortunately, different predictions do not agree with each other, and the main difficulty remains to understand the alignment of galaxies within their surrounding dark-matter structures. Galaxy formation can strongly modify angular momentum and tidal stretching alignments, and erase correlations that have been present in the dark matter. Only recently have hydro-dynamical simulations attained a high enough resolution to

form galaxies with realistic morphologies, allowing for a direct measurement of galaxy alignments (Hahn et al. 2010, Dubois et al. 2014, Codis et al. 2015, Tenneti et al. 2014).

Two main mechanisms are believed to produce intrinsic shape correlations of galaxies that are formed in the same tidal gravitational field: **First**, spin axes of (spiral) galaxies become aligned during galaxy formation due to the exertion of a torquing moment by the tidal field (tidal torquing). **Second**, halo shapes of (elliptical) galaxies are coherently stretched by the tidal field. This can also include anisotropic accretion e.g. along filaments, see Schäfer (2009) for a comprehensive review of the theory of galactic angular momenta and their correlations.

Due to IA, the intrinsic ellipticity of galaxies ε^s no longer has a random orientation, or phase. This directly contributes to the measured two-point shear correlation function (33), as follows. The first term in (34) describes the correlation of intrinsic ellipticities of two galaxies i and j . This term (II , or shape-shape correlation) is non-zero only for physically close galaxies. Its contribution to cosmic shear (GG , or shear-shear correlation), the last term in (34), can be suppressed by down-weighting or omitting entirely galaxy pairs at the same redshift (Heymans & Heavens 2003, King & Schneider 2002, King & Schneider 2003).

The second and third term in (34) correspond to the correlation between the intrinsic ellipticity of one galaxy with the shear of another galaxy. For either of these terms (GI , or shape-shear correlation) to be non-zero, the foreground galaxy ellipticity has to be correlated via IA to structures that shear a background galaxy. A lensing mass distribution causes background galaxies to be aligned tangentially. Foreground galaxies at the same redshift as the mass distribution are stretched radially towards the mass by tidal forces. Therefore the ellipticities of background and foreground galaxies tend to be orthogonal, corresponding to a negative GI correlation. For typical cosmic shear surveys with not too small redshift bins, GI dominates over II . It is therefore rather surprising that this term was discussed for the first time only in 2004 (Hirata & Seljak 2004).

Contrary to II , the GI contribution is very hard to remove since galaxy pairs at all line-of-sight separations are affected. To mitigate GI in a model-independent way, one can exploit the known dependence with source redshift (which only involves angular distances). Weighted combinations of the measured shear signal at different redshifts can be formed that provide a *nulling* of the GI contribution. The disadvantage of this technique is a loss in cosmological information, and a very strong requirement on photometric redshift accuracy (Joachimi & Schneider 2008, Joachimi & Schneider 2009). Alternatively, cosmic shear data can be analysed by jointly modelling IA and cosmology (King 2005, Bernstein 2009, Joachimi & Bridle 2010). This however might introduce biases on cosmological parameters if a wrong or restrictive IA model is chosen (Kirk et al. 2012). See Troxel & Ishak (2014) for a review of IA in a weak-lensing context.

Additional observations of galaxy properties could help to infer their intrinsic orientation, alleviating the contribution of intrinsic alignment, for example from spectroscopic data (Blain 2002, Huff et al. 2013), or polarization observations in the radio (see Sect. 8.2).

3.12. Galaxy-galaxy lensing

In contrast to cosmic shear, galaxy-galaxy lensing (GGL) correlates shapes of high-redshift galaxies with positions of galaxies at lower redshift. The resulting weak-lensing correlation singles out the mass associated with the foreground galaxy sample. GGL has many applications in astrophysics and cosmology, in particular when it is combined with other observations of properties of the foreground galaxy sample. GGL probes galaxy halos from several kpc out to Mpc distances, providing insights about halo masses and density profiles, e.g. as function of stellar mass, luminosity, type, or environment (Mandelbaum et al. 2006b).

GGL becomes of particular cosmological interest when complemented with statistical

measurements of other matter tracers, for example spatial galaxy correlations (projected or in redshift space), cosmic shear, or galaxy velocity correlations (Guzik et al. 2010, Simon 2012). The combination of those observables allows for detailed and quasi-model-independent analyses of the relation between luminous and dark matter, including the measurement of galaxy bias, in particular its linearity, scale-dependence, and stochasticity. Since these different correlations also probe different combinations of the Bardeen potentials (1), they can test General Relativity.

GGL is usually quantified as the mean tangential shear $\langle \gamma_t \rangle$ of background galaxies around foreground galaxies. It is a measure of the excess projected mass within an aperture (Miralda-Escude 1991a, Squires & Kaiser 1996). The mean convergence in a circular aperture of angular radius θ is

$$\bar{\kappa}(\leq \theta) = \frac{1}{\pi\theta^2} \int_{|\theta'| < \theta} d^2\theta' \kappa(\theta') = \frac{2}{\theta^2} \int_0^\theta d\theta' \theta' \langle \kappa \rangle(\theta'), \quad (40)$$

where the second equality defines the circularly averaged quantity $\langle \kappa \rangle(\theta') = (2\pi)^{-1} \int_0^{2\pi} d\varphi \kappa(\theta', \varphi)$. Since 2κ is equal to the divergence of the gradient of the lensing potential ψ (19), one can apply Gauss' law and eliminate the divergence. The resulting integral along the circle then depends on the derivative of ψ in radial direction \hat{e}_θ , normal to the circle; the tangential part along the aperture's circumference \hat{e}_φ is projected out. Accounting for the circle length of $2\pi\theta$, one gets

$$\bar{\kappa}(\leq \theta) = \frac{1}{2\pi\theta} \int_0^{2\pi} d\varphi \partial_\theta \psi(\theta, \varphi). \quad (41)$$

Calculating the derivative with respect to the radius θ introduces a second radial derivative, resulting in

$$\frac{\partial[\theta\bar{\kappa}(\leq \theta)]}{\partial\theta} = \int_0^{2\pi} \frac{d\varphi}{2\pi} \partial_\theta \partial_\theta \psi(\theta, \varphi) = \langle \kappa \rangle(\theta) - \langle \gamma_t \rangle(\theta). \quad (42)$$

The second equality follows from (19) for a local Cartesian coordinate system $(\hat{e}_\theta, \hat{e}_\varphi)$. As above, angle brackets denote circular averages.

On the other hand, calculating the derivative of (40) yields

$$\frac{\partial[\theta\bar{\kappa}(\leq \theta)]}{\partial\theta} = -\bar{\kappa}(\theta) + 2\langle \kappa \rangle(\theta). \quad (43)$$

Equating the two expressions, we get

$$\langle \gamma_t \rangle(\theta) = \bar{\kappa}(\leq \theta) - \langle \kappa \rangle(\theta). \quad (44)$$

The mean tangential shear at radius θ is therefore a direct measure of the total projected mass inside this radius, minus a boundary term. This result is very general as it makes no assumption about the actual mass distribution.

We can express $\langle \gamma_t \rangle$ in terms of a *surface mass excess* as follows. In the case of a single lens localised at angular diameter distance D_l , we can approximate (21) with

$$\kappa(\theta) = \frac{4\pi G D_l D_{ls}}{c^2 D_s} \int_{D_l - \Delta D/2}^{D_l + \Delta D/2} dD \Delta\rho(D\theta, D), \quad (45)$$

where D_s is the distance to the source, and D_{ls} the distance between lens and source. All distances in this and subsequent equations are proper distance. The integral over the lens mass density contrast $\Delta\rho = \rho - \bar{\rho} = \bar{\rho}\delta$ is carried out along the physical extent of the mass concentration ΔD . This integral is defined as *surface mass density* Σ . Introducing the critical surface mass density $\Sigma_{\text{cr}}^{-1} = (4\pi G/c^2)(D_l D_{ls}/D_s)$, the convergence is simply

$$\kappa(\theta) = \frac{\Sigma(\theta)}{\Sigma_{\text{cr}}}. \quad (46)$$

Then, (44) can be written in terms of the surface mass as

$$\langle \gamma_t \rangle (\theta) \Sigma_{\text{cr}} = \Delta \Sigma(\leq \theta) = \bar{\Sigma}(\theta) - \langle \Sigma \rangle (\theta). \quad (47)$$

If the convergence in (45) is measured statistically with GGL, it is actually a two-point correlation function, between background lensing and foreground galaxy over-density δ_g . Thus,

$$\begin{aligned} \langle \kappa \rangle (\theta) &= \langle \kappa(\boldsymbol{\vartheta}) \delta_g(\boldsymbol{\vartheta} + \boldsymbol{\theta}) \rangle_{\boldsymbol{\vartheta}} \\ &= \Sigma_{\text{cr}}^{-1} \bar{\rho} \int D \langle \delta(D\boldsymbol{\theta}, D) \delta_g(D_1\boldsymbol{\theta}, D_1) \rangle \\ &= \Sigma_{\text{cr}}^{-1} \bar{\rho} \int dD \xi_{\delta_g}(\sqrt{(D\theta)^2 + (D - D_1)^2}). \end{aligned} \quad (48)$$

In the last step, the cross-correlation function between galaxy and matter overdensity, ξ_{δ_g} was introduced. Alternatively, the convergence can be expressed as a function of the Fourier transform of ξ_{δ_g} , the galaxy-matter power spectrum P_{δ_g} . The relation between ξ_{δ_g} and the matter correlation function $\xi_{\delta\delta}$ depends on the model of the bias between galaxies and matter. GGL thus offers a unique way to measure this relation.

The measurement of circularly averaged tangential shear (44) makes it robust against anisotropic systematics, e.g. induced by PSF residuals, see Sect. 6.3. Further, diagnostic null tests can easily be performed: First, the mean cross-component γ_{\times} around foreground galaxies violates parity and is therefore expected to vanish. Second, the tangential shear should be zero around random points, and around special points that are not associated with the foreground sample, such as stars, field centres, or chip corners.

3.13. The lensing bispectrum

The convergence power spectrum P_{κ} (29) only captures the Gaussian component of the LSS. There is however substantial complementary non-Gaussian information in the matter distribution, in particular on small scales, where the non-linear evolution of structures creates non-Gaussian weak-lensing correlations. On small and intermediate scales, these non-linear structures are the dominant contributor to non-Gaussian lensing signatures, compared to (quasi)-linear perturbations, or potential primordial non-Gaussianity. Constraints on the latter from cosmic shear alone can not compete with constraints from other probes such as CMB or galaxy clustering (Takada & Jain 2004, Pace et al. 2011, Hilbert et al. 2012).

To measure these non-Gaussian characteristics, one has to go beyond the second-order convergence power spectrum. The next-leading order statistic is the bispectrum B_{κ} , which is defined by the following equation:

$$\langle \tilde{\kappa}(\boldsymbol{l}_1) \tilde{\kappa}(\boldsymbol{l}_2) \tilde{\kappa}(\boldsymbol{l}_3) \rangle = (2\pi)^2 \delta_D(\boldsymbol{l}_1 + \boldsymbol{l}_2 + \boldsymbol{l}_3) [B_{\kappa}(\boldsymbol{l}_1, \boldsymbol{l}_2) + B_{\kappa}(\boldsymbol{l}_2, \boldsymbol{l}_3) + B_{\kappa}(\boldsymbol{l}_3, \boldsymbol{l}_1)]. \quad (49)$$

The bispectrum measures three-point correlations of the convergence defined on a closed triangle in Fourier space. B_{κ} can be related to the density bispectrum B_{δ} via Limber's equation (Cooray & Hu 2001). Other measures of non-Gaussianity are presented in Sect. 8.6.

The corresponding real-space weak-lensing observable is the shear three-point correlation function (3PCF) (Takada & Jain 2003, Schneider & Lombardi 2003, Zaldarriaga & Scoccimarro 2003, Benabed & Scoccimarro 2006). Correlating the two-component shear of three galaxies sitting on the vertices of a triangle, the 3PCF has $2^3 = 8$ components, and depends on three angular scales. Those eight components can be combined into four complex *natural* components (Schneider & Lombardi 2003, Schneider et al. 2005).

A simple estimator of the 3PCF can be constructed analogous to (33), by summing up triplets of galaxy ellipticities at binned triangles. The relations between the 3PCF and the bispectrum are

complex, and it is not straightforward to efficiently evaluate those numerically. Most measurements and cosmological analyses of higher-order cosmic shear have been obtained using the aperture-mass skewness $\langle M_{\text{ap}}^3 \rangle$ (Pen et al. 2003, Jarvis et al. 2004, Schneider et al. 2005). $\langle M_{\text{ap}}^3 \rangle$ is the skewness of (36), and can be written as pass-band filter over the convergence bispectrum. Analogous to the second-order case, relations exist to represent $\langle M_{\text{ap}}^3 \rangle$ as integrals over the 3PCF, facilitating the estimation from galaxy data without the need to know the mask geometry. Corresponding filter functions have been found in case of the Gaussian filter, but not the polynomial one (Jarvis et al. 2004). An extension to filters with three different aperture scales, permitting to probe the bispectrum for different ℓ_1, ℓ_2, ℓ_3 has been obtained in Schneider et al. (2005). Pure E-/B-mode separating third-order functions have been calculated (Shi et al. 2011, Krause et al. 2012), but a rigorous treatment analogous to the second-order COSEBIs (Sect. 3.9) are still lacking. This being said, the leakage on small scales is less severe compared to the second-order case (Shi et al. 2014).

Convergence power- and bispectra show different dependencies on the geometry of the universe, and on the growth of structures. This is true even for simple models, where, inspired by perturbation theory, the bispectrum is given in terms of products of the power spectrum. The combination of second- and third-order statistics helps lifting parameter degeneracies, in particular the one between Ω_m and σ_8 (Bernardeau et al. 1997, Takada & Jain 2004, Kilbinger & Schneider 2005). Combining weak-lensing power- and bispectrum measures can also be used for self-calibration techniques (Huterer et al. 2006, Semboloni et al. 2013b).

3.14. Higher-order corrections

The approximations made in Sects. 3.3 and 3.7, resulting in the convergence power spectrum, have to be tested for their validity. Corrections to the linearised propagation equation (18) include couplings between lens structures at different redshift (lens-lens coupling), and integration along the perturbed ray (additional terms to the Born approximation). Further, higher-order correlations of the convergence take account of the reduced shear as observable. Similar terms arise from the fact that the observed size and magnitudes of lensing galaxies are correlated with the foreground convergence field (magnification and size bias; Hamana 2001, Schmidt et al. 2009b). Over the relevant scale range ($\ell \leq 10^4$) most of those effects are at least two orders of magnitude smaller than the first-order E-mode convergence power spectrum, and create a B-mode spectrum of similar low amplitude. The largest contribution is the reduced-shear correction, which attains nearly 10% of the shear power spectrum on arc minute scales (Bernardeau et al. 1997, Schneider et al. 1998, Dodelson et al. 2006, Krause & Hirata 2010).

Thanks to the broad lensing kernel, the Limber approximation is very precise and deviates from the full integration only on very large scales, for $\ell < 20$ (Giannantonio et al. 2012). The full GR treatment of fluctuations together with dropping the small-angle approximation was also found to make a difference only on very large scales (Bernardeau et al. 2010).

Additional corrections come from the clustering of galaxies, causing local variations in the redshift distribution that are correlated with the density and therefore with the lensing convergence. Both the self-clustering of source galaxies (Schneider et al. 2002b) as well as associations between source galaxies and lens structures (source-lens clustering; Valageas 2014) cause sub-percent corrections for $\ell \leq 10^4$.

Many of the above mentioned corrections are more important for higher-order lensing statistics (Hamana et al. 2002, Dodelson & Zhang 2005, Valageas 2014). This can be seen by developing the density contrast into a perturbative series $\delta = \delta^{(1)} + \delta^{(2)} + \dots$, with $\delta^{(\nu)} \propto [\delta^{(1)}]^\nu$. The first-order lensing power spectrum goes with the square of the first-order density contrast, $P_\kappa \propto \langle [\delta^{(1)}]^2 \rangle$. Lensing corrections typically add one order in density, so corrections to P_κ are proportional to $\langle [\delta^{(1)}]^3 \rangle$, and

are thus suppressed by one power of the density contrast. However, the lowest third-order term $\langle [\delta^{(1)}]^3 \rangle$ vanishes since $\delta^{(1)}$ is assumed to be a Gaussian field. The lensing bispectrum B_κ in this perturbation theory approach is proportional to $\langle \delta^{(2)} \delta^{(1)} \delta^{(1)} \rangle \propto \langle [\delta^{(1)}]^4 \rangle$, which is of the same order as the corrections $\propto \langle [\delta^{(1)}]^4 \rangle$ to B_κ .

The intrinsic alignment of galaxy orientations contribute to the lensing power spectrum at up to 10%. This is discussed in more detail in Sect. 3.11.

3.15. Weak-lensing mass maps

All information that can be extracted from weak-lensing distortions is contained in the observed ellipticity of galaxies. In Sects. 3.8, 3.9 and 3.13, we have seen how to extract statistical information from the observed ellipticities. In some cases however, one wishes to estimate the convergence to create a local measure of the projected overdensity.

The convergence can be obtained either indirectly by reconstruction from the observed galaxy ellipticities, or directly from a measurement of the magnification, see Sect. 8.4. The former method was first proposed by Kaiser & Squires (1993): The relation between κ and γ via the lensing potential ψ (19) can be written as the integral

$$\kappa(\boldsymbol{\theta}) = \frac{1}{\pi} \int d^2\theta' \mathcal{D}^*(\boldsymbol{\theta} - \boldsymbol{\theta}') \gamma(\boldsymbol{\theta}') + \kappa_0. \quad (50)$$

The kernel \mathcal{D} is π times the Fourier transform of the prefactor in (30). The convergence is therefore given as a convolution of the shear field, i.e. there exist a linear relation between the two. However, a few caveats complicate a simple application of the above relation to obtain κ . **First**, replacing the integral by a discrete sum over galaxies at measured positions results in infinite noise, since the sampled uncorrelated intrinsic ellipticities are a white-noise component, contributing a $1/\theta^2$ -divergence to (50) (Kaiser & Squires 1993). Smoothing is therefore required, which results in a decreased resolution and correlated noise, and requires accounting for masks. **Second**, the integral (50) extends over \mathbb{R}^2 , and any reconstruction algorithm has to be modified to account for finite observed fields, to avoid boundary artefacts in the reconstruction (Seitz & Schneider 1996). **Third**, the convergence is obtained up to an additive constant κ_0 , corresponding to the $\ell = 0$ mode that is undefined in (30): A constant convergence does not induce a shear, and is therefore unobservable without additional information such as magnification to lift this *mass-sheet degeneracy*. Lastly, (30) is only a first-order approximation, and becomes a non-linear relation if the reduced shear $g = \gamma/(1 - \kappa)$ is used instead of the unobservable shear.

Despite of these difficulties, mass maps have several advantages over the shear field. The convergence is a scalar quantity, and in some sense simpler than the spinor shear, and also more directly related to (projected) mass. This facilitates the cross-correlation with other maps of mass tracers, for example galaxy overdensities, or the Sunyaev-Zel'dovich (SZ) effect. These measurements help to understand properties of those tracers and their relation to the underlying dark-matter environment. Further, higher-order correlations are simpler using convergence maps; in fact, many reconstruction methods provide the κ field in Fourier space, allowing the easy and fast calculation of higher-order spectra. Reconstructing the lensing potential provides a measure of $\Psi + \Phi$ which in combination with other probes that for example measured Φ , can yield constraints on general relativity (Sect. 2.3).

Alternative techniques have been proposed as well, for example non-linear methods (Pires et al. 2009b), or the addition of extra-information, such as weak gravitational flexion (Pires & Amara 2010) or the observed galaxy distribution as prior tracer of the total matter (Szepietowski et al. 2014, Simon 2013). Reconstructions in three dimensions are briefly discussed in Sect. 8.3.

Results and cosmological applications of mass reconstructions are presented in Sect. 7.4.

4. Numerical simulations

4.1. The necessity of simulations for weak lensing

Numerical simulations play a central role in the cosmological interpretation of cosmic shear data. Realistic simulations of large volumes of the large-scale structure are necessary for weak cosmological lensing for a variety of reasons, as follows.

First, the scales on which cosmic shear probes the LSS extend deep into the highly non-linear regime. To make analytical predictions of the power spectrum on those scales is very difficult. N -body simulations offer ways to obtain the non-linear power spectrum (i) by establishing fitting formulae based on the linear power (e.g. Peacock & Dodds 1994, Peacock & Dodds 1996, Smith et al. 2003, Takahashi et al. 2012); (ii) by directly providing the non-linear power using templates (Heitmann et al. 2009, Lawrence et al. 2010, Heitmann et al. 2014); or (iii) by calibrating semi-analytical, non-linear models such as the halo model (Cooray & Sheth 2002, Jing & Suto 2002, Tinker et al. 2008, Tinker et al. 2010), or hierarchical clustering models (Bernardeau & Schaeffer 1992, Munshi & Jain 2001). Simulations are even more important for higher-order statistics, such as the bispectrum or peak counts (Sect. 8.6), for which theoretical predictions are much harder to be obtained compared to the power spectrum.

Second, the density field δ , and consequently the weak-lensing convergence κ , is highly non-Gaussian on those non-linear scales. The distribution of κ is not easily assessed. Information about this distribution can however be estimated from a sufficiently large number of independent numerical simulations. Even complex survey properties that affect this distribution, like an inhomogeneous depth or a complicated mask geometry, can be easily included in the simulations. From the distribution of lensing observables, their covariance can be estimated, which is of great importance for cosmological error analyses. This is discussed in more detail in Sect. 5.1.

Third, baryonic effects have to be taken into account with increasing necessity for current and future surveys. Hydro-dynamical simulations with various details of baryonic physics have been run to quantify the influence on the total matter power spectrum, and to implement ways to take baryons into account for cosmological predictions (Jing et al. 2006, Rudd et al. 2008, Semboloni et al. 2011a).

Fourth, N -body simulations are an important tool for the analysis of potential astrophysical and observational systematics. This is in particular true for observational effects that are intertwined with astrophysics and cosmology in a complex way. One example is the recently discovered correlation between the weak-lensing galaxy selection function and the background density field: Close galaxy pairs whose images are blended are deselected by most lensing pipelines, since their shapes are not easily measured. This leads to an underrepresentation of high density regions and therefore to a bias if not corrected (Hartlap et al. 2011). A similar bias arises from massive foreground galaxies blocking the line of sight to background galaxies. Another example is the assessment of systematics, for which the cosmological shear signal has to be modeled as well: The distribution of a systematics measurement can be altered by the latter: For example a chance alignments between LSS and PSF pattern can create a non-zero shape correlation between stars and galaxies (see Sect. 6.6). To assess data quality using such a systematic test, this distribution has to be accounted for, to compare with the simulated, systematic-free case (Heymans et al. 2012). Other examples are contributions to lensing that depend on complex non-linear or baryonic physics, such as intrinsic galaxy alignment or source clustering.

Fifth, some mathematical approximations of weak lensing can be tested with simulations, such as linearisation of the propagation equation (Born approximation and lens-lens coupling; Hilbert et al. 2009), or the reduced shear (Dodelson et al. 2006), see also Sect. 3.14.

4.2. Principles of ray-shooting and ray-tracing

The simulation of gravitational lensing by large-scale structures can be performed by propagating light rays through the particle distribution of an N -body simulation. The techniques of calculating the light propagation depend on the nature and accessibility of the N -body simulation. In the following, we will present some of these methods.

4.2.1. Projecting the density field In many cases, an N -body simulation is available as snapshots corresponding to different redshifts, in the form of boxes in comoving 3D cartesian coordinates. The density in each box is projected onto a 2D “lens plane”, yielding the convergence κ and subsequently, the lensing potential ψ (16), the shear γ , and the deflection angle α for a light bundle within a light cone are derived. This provides a discretization of the light propagation equations (Sect. 3.2, see also Seitz et al. 1994). To avoid the repeated encounter of light rays with the same object at different snapshot times, boxes are usually rotated and translated randomly. This reduces but does not eliminate spurious correlations of structure across different redshifts, the importance of which depends on the simulation size.

Potential, shear, and the deflection angle can be calculated from the convergence on a grid via FFT, making use of the periodic boundary conditions of the box, or in real space via finite differences (Hilbert et al. 2009). Usually a smoothing step has to be involved here due to the discreteness of the simulated density field represented by point masses. Subsequently, lensing deflections are obtained from the smoothed density field. Alternatively, one can adapt the resolution according to local density, allowing lensing quantities to be obtained directly from the simulated particles (Aubert et al. 2007). However, in any case smoothing of the density field is necessary to reduce Poisson noise, and to avoid singularities from deflection by point masses. Various smoothing schemes and density estimators have been proposed (Schaap & van de Weygaert 2000, Bradač et al. 2004, Kiessling et al. 2011, Angulo et al. 2014).

In the simplest case, the lensing contributions are added up along straight lines of sight, corresponding to the Born approximation of light deflection along the unperturbed path (Sect. 3.3; Refsdal 1970, Schneider & Weiss 1988).

4.2.2. Tracing the photons A further refinement of the “ray-shooting” method introduced in the last section is “ray-tracing”, where light rays are followed to the next plane along the deflected direction calculated on the current lens plane (Blandford & Narayan 1986, Jain et al. 2000). This multiple-plane approach takes into account non-linear couplings between lens planes and generates a non-symmetrical Jacobi matrix. With respect to the first-order cosmic shear convergence power spectrum P_κ , those higher-order corrections are very small on relevant scales: The E-mode power spectrum due to lens-lens couplings is four orders of magnitude smaller than P_κ . B-mode power is created at about the same level (Hilbert et al. 2009, Krause & Hirata 2010). The non-symmetrical, rotational contribution is about three orders below P_κ (Jain et al. 2000).

In the multiple-plane approach there is no one-to-one and onto mapping between the light cone of emitted rays at high redshift and the observer’s field of view. To guarantee that each photon reaches the observer, light rays are traced backwards from the observer to the emitting redshift, instead of forward propagation towards the observer.

For accurately simulating galaxy-galaxy lensing (Sect. 3.12), ray-shooting is insufficient, since weak-lensing-induced changes in the positions of background galaxies with typical deflection angles of order several arcmin. To preserve the correlation between lens galaxies and foreground matter structures, tracing of the deflected photon ray positions is necessary (Hilbert et al. 2009).

4.2.3. Approximations Several subtleties and further implicit approximations have to be mentioned here. **First**, a snapshot is a fixed point in time, neglecting any evolution or redshift-dependence of light deflection for the duration of light crossing the box. Thus, the box size should be not more than about 300 Mpc. For larger simulations, boxes can be split and projected onto more than one lens plane. This however causes problems when cutting through halos, and leads to loss of large-scale power. Alternatively, the field of view is generated under a skewed angle with respect to the box. By choosing an appropriate angle, repeated structures can be largely reduced, and lens planes with periodic boundaries can be constructed (Hilbert et al. 2009).

Second, the lens planes are parallel to each other, which means that the projection of matter neglects the sky curvature, and the fact that the gradient of the lensing potential is necessarily taken in the lens plane and not orthogonal to the light ray. Both approximations remain accurate if the light cone is small, on the order of a few degrees.

Third, most N -body codes only simulate Newtonian physics. Relativistic corrections to lensing observables due to General Relativity are however very small (Thomas et al. 2014). To explore deviations from GR, simulations in modified gravity models have been introduced recently (e.g. Li et al. 2012).

4.2.4. Further methods To circumvent lens-plane projections altogether, the lensing signal can be computed on the fly during the N -body run. For the ray-shooting technique, where light trajectories are known before-hand, the lensing quantities can be calculated by approximating the integral (15) with a discrete sum evaluated at the time steps of the simulation (White & Hu 2000, Li et al. 2011). With relative scale factor ratios of typically $\Delta a/a \approx 0.01 - 0.03$, the time resolution is of the same order if slightly higher than usual separations of lens planes with $\Delta a/a \approx 0.03 - 0.05$. The implementation of this method is straightforward for ray-shooting, but becomes more difficult for propagation along the perturbed light ray (Li et al. 2011). An alternative method to allow for ray-tracing is to store the density field at each time step on a surface that moves at the speed of light toward an observer in the centre of the box (Teyssier et al. 2009).

4.2.5. Full-sky lensing simulations Upcoming and future large cosmic shear surveys require simulations covering a substantial part of the full sky. Such simulations are also used for CMB lensing. This requires taking steps beyond the small-angle fields of view and the plane-parallel approximation. Spherical density shells generated on the fly are transformed into lens spheres instead of Cartesian planes (Fosalba et al. 2008, Das & Bode 2008, Teyssier et al. 2009, Becker 2013). Lensing quantities are calculated using spherical geometry.

4.3. Dark matter and hydro-dynamical simulations

Dark matter interacts gravitationally, which for weak fields is a linear problem. Pure dark-matter N -body simulations are essentially solutions for Newton's equations of motion. Fast, parallel computers and massive memory and storage space allows for very accurate, high-resolution simulations spanning a wide range of scales and dynamic range. For an overview over various methods and codes, some of which publicly available, see Dolag et al. (2008).

Baryonic interactions however are much more complicated and not well known in detail. Already the simplistic approximation of the baryonic content as an ideal fluid introduces a set of non-linear equations, which further couple baryons and dark matter gravitationally. Additional physics is necessary for realistic simulations, consisting for example in radiative cooling, star formation, supernova feedback, magnetic fields, black hole and AGN feedback, and cosmic rays. Many of those processes are only poorly known and understood.

4.4. Baryonic effects on lensing observables

Baryons alter the profile of halos compared to pure collisionless dark matter. The changes to the power spectrum happen on small scales. Baryons play only a very minor role on large scales ($k \lesssim 1 h \text{Mpc}^{-1}$ or $\ell \lesssim 800$), since most of the dissipational physics takes place within virialized halos (Rudd et al. 2008). On intermediate scales, the gas distribution is more diffuse compared to dark matter, due to pressure which suppressed the formation of structure in the range of $k \approx 1$ to $10 h \text{Mpc}^{-1}$. On the other hand, baryonic cooling and dissipation leads to the condensation of baryons into stars and galaxies, increasing the density in the inner halo regions, leading to a stronger clustering at very small scales of $k \gtrsim 10 h \text{Mpc}^{-1}$ (Jing et al. 2006, Rudd et al. 2008, Semboloni et al. 2011a).

Future surveys require the knowledge of the total, dark + baryonic matter power spectrum at the 1 – 2 percent level, with the highest required sensitivity being at scales between $k = 0.1$ and $10 h \text{Mpc}^{-1}$, corresponding to a few to a few tens of arcmin on the sky (Huterer & Takada 2005, Eifler 2011). The convergence power spectrum is significantly altered at angular scales corresponding to $\ell \leq 1000$ to $\ell \leq 3000$, depending on the assumed statistical uncertainty. This result has also been found using semi-analytical models (White 2004, Zhan & Knox 2004).

Some past and present cosmological results have been obtained by leaving out small, very non-linear scales. Attempts to model baryonic effects on the total power spectrum have been made in the framework of the halo model. Modifications to halo properties like the density profile or the concentration parameter have been calibrated with numerical simulations (Rudd et al. 2008, Semboloni et al. 2011a, Fedeli et al. 2014). An alternative ansatz of mitigating the uncertainty of baryonic effects is self-calibration using additional information on the internal halo structure (Zentner et al. 2008), or on the lensing bispectrum (Semboloni et al. 2013b).

5. Cosmology from cosmic shear

This section gives a brief overview of the techniques to obtain constraints on cosmological parameters from cosmic shear.

5.1. Covariance estimation

The covariance matrix of weak-lensing observables is an essential ingredient for cosmological analyses of cosmic shear data. Shear correlations at different scales are not independent but correlated with each other: The cosmic shear field is non-Gaussian, in particular on small scales, and different Fourier modes become correlated from the non-linear evolution of the density field. This mode-coupling leads to an information loss compared to the Gaussian case (unless higher-order statistics are included). If not taken into account properly, error bars on cosmological parameters will be underestimated.

Additionally, even in the Gaussian case Fourier modes are spread on a range of angular scales in real space, causing shear functions to be correlated across scales. The correlation strength depends on the filter function relating the power spectrum to the real-space observable (Sects. 3.8, 3.9). The broader the filter, the stronger is the mixing of scales, and the higher is the correlation.

For an observed data vector $\mathbf{d} = \{d_i\}, i = 1 \dots m$, the covariance matrix \mathbf{C} is defined as

$$C_{ij} = \langle \Delta d_i \Delta d_j \rangle = \langle d_i d_j \rangle - \langle d_i \rangle \langle d_j \rangle, \quad (51)$$

where the brackets denote ensemble average.

In a typical cosmic shear setting, the data vector \mathbf{d} consists of functions of shear correlations (e.g. the shear two-point correlation function at m angular scales θ_i , or band-estimates of the convergence power spectrum P_κ at m Fourier wave bands with centres ℓ_i). Those functions are

quadratic in the observed galaxy ellipticity ε . The covariance then depends on fourth-order moments of ε . From (26), one can see that the covariance can be split into three terms: The shot noise, which is proportional to $\langle |\varepsilon^s|^2 \rangle^2 = \sigma_\varepsilon^4$, and, in the absence of intrinsic galaxy alignment (Sect. 3.11), only contributes to the covariance diagonal; the cosmic variance term, which depends on fourth moments of the shear; and a mixed term.

In particular the cosmic variance term is difficult to estimate since it requires the knowledge of the non-Gaussian properties of the shear field. Note that in the case of 3D lensing (Sect. 3.10.2), the vector \mathbf{d} consists of the observed galaxy shapes (in harmonic space), and the covariance is quadratic in the shear, and does therefore consist of a signal covariance, which is proportional to the convergence power spectrum P_κ , and a noise contribution $\propto \sigma_\varepsilon$.

5.1.1. The Gaussian approximation The covariance of the convergence power spectrum P_κ at an individual mode ℓ in the Gaussian approximation is the simple expression (Kaiser 1992, Kaiser 1998, Joachimi et al. 2008)

$$\langle (\Delta P_\kappa)^2 \rangle(\ell) = \frac{1}{f_{\text{sky}}(2\ell + 1)} \left(\frac{\sigma_\varepsilon^2}{2\bar{n}} + P_\kappa(\ell) \right)^2. \quad (52)$$

Here, the survey observes a fraction of sky f_{sky} , with a number density of lensing galaxies \bar{n} . The quadratic expression expands into shot-noise (first term), cosmic variance (second term), and a mixed term. In this Gaussian approximation, the fourth-order connected term of κ is zero, and the cosmic variance consists of products of terms second-order in κ .

Analytical expressions for the Gaussian covariance of real-space second-order estimators have been obtained in (Schneider et al. 2002a, Kilbinger & Schneider 2004, Semboloni et al. 2009). The power-spectrum covariance for shear tomography is easily obtained (Takada & Jain 2004).

5.1.2. Non-Gaussian contributions Equation (52) can be extended to the case of a non-Gaussian convergence field. For example, terms of order four in κ can be parametrized as integrals over the trispectrum T_κ (Scoccimarro et al. 1999, Takada & Jain 2004).

Non-Gaussian evolution leads to a further coupling of small-scale modes with long wavelength modes that are larger than the observed survey volume. These super-survey modes were first introduced as *beat coupling* in (Hamilton et al. 2006), and later modeled in the halo model framework as *halo sample variance* (HSV; Sato et al. 2009, Kayo et al. 2013). Contrary to the other terms of the covariance that scale inversely with the survey area f_{sky} , the super-survey covariance decreases faster. Therefore it is important for small survey areas (Sato et al. 2009). A rigorous treatment of the non-Gaussian covariance including super-survey modes is presented in Takada & Hu (2013).

The non-Gaussian cosmic variance has been fitted to N -body and ray-tracing simulations, providing fitting functions in terms of the Gaussian cosmic variance (Semboloni et al. 2007, Sato et al. 2011b). Using the halo model, the trispectrum contributions to the covariance can be computed (Sato et al. 2009, Takada & Hu 2013), including expressions for the bispectrum covariance (Kayo et al. 2013, Sato & Nishimichi 2013).

An alternative, non-analytic path to estimate the covariance matrix is replacing the ensemble average in (51) by spatial averaging. This requires a large enough number of independent or quasi-independent lines of sight n , to have a fair representation of the LSS. These lines of sight can be either numerical simulations or the observed survey itself. For the resulting matrix to be non-singular, the dimension of the data vector m has to be smaller than n . The corresponding estimator is unbiased; however, the inverse of this estimate, being a non-linear operation, is not. It is the inverse covariance that is needed for the likelihood function (see following section). The bias can be calculated and

removed in the Gaussian case (Anderson 2003). This debiasing also works reasonably well for non-Gaussian fields, and overestimates error bars by less than 5% if m/n is smaller than about 0.1 (Hartlap et al. 2007). For current surveys with a few redshift bins and reasonably small number of angular scales, resulting in a total $m \lesssim 100$, a few hundred realisations are sufficient. Future surveys, with many redshift bins and multiple galaxy population subsamples, have m of order a few thousand. To reach percent-level precision, the number of realisations has to be at least a few times 10^4 (Taylor et al. 2013, Dodelson & Schneider 2013).

Estimating the covariance from numerical simulations offers the additional advantage that systematic effects are relatively easy to include, for which analytical expressions are difficult to obtain. By populating simulations with galaxies and modeling their properties, effects such as photo- z errors, shape measurement biases, or intrinsic alignment can be included into the covariance matrix.

A further complication is that super-survey modes may not be fully captured by sample variance from numerical simulations, since the latter often lacks large-scale modes due to small box sizes or periodic boundaries. Including these modes requires special care in the simulation set-up (Li et al. 2014).

5.2. The likelihood function

To compare weak-lensing observations to theoretical predictions, one invokes a likelihood function L as the probability of the observed data \mathbf{d} given a model M with a set of parameters \mathbf{p} of dimension q .

For simplicity, in most cases, the likelihood function is modeled as an m -dimensional multi-variate Gaussian distribution,

$$L(\mathbf{d}|\mathbf{p}, M) = (2\pi)^{-m/2} |\mathbf{C}(\mathbf{p}, M)|^{-1/2} \exp \left[-\frac{1}{2} (\mathbf{d} - \mathbf{y}(\mathbf{p}, M))^t \mathbf{C}^{-1}(\mathbf{p}, M) (\mathbf{d} - \mathbf{y}(\mathbf{p}, M)) \right]. \quad (53)$$

The function \mathbf{y} is the model prediction for the data \mathbf{d} , and depends on the model M and parameter vector \mathbf{p} . This is only an approximation to the true likelihood function, which is unknown, since shear correlations are non-linear functions of the shear field, which itself is not Gaussian, in particular on small scales.

The true likelihood function can be estimated by sampling the distribution using a suite of N -body simulations for various cosmological parameters. Because of the high computation time, this has been done only for a restricted region in parameter space (Hartlap et al. 2009, Pires et al. 2009a, Takahashi et al. 2011).

In contrast, analytical approaches might be promising to determine the true likelihood function. Transforming the data to obtain more Gaussian distributions involves Gaussianizing the convergence (Joachimi et al. 2011b, Seo et al. 2011, Yu et al. 2012), or transforming the correlation function (Schneider & Hartlap 2009, Wilking & Schneider 2013). The so-called copula can be used to reconstruct the multi-variate probability distribution function (pdf) from one-dimensional pdfs (Sato et al. 2011a). Further, a lognormal distribution (Taruya et al. 2002, Hilbert et al. 2011) might be a better approximation to the convergence field.

The log-likelihood function can be approximated by a quadratic form, which is the inverse parameter covariance at the maximum point, called the *Fisher matrix* (Kendall & Stuart 1969, Tegmark et al. 1997). This approximation is exact in the case of a Gaussian likelihood function *and* Gaussian distributed parameters, but does not account for non-linear parameter degeneracies, nor non-Gaussian tails of the likelihood. The diagonal of the Fisher matrix inverse represents minimum parameter variances. This is very useful to quickly generate predictions of parameter constraints without the need of a time-consuming exploration of the parameter space (see following section). The Fisher matrix has become a standard tool to assess the performance of planned surveys, or to explore

the feasibility of constraining new cosmological models, e.g. (Albrecht et al. 2006). Marginalising over an arbitrary number of nuisance parameters, and modeling parameter biases (Huterer & Takada 2005) are easily incorporated. However, one has to keep in mind that the Fisher matrix is often ill-conditioned, in particular in the presence of strong parameter degeneracies, and its inversion requires a very high precision calculating of theoretical cosmological quantities (Wolz et al. 2012).

In most cases, the parameter-dependence of the covariance in (53) is neglected, since the computation of the covariance is very time-consuming, e.g. when derived from N -body simulations. When estimated from the data themselves, the cosmology-dependence of the covariance is missing altogether. This is a good approximation, as was shown in Eifler et al. (2009) and confirmed in Kilbinger et al. (2013), in particular when only a small region in parameter space is relevant, for example in the presence of prior information from other cosmological data.

5.3. Parameter estimation

Theoretical models of cosmic shear observables can depend on a large number of parameters. Apart from cosmological parameters, a number of additional, nuisance parameters might be included to characterize systematics, calibration steps, astrophysical contaminants such as intrinsic alignment, photometric redshift uncertainties, etc. The number of such additional parameters can get very large very quickly and reach of the order a few hundred or even thousands, for example if nuisance parameters are added for each redshift bin (Bernstein 2009).

When inferring parameter constraints within the framework of a given cosmological model, one usually wants to estimate the probability of the parameter vector \mathbf{p} given the data \mathbf{d} and model M . In a Bayesian framework, this is the *posterior* probability π , which is given via Bayes' theorem as

$$\pi(\mathbf{p}|\mathbf{d}, M) = \frac{L(\mathbf{d}|\mathbf{p}, M)P(\mathbf{p}|M)}{E(\mathbf{d}|M)}, \quad (54)$$

which links the posterior to the likelihood function (see previous section) via the *prior* P and the *evidence* E . In most cases, one wants to calculate integrals over the posterior, for example to obtain the mean parameter vector, its variance, or confidence regions. Such integrals can be written in general as

$$I(h) = \int d^q p h(\mathbf{p})\pi(\mathbf{p}|\mathbf{d}, M), \quad (55)$$

where h is a function of the parameter \mathbf{p} . To calculate the mean of the α^{th} parameter, $I(h) = \bar{p}_\alpha$, $h(\mathbf{p}) = p_\alpha$. For the variance of p_α , set $h(\mathbf{p}) = (p_\alpha - \bar{p}_\alpha)^2$. For a confidence region \mathcal{C} (e.g. the 68% region around the maximum) h is the characteristic function $1_{\mathcal{C}}$ of the set \mathcal{C} , that is $h(\mathbf{p}) = 1$ if \mathbf{p} is in \mathcal{C} , and 0 else. Note that this does not uniquely define \mathcal{C} ; there are indeed many different ways to define confidence regions.

In high dimensions, such integrals are most efficiently obtained by means of Monte-Carlo integration, in which random points are sampled from the posterior density function. Many different methods exist and have been applied in astrophysics and cosmology, such as Monte-Carlo Markov Chain (MCMC; Lewis & Bridle 2002), Population Monte Carlo (Wraith et al. 2009, Kilbinger et al. 2010), or Multi-nested sampling (Feroz & Hobson 2008). Monte-Carlo sampling allows for very fast marginalization, for example over nuisance parameters, and projection onto lower dimensions, e.g. to produce 1D and 2D marginal posterior constraints. MCMC provides a chain of N points \mathbf{p}_j , which under certain conditions represent a sample from the posterior distribution π . Using this Markov chain, integrals of the form (55) can be estimated as sums over the N sample points \mathbf{p}_j ,

$$\hat{I}(h) = \frac{1}{N} \sum_{j=1}^N h(\mathbf{p}_j). \quad (56)$$

Other Monte-Carlo sampling techniques might provide samples under a different distribution, and (56) has to be modified accordingly.

Alternatively, in a frequentist framework, one can minimize the function $\chi^2 = -2 \ln L$. This implicitly assumes flat priors on all parameters.

Cosmic shear using current data is sensitive to only a few cosmological parameters, in particular Ω_m and σ_8 . Shear tomography is beginning to obtain interesting results on other parameters such as Ω_K , or w . For parameters that are not well constrained by the data, for example Ω_b or h , the (marginal) posterior is basically given by the prior density. Therefore, the prior should be chosen wide enough to not restrict other parameters, and result in overly optimistic constraints.

6. Measuring weak lensing

6.1. Data analysis methods for weak lensing

The cosmological interpretation of cosmic shear measurements requires the observation of large and deep sky areas in superb image quality, together with sophisticated image analysis methods. **First**, the cosmological distortion induced on an individual galaxy is typically much smaller than the galaxy's intrinsic ellipticity. A significant detection of cosmic shear requires a very large number of galaxies to high redshifts and low signal-to-noise ratios, necessitating very wide and deep images at high resolution. The shapes of those faint galaxies have to be measured with high accuracy (Sect. 6.2). **Second**, galaxy images are corrupted by the *point-spread function* (PSF). The PSF is the combined effect of the imaging system consisting of the atmosphere (for ground-based surveys), telescope optics, and detector. The anisotropic part of the PSF creates spurious correlations of galaxy shapes which, if uncorrected, are typically larger than the cosmological shear correlations. To estimate the PSF, a very pure sample of stars, uncontaminated by small galaxies, has to be selected (Sect. 6.3). **Third**, any method of galaxy shape measurement and PSF correction has to be calibrated, to ensure that measurement biases are small enough compared to the statistical errors. This can be achieved by using large sets of image simulations that include properties of the survey and the lensing galaxy population as realistically as possible (Sect. 6.4). **Fourth**, the interpretation of measured shape correlations depends crucially on the redshift distribution of the lensed galaxy sample, see (22). The large number of lensing galaxies prohibits obtaining this distribution using spectroscopy. Instead, multiple optical band observations are necessary to estimate photometric redshifts (Sect. 6.5).

6.2. Galaxy shape measurement

One of the greatest challenges of cosmological weak lensing is shape measurement. High-redshift lensing galaxies, carrying the bulk of the cosmological signal, are faint objects with typical *i*- or *r*-band magnitudes of around 24, signal-to-noise ratios down to $S/N \sim 10$, and sizes of the order arcsec, thus extending over just a handful of pixels. Those galaxies are convolved with a spatially and temporally varying PSF of similar size. It is not required that an individual galaxy shape be measured with high precision; what is important instead is an unbiased measurement for a sample of galaxies. How small the residual bias can be depends on the survey size and depth, which drives the expected precision of cosmological parameters to be measured. Current surveys measure the sample galaxy ellipticity to about 1% accuracy, but the next generation of surveys needs to improve this by an order of magnitude (Huterer et al. 2006, Amara & Réfrégier 2007, Kitching et al. 2009, Amara et al. 2010, Cardone et al. 2014).

There are two main families of methods to measure the ellipticity ϵ of a galaxy image with light distribution $I(\theta)$. The **first** family directly estimates the ellipticity from the data, for example

by measuring second moments of I , or by decomposing I into basis functions, and extracting the ellipticity from the corresponding coefficients (Sect. 6.2.1). These direct techniques are generally more sensitive to the pixel noise compared to the fitting methods, but they also require fewer assumptions about I . However, no method is model- or assumption-*free* in principle. The **second** approach is to assume a model for the surface brightness I , including ellipticity parameters, and to fit the model to the observed image (Sect. 6.2.2). One of the advantages of these *forward-fitting* methods is the straightforward treatment of the PSF: The model is easily convolved with the PSF before comparing it to the data.

For all approaches, there are complications coming from the fact that weak-lensing galaxy images usually consist of multiple exposures. This observation strategy increases the image depth, and helps to fill gaps between the CCDs of modern multi-chip mosaic wide-field cameras. Two options are possible to perform the shape measurement: on single exposures images, or on a stacked image. The stacked image is obtained after a complex co-addition procedure, which consists in astrometrically aligning the individual images first, and interpolating pixel values of the individual frames to a new, common pixel grid. Although the stacking approach offers the advantage of higher signal-to-noise ratio per image, it has been shown for some shape measurement methods to limit their accuracy: The interpolation of the individual frames necessitates small image transformations to match the astrometry between exposures. This produces distortions in the PSF, and correlated pixel noise. Further, PSFs from different exposures usually have different shapes. Averaging over those PSFs is far from optimal, and can lead to a highly complex stacked PSF (Miller et al. 2013).

To avoid these difficulties with stacked images, there are various other ways to combine the individual exposures to yield a single galaxy shape estimate: shapes can be measured on individual images and then be averaged (Bernstein & Jarvis 2002); the (Bayesian) posterior probabilities of model fits on each image can be multiplied (Miller et al. 2007); a common model can be fitted jointly to all exposures. See Sect. 6.2.2 for more details on model-fitting shape methods.

Galaxy shapes are usually measured in one optical band, which is observed in the best-seeing nights. Combining different bands does improve the measurement, although the correlation of measured galaxy shapes from different wavelengths has to be accounted for (Jarvis & Jain 2008).

6.2.1. Direct estimation methods One can further sub-classify the first class of direct measurements techniques into perturbative and non-perturbative approaches. For the perturbative approach we find most notably KSB (Kaiser, Squires & Broadhurst 1995), which measures ellipticity using weighted second moments of the galaxy light distribution, and approximates the convolution of the image with the PSF by linear operations on the ellipticities. Various significant improvements of KSB have been achieved (Luppino & Kaiser 1997, Hoekstra et al. 1998, Kaiser 2000, Bernstein & Jarvis 2002), including an extension to higher perturbation order (Okura & Futamase 2009), originally developed for the measurement of flexion (Okura et al. 2007, see also Sect. 8.5). Alternatively, instead of correcting the ellipticities as in KSB, the PSF-deconvolution can be done directly on the moments of the galaxy light distribution (Rhodes et al. 2000). This is more rigorously explored using a truncated hierarchy of higher-order moments in Melchior et al. (2011).

The non-perturbative approach consists in assuming that the noise-free lensing galaxy profile can be decomposed into a set of orthogonal eigenfunctions, dubbed *shapelets* in the original paper (Refregier 2003). If the PSF can also be represented by the same set, the convolution of the galaxy with the PSF is a simple sum over the eigenfunctions, reducing the shape measurement and PSF correction process in principle to a simple matrix inversion problem. Several families of basis functions have been proposed (Bernstein & Jarvis 2002, Refregier 2003, Refregier & Bacon 2003, Massey & Refregier 2005, Kuijken 2006, Ngan et al. 2009, Andrae et al. 2011). In practice one has to truncate the

infinite eigenfunction expansion. This leads to biases, since the coefficients representing the ellipticity and the ones that have been truncated are typically correlated, due to noise and the presence of the PSF. Therefore, the measured ellipticity is biased compared to the true ellipticity from the hypothetical case of an infinite expansion and perfect representation of the galaxy (Bernstein 2010). Additionally, limiting the number of degrees of freedom is necessary to avoid the over-fitting of noise features. All shapelet methods seem to share the tendency of not well representing the galaxy light profile (Melchior et al. 2010). To date, none of these techniques have been used on optical data for shape measurement in the framework of cosmic shear. However, shapelets have been employed using radio data (see Sect. 8.2), galaxy-galaxy flexion (Velandar et al. 2011), and for weak lensing by clusters (Bergé et al. 2008, Romano et al. 2010). Further, the orthogonal eigenfunctions in the Bernstein & Jarvis (2002) variant have been employed to characterise and interpolate the PSF across the field in Jarvis et al. (2003).

6.2.2. Model-fitting methods The first model-dependent, forward-fitting technique was proposed in Kuijken (1999). However, only in the last five years or so has model-fitting become a widely used and very successful approach. It can be mathematically designed to work with low signal-to-noise images, allowing for measuring shapes from individual exposures instead of the stacked image.

A fully Bayesian forward-fitting method is *lensfit*, which measures the posterior distribution of ellipticity for galaxies on individual exposures, and combines the results in a Bayesian way without information loss (Miller et al. 2007, Kitching et al. 2008, Miller et al. 2013). Further notable model-fitting methods are *gfit* (Gentile et al. 2012), *im2shape* and *im3shape* (Zuntz et al. 2013), and *StackFit*, the method used for the latest DLS (Deep Lens Survey) cosmic shear results (Wittman et al. 2006, Jee et al. 2013).

Challenges for model-fitting methods are to find a good model and parametrization to match the wide observed range of galaxy light distributions. A non-suitable profile will result in a *model bias* (Voigt & Bridle 2010). The number of parameters is equally important: A model with too few free parameters is not flexible enough and can also give rise to model bias (Bernstein 2010). Note that this case of under-fitting is similar to the truncation of the expansion in eigenfunctions for non-perturbative methods discussed above. On the other hand, too many parameters risk to fit the noise and can cause a bias from over-fitting.

For any Bayesian shear measurement method, a prior distribution of galaxy properties is required on input. This prior may originate for example from deep, high signal-to-noise images, either from a deeper sub-part of the survey, from external observations, or from simulations. This prior distribution is difficult to obtain, since one needs to sample a large and multi-dimensional space of galaxy properties.

6.2.3. Further approaches The auto-correlation of light over the whole image, without the necessity of detecting galaxies, was proposed as an alternative, model-independent approach for weak cosmological lensing (van Waerbeke et al. 1997). This technique has however never been tested on large surveys, and it is further lacking a formal procedure for accurate shape measurement.

Recently, two Bayesian inference methods were proposed. One approach is hierarchical multi-level Bayesian inference (*MBI*; Schneider et al. 2014), that constructs a joint posterior of shear, galaxy properties, and the PSF (along with other nuisance parameters) given the pixel data. The posteriors of individual galaxies are combined to infer population parameters of galaxies and the PSF, which are marginalised over to obtain the shear. The other Bayesian method is an approach developed by Bernstein & Armstrong (2014), which does not need to attribute ellipticities to individual galaxies. It estimates an approximation of the posterior probability of shear given observed properties of a

galaxy population. The prior distribution of those properties has to be inferred, for example from deep images.

Further, ellipticities can be inferred by comparing observed shape parameters to a learning sample of galaxies, using some classification scheme. In principle, any method can be used to measure shape parameters, and since it is applied to both observations and the learning set, potential shear biases cancel in principle (Tewes et al. 2012).

These last two methods are limited by the dimensionality, resolution, and completeness of the training sample.

6.2.4. Shape measurement biases One can make the very general statement that the non-linear dependence of ellipticity estimators on the light distribution in the presence of noise creates a bias, the so-called *noise bias*. This bias has been investigated for methods based on moments (Hirata et al. 2004) and model fitting (Refregier et al. 2012, Kacprzak et al. 2014). Some work has been done to explore methods that are linear in the pixel light to reduce the bias, for example using unnormalised shape estimators (Zhang & Komatsu 2011, Viola et al. 2014, Bernstein & Armstrong 2014). However, since the intrinsic flux variation of galaxies is very large, the price to pay for a small bias is a very large variance.

A further source of shape measurement biases are *ellipticity gradients*, which occur if the ellipticity is a function of the scale where it is measured, for example for galaxies with a bulge that is more circular than its disk, see Voigt & Bridle (2010), Bernstein (2010), and Sect. 6.3.2.

Shape biases can be characterised to first approximation by a multiplicative component \mathbf{m} , and an additive term \mathbf{c} . These bias parameters are given by the relation between observed and true ellipticity (Huterer et al. 2006, Heymans et al. 2006),

$$\varepsilon_i^{\text{obs}} = (1 + m_i)\varepsilon_i^{\text{true}} + c_i; \quad i = 1, 2. \quad (57)$$

The shear biases \mathbf{m} and \mathbf{c} are generally functions of galaxy properties and redshift. Current shape measurement methods provide shear estimates with m at the 1 to 10 percent level, and c between 10^{-3} and 10^{-2} . Typically, the measured shapes are corrected for those biases using calibration image simulations (Sect. 6.4). Possible additional ways to mitigate shear biases is their self-calibration using the weak-lensing data themselves (Huterer et al. 2006, Zhang 2010). Future surveys require the accuracy of calibrated shapes to be on the order of 0.1% (Huterer et al. 2006, Massey et al. 2013, Cropper et al. 2013).

6.3. PSF correction

The PSF is the response of the image system to a point source. Since stars are unresolved objects, they are the local (noisy) representation of the PSF, and can be used to correct galaxy images for the PSF.

The intrinsic size of the PSF from the optical system together with atmospheric turbulence (*seeing*) circularizes galaxy images, resulting in a decrease of shape correlations. Ground-based sites with excellent conditions have seeing disk of the order 0.5 – 0.7 arcsec in the optical. A seeing of larger than an arcsec or so dramatically reduces the depth and usability of cosmic shear data. PSF anisotropies originate from the atmosphere, optical aberrations, mirror deformations, tracking errors, CCD non-flatness and misalignments on the focal plane, and pixelation. (Jarvis et al. 2008, Hamana et al. 2013, Chang et al. 2013). The typical PSF anisotropy in ground-based images is up to 10%. Therefore, for a sub-percent measurement of a 1% cosmic shear, the PSF induced on galaxy images has to be corrected with a precision of one part in 100.

6.3.1. The PSF model To estimate the PSF at the position of a galaxy, one has to select stars on the image, measure their shape, and interpolate the resulting PSF to the position of the galaxy. **First**, this requires a sample of suitable stars, i.e. without saturated pixels, not hit by cosmic rays, and uncontaminated by galaxies. A common selection criteria is the identification of the *stellar locus* in a size-magnitude diagram. This is a region of bright and small objects that is relatively well isolated from resolved galaxies and unresolved, dim objects such as very faint galaxies and detection artefacts. Additionally, colour information can be added to classify stars and galaxies.

Second, the shape of stars is measured and, in the simplest case, their ellipticity parameters are extracted. To increase the precision of the PSF correction, more parameters of the stellar shape have to be included. These can be higher-order moments, or a pixellised postage stamp around each star, or coefficients of a decomposition into a set of basis functions.

Third, those parameters are interpolated onto the galaxy position. For ground-based observations in the past, this has usually been done with a two-dimensional polynomial or a rational function, and the choice of the interpolating function can affect the measured cosmic shear signal (Hoekstra 2004). A variety of interpolating schemes that differ from simple fitting of a smooth function have been proposed (Kitching et al. 2013, Bergé et al. 2012, Gentile et al. 2013). Alternatively, a physical model of the optics and its aberrations can be used (Jarvis et al. 2008). For mosaic multi-CCD cameras, discontinuities between chips are common and have to be accounted for in the PSF model, for example by performing fits on each chip individually (Miller et al. 2013). By correlating the observed PSF to the PSF model residuals, cases of over- and under-fitting can be diagnosed (Rowe 2010).

For space-based observations the number of stars per field is very low, making it difficult to fit an interpolating function over the currently available small fields of view. However, due to the lack of the stochastic atmospheric contribution to the PSF, and the high stability of the optical system, dense stellar fields can be used to construct a model of the PSF, e.g. using a principal component analysis (PCA; Jarvis & Jain 2004, Schrabback et al. 2010). A PCA model of the PSF on individual images is also a viable option for lensing measurements on stacked images, where stacking can create PSF discontinuities (Jee et al. 2013).

6.3.2. Colour effects For a general image system, the PSF varies with wavelength λ . For example for a diffraction-limited telescope, the PSF size is directly proportional to λ . Further, atmospheric refraction is chromatic. Stars have different spectral energy distributions (SED) than galaxies; in general they are Milky Way disk stars and therefore bluer than high-redshift galaxies. The PSF that is used to correct galaxy images is therefore not exactly the one with which these images are convolved, introducing a bias. This bias depends on the SED variation within the filter, which is the larger the broader the filter is. In particular for the planned satellite mission *Euclid* (Sect. 8.1) for which the wide optical transmission spans the optical filter range $R + I + Z$, this colour-dependence has to be taken into account, for example by adding information from other wavelengths (Cypriano et al. 2010, Alejandro Plazas & Bernstein 2012, Meyers & Burchat 2014).

An additional complication arises because in general, the SED of a galaxy varies spatially, and the projected 2D shape of a galaxy depends on the scale where it is measured. For example, a bulge+disk galaxy often has a spherical, red bulge, and a more elliptical, blue disk. The measured shape involves some (radial) weight function of the galaxy's light distribution, the colour of which in general does not correspond to the SED-weighted PSF. Thus, even if the PSF for all wavelengths was known, the galaxy is corrected with the 'wrong' PSF, introducing a bias in the inferred shape. To account for this *colour gradient* and the associated bias, one can, as in the case of the wavelength-dependent PSF, reduce the filter width, observe the sky in additional filters, or use an external galaxy

calibration set of sufficient size (Voigt et al. 2012, Semboloni et al. 2013a)

6.4. Image simulations

As we have discussed in Sect. 6.2.4, virtually all shape measurement methods suffer from measurement biases and require a large and representative sample of observed or simulated galaxies to calibrate these biases. Such a calibration set is also needed for methods that are constructed to provide (near-)unbiased estimates of shear. For example, Bayesian methods, use it to estimate the prior distribution of galaxy properties. An inappropriate prior will result in a biased shear estimate.

Such a calibration sample can be obtained from the deep part of a survey with significantly longer integrated exposure time than the main survey. The sky coverage of such very deep observations is however very limited; in cases like the Canada-France Hawaii Legacy Survey (CFHTLS, see Sect. 7.1.1) or Euclid the deep part covers only on the order of a percent of the main survey.

An alternative calibration approach is to use image simulations, of which a huge data volume can be created. These simulations need to have realistic survey characteristics, for example concerning the noise. Additionally, the distribution of galaxy properties need to be well covered, since shape biases depend on galaxy size, signal-to-noise ratio, ellipticity, type, etc., and the calibration needs to be done as a function of these properties.

Image simulations have been created as collaborative projects within the weak-lensing community, such as the Shear TEsting Project (STEP) with the two consecutive blind tests STEP1 (Heymans et al. 2006) and STEP2 (Massey et al. 2007a). Public challenges like the GRavitational lEnsing Accuracy Testing (GREAT) projects have been launched to reach out to a larger community, in particular computer science, to invite more ideas to tackle the problem of galaxy shape measurement. This contains GREAT08 (Bridle et al. 2009, Bridle et al. 2010), GREAT10 (Kitching et al. 2011a, Kitching et al. 2012a, Kitching et al. 2013), and GREAT3 (Mandelbaum et al. 2014), as well as two ‘‘Kaggle’’ crowdsourcing challenges (Kitching et al. 2012b, Harvey et al. 2014).

Those collaborative image simulation projects typically started under simple, well-controlled conditions, for example, a constant PSF, constant shear over the field, and analytical galaxy light distributions with high signal-to-noise. They then progressed to more complex and more realistic images, for example galaxy images based on observed HST deep fields. The purpose of those simulations is to test estimates of shear with amplitudes of a few percent to an accuracy at also the percent level. This is typically quantified in terms of multiplicative and additive bias (57). The number of simulated images is necessarily very large, producing hundreds of gigabytes of data.

After the end of those projects, the true input parameters, and in some cases the codes to generate the simulations (e.g. the galaxy image simulation toolkit `GalSim`; Rowe et al. 2014), were released to the public. This policy has been proven to be of great value for the weak-lensing community, as those simulations and results have been used extensively in subsequent work, to better understand the performance of existing methods, and to scrutinize and calibrate new shape measurement techniques.

6.5. Photometric redshifts

Weak lensing observables, being integrals along the line of sight weighted by the source galaxy distribution $n(z)$ (24), require knowledge of the latter if they are to be interpreted cosmologically. To first order, the mean redshift \bar{z} has to be determined, but also the shape of $n(z)$ plays an important role. The sensitivity of the cosmic shear power spectrum (29) to \bar{z} is comparable to its sensitivity with respect to cosmological parameters (Jain & Seljak 1997, Bernardeau et al. 1997). For example,

Huterer et al. (2006) find a rough estimate of $P_\kappa(\ell \sim 1000) \propto \Omega_{\text{de}}^{-3.5} \sigma_8^{2.9} \bar{z}^{1.6} |w|^{0.31}$. Clearly, for a desired accuracy on cosmological parameters, the mean redshift of sources has to be known to at least that accuracy, and to a much higher accuracy in the case of parameter on which the power spectrum has a weaker dependence such as w . For tomography, this is true for each individual bin, further exacerbating the demands on photometric redshifts. For example, the centroids of each bin have to be known to better than a per cent in order to limit the decrease in accuracy of dark-energy parameters to 50% (Huterer et al. 2006).

Spectroscopy of all the faint galaxies used for a typical weak-lensing survey is too costly, and redshifts have to be estimated from broad-band photometry, using the technique of *photometric redshifts*, or photo- z s. There are various methods to measure photometric redshifts. Template-based approaches perform χ^2 -type fits of (redshifted) template SEDs to the flux in the observed bands. Exemplary methods that have been used in a weak-lensing context include *LePhare* (Ilbert et al. 2006), *Bayesian Photometric redshift estimation* (BPZ; Benítez 2000), and *HyperZ* (Bolzonella et al. 2000). In contrast, various empirical approaches exist that typically require a training set of galaxies with spectroscopic redshifts, such as *ANNz* (Collister & Lahav 2004). Other methods do not attempt to measure individual redshifts, but apply statistical tools to the ensemble of observations, for example clustering in colour space (Jain et al. 2007, Lima et al. 2008).

Most photo- z methods not only yield an estimate \hat{z} of the redshift, but provide more information about the distribution, for example error bars, or a goodness-of-fit parameter. Ideally, they estimate the full probability distribution function. Additional outputs may be the galaxy type, and the probability of the object being a star.

The dispersion of current photometric redshifts is of the order $\sigma_z/(1+z) = 0.03 - 0.06$ for typical multi-band optical surveys. The rate of catastrophic outliers — galaxies whose estimated redshift is off from the true (spectroscopic) redshift by more than a couple of standard deviations — is between a few to a few tens of percent. All redshift estimates strongly depend on galaxy type: Elliptical galaxies usually have much smaller uncertainties than blue and irregular types.

The currently-reached amplitude of dispersion σ_z is sufficient for future surveys. However, they require σ_z to be known to sub-percent accuracy (Ma et al. 2006). Catastrophic outliers can strongly bias tomographic shear power spectra, and their rate has to be lower than a percent (Bernstein & Huterer 2010, Hearin et al. 2010). This rate is applied to the galaxy sample after possible rejection of likely outliers by the photometric redshift code. The required precision of photometric redshifts necessitates a very large spectroscopic calibration set. For current surveys, this number is on the order of ten thousand, and a magnitude larger for future surveys (Ma et al. 2006). The spectroscopic survey has to be a representative sample of the lensed galaxy population, covering all possible types and redshifts. In most cases however, the spectroscopic surveys are too shallow to be complete down to the limiting magnitude of weak-lensing galaxies, and suffer from a non-zero spectroscopic redshift failure rate.

Additional methods to assess the quality of photometric redshifts, and to recover the true redshift distribution, make use of the spatial clustering of galaxies. From the amount of cross-correlation of samples between different redshift bins one can deduce the amount of redshift outliers (Benjamin et al. 2010, Benjamin et al. 2013). Similarly, the cross-correlation of the photometric with a spectroscopic sample can reveal the true redshift distribution (Newman 2008), although this reconstruction is hampered by a possible redshift-dependent bias of the photometric galaxy sample (Schulz 2010).

6.6. Error modelling and residual systematics

Any weak lensing data analysis must be completed with a robust error modeling. This step is necessary to quantify any residual systematics caused by an imperfect PSF correction, since those residuals can mimic a cosmological signal. The most commonly used approach is a null test of the correlation between the stellar ellipticities ε^* (before PSF correction) and the corrected galaxy shapes ε . This star-galaxy ellipticity correlation function is defined as

$$\xi_{\text{sys}} = \langle \varepsilon^* \varepsilon \rangle. \quad (58)$$

There are two sources of noise contributions, statistical noise and sample variance: (1) The statistical noise is easy to estimate for the shear because it is caused by the uncorrelated intrinsic ellipticity dispersion σ_ε^2 of galaxies which can be known very accurately either from the lensing data themselves, or from deep, high-resolution space-based surveys. (2) Sample variance can create local, random alignments between the PSF ellipticity patterns and shear from the large-scale structure. Even though a perfect PSF correction leads to a zero expectation value of ξ_{sys} , there is a non-zero scatter, which exceeds the statistical-noise scatter of that estimator in the absence of cosmic shear. Heymans et al. (2012) showed that the distribution of ξ_{sys} can be measured including sample variance estimated from N -body simulations. By comparing the observed scatter of ξ_{sys} to the one from LSS simulations, one can statistically estimate the amount of PSF residual systematics.

Other null tests for detecting potential systematics in weak-lensing data look at correlations of the measured shear with quantities that should be independent of the shear, such as PSF size and shape, position on the CCD or in the field, etc.

A further test that has been used frequently in the past is the null detection of a B-mode dispersion, for example using the aperture-mass or the COSEBIs (Sect. 3.9). Note however that a small non-zero B-mode is expected from astrophysical sources (Sect. 3.14), and future surveys will have large enough statistical power to detect this B-mode. Moreover, this test does not catch systematic effects that only produce an E-mode pattern.

Additionally, it is important to test for potential redshift dependent systematics (Semboloni et al. 2009). For example, the shear biases m and c (57) likely depend on galaxy properties such as size, magnitude, or colour, which change with redshift. A simultaneous test of redshift-dependent shear biases and catastrophic photometric redshift outliers is the increase of the galaxy-galaxy lensing amplitude for a fixed foreground sample with increasing redshift of the background population. This increase is a purely geometrical effect and depends on the angular diameter distance between lens and source. This redshift-scaling shear test can help to identify the redshift range with the most reliable shear and photo- z quality (Heymans et al. 2012).

7. Observational results and cosmological constraints

7.1. Basic results

The following sections discuss the basic observational results from second-order cosmic shear statistics. The parameter combination that cosmic shear (including non-linear scales) is most sensitive to is $\sigma_8 \Omega_m^\alpha$, with $\alpha \approx 0.5 - 0.7$. Fig. 7 shows this combination measured in recent years. The corresponding data and original results used for this plot are listed in Table 7.1. Some data points in this figures are from third-order and 3D lensing. These results are discussed in more detail in Sects. 7.2 and 7.5.

7.1.1. Early era, 2000 - 2006 The first detection of weak gravitational lensing by the large-scale structure was reported in 2000 by four independent groups (Bacon et al. 2000, Kaiser

Table 1. Parameter values of $\sigma_8\Omega_m^\alpha$ used for Fig. 7. For different surveys (first column) the second column is the value rescaled to $\Omega_m = 0.3$ which is plotted in the figure, obtained from the original measurement (third column). The fourth column indicates the number of redshift bins, the column 5 is the reference.

Survey	$\sigma_8(\Omega_m/0.3)^\alpha$	original measurement	N_z	Reference
COSMOS	0.81 ± 0.17	$\sigma_8(\Omega_m/0.3)^{0.48} = 0.81 \pm 0.17$	1	Massey et al. (2007b)
COSMOS	$0.87^{+0.09}_{-0.07}$	$\sigma_8(\Omega_m/0.3)^{0.44} = 0.866^{+0.085}_{-0.068}$	3	Massey et al. (2007b)
100 deg ²	0.74 ± 0.04	$\sigma_8(\Omega_m/0.24)^{0.59} = 0.84 \pm 0.05$	1	Benjamin et al. (2007)
CFHTLS	0.70 ± 0.04	$\sigma_8(\Omega_m/0.25)^{0.64} = 0.785 \pm 0.043$	1	Fu et al. (2008)
CFHTLS	0.76 ± 0.08	$\sigma_8(\Omega_m/0.25)^{0.53} = 0.837 \pm 0.084$	1	Fu et al. (2008), large scales
COSMOS	0.75 ± 0.08	$\sigma_8(\Omega_m/0.3)^{0.51} = 0.75 \pm 0.08$	5+1 ^a	Schrabback et al. (2010)
COSMOS	0.65 ± 0.10	$\sigma_8(\Omega_m/0.3)^{0.62} = 0.65 \pm 0.1$	1	Schrabback et al. (2010)
COSMOS	$0.69^{+0.08}_{-0.14}$	$\sigma_8(\Omega_m/0.3)^{0.46} = 0.69^{+0.08}_{-0.14}$	1	Semboloni et al. (2011b), +IA
SDSS-Stripe82	$0.59^{+0.07}_{-0.12}$	$\sigma_8(\Omega_m/1.0)^{0.7} = 0.252^{+0.032}_{-0.052}$	1	Lin et al. (2012)
SDSS-Stripe82	$0.60^{+0.11}_{-0.14}$	$\sigma_8(\Omega_m/0.264)^{0.67} = 0.65^{+0.12}_{-0.15}$	1	Huff et al. (2014a)
SDSS-DR7	0.72 ± 0.05	$\sigma_8(\Omega_m/0.25)^{0.57} = 0.8 \pm 0.05$	1	Mandelbaum et al. (2013)
DLS	0.82 ± 0.04	$\sigma_8(\Omega_m/0.265)^{0.5} = 0.868 \pm 0.041$	1	Jee et al. (2013), priv. comm.
CFHTLenS	0.74 ± 0.03	$\sigma_8(\Omega_m/0.27)^{0.59} = 0.787 \pm 0.032$	1	Kilbinger et al. (2013)
CFHTLenS	$0.74^{+0.07}_{-0.06}$	$\sigma_8(\Omega_m/0.27)^{0.65} = 0.79^{+0.07}_{-0.06}$	1	Kilbinger et al. (2013), large scales
CFHTLenS	0.73 ± 0.04	$\sigma_8(\Omega_m/0.27)^{0.55} = 0.771 \pm 0.04$	2	Benjamin et al. (2013)
CFHTLenS	$0.74^{+0.03}_{-0.04}$	$\sigma_8(\Omega_m/0.27)^{0.46} = 0.774^{+0.032}_{-0.041}$	6	Heymans et al. (2013), +IA
CFHTLenS	0.66 ± 0.21	$\sigma_8(\Omega_m/0.27)^{0.46} = 0.69 \pm 0.22$	∞^b	Kitching et al. (2014)
CFHTLenS	1.11 ± 0.26	$\sigma_8(\Omega_m/0.27)^{0.44} = 1.16 \pm 0.27$	∞^b	Kitching et al. (2014), large scales
CFHTLenS	$0.73^{+0.07}_{-0.09}$	$\sigma_8(\Omega_m/0.27)^{0.57} = 0.77^{+0.07}_{-0.1}$	1	Fu et al. (2014), +IA
CFHTLenS	$0.79^{+0.03}_{-0.04}$	$\sigma_8(\Omega_m/0.27)^{0.64} = 0.84^{+0.03}_{-0.04}$	1	Liu et al. (2015)
SDSS-Stripe82	0.78 ± 0.03	$\sigma_8(\Omega_m/0.27)^{0.42} = 0.82 \pm 0.03$	1	Liu et al. (2014)
WMAP3 ^c	0.67 ± 0.07	$\sigma_8(\Omega_m/0.234)^{0.5} = 0.76 \pm 0.05$	-	Spergel et al. (2007)
WMAP5 ^c	0.74 ± 0.05	$\sigma_8(\Omega_m/0.258)^{0.5} = 0.796 \pm 0.036$	-	Komatsu et al. (2009)
WMAP7 ^c	0.77 ± 0.05	$\sigma_8(\Omega_m/0.273)^{0.5} = 0.811^{+0.03}_{-0.031}$	-	Komatsu et al. (2011)
WMAP9	0.79 ± 0.05	$\sigma_8(\Omega_m/1.0)^{0.5} = 0.434 \pm 0.029$	-	Hinshaw et al. (2013)
Planck2013	0.85 ± 0.03	$\sigma_8(\Omega_m/0.27)^{0.46} = 0.89 \pm 0.03$	-	Planck Coll. (2014a), $C(\ell)$
Planck2013	0.74 ± 0.02	$\sigma_8(\Omega_m/0.27)^{0.3} = 0.764 \pm 0.025$	-	Planck Coll. (2014b), SZ
Planck2015	0.83 ± 0.02	$\sigma_8(\Omega_m/1.0)^{0.5} = 0.4521 \pm 0.0088$	-	Planck Coll. (2015), $C(\ell)$

^a 5 narrow photo- z bins and one wide bin of faint galaxies.

^b 3D lensing, no z -binning.

^c The index $\alpha = 0.5$ is adopted from the WMAP9 measurement, published on <http://lambda.gsfc.nasa.gov>. The resulting values and errors are therefore only illustrative.

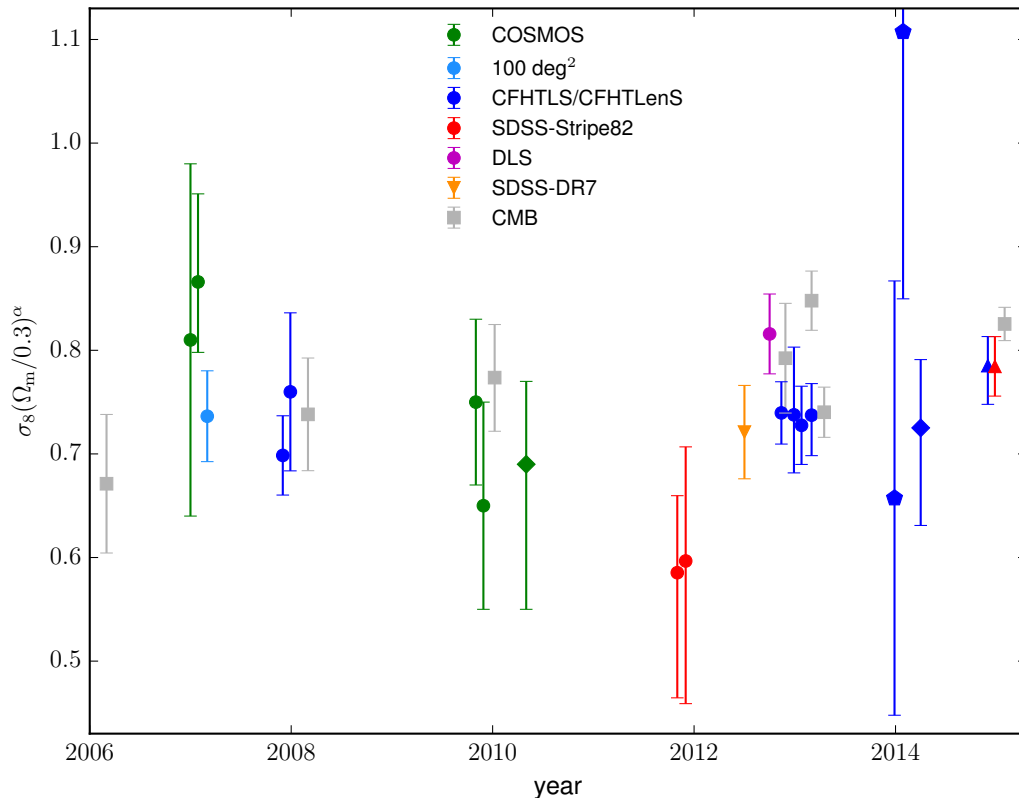


Figure 7. Mean and 68% error bars for the parameter $\sigma_8(\Omega_m/0.3)^\alpha$, for various cosmic shear observations, plotted as function of their publication date (first arXiv submission). All parameter values are given in Table 7.1. Different surveys are distinguished by colour as indicated in the figure. Data points are shown for second-order statistics (circles), third-order (diamonds), 3D lensing (pentagons), galaxy-galaxy lensing (+ galaxy clustering; triangle), and CMB (squares).

et al. 2000, Van Waerbeke et al. 2000, Wittman et al. 2000). The observations were taken with different cameras and telescopes — the Prime Focus Imaging Camera (PFIC) on the William-Herschel Telescope (WHT), UH8K and CFH12K on the Canada-France Hawaii Telescope (CFHT), and the Big Throughput Camera (BTC) on Blanco — and covered sky areas between 0.5 and 1.5 deg². These early analyses measured correlations of galaxy ellipticities that were larger than the expected residual systematics. Limits on Ω_m and σ_8 could be obtained.

Those exploratory results were very soon followed by other surveys from a wide range of telescopes, for example CFH12K/CFHT with the Red-sequence Cluster Survey (RCS) and VIRMOS-DESCART (Van Waerbeke et al. 2001, Van Waerbeke et al. 2002, Hoekstra et al. 2002*b*, Hoekstra et al. 2002*c*, van Waerbeke et al. 2005), FORS1 (FOcal Reducer and Spectrograph)/VLT (Very Large Telescope; Maoli et al. 2001), the 75-deg² survey with BTC/Blanco-CTIO (Jarvis et al. 2003, Jarvis et al. 2006), PFIC/WHT (Massey et al. 2005), ESI (Echelle Spectrograph and Imager)/Keck II (Bacon et al. 2003), WFI at MPG/ESO 2.2m with the Garching-Bonn Deep Survey (GaBoDS; Hettterscheidt et al. 2007), and Suprime-Cam/Subaru (Hamana et al. 2003).

Cosmic shear then was measured using MegaCam/CFHT on the Canada-France Hawaii Legacy Survey (CFHTLS). During five years this large program observed 170 square degrees in five optical bands. First results from the first data release were published over 22 deg² of the wide part (Hoekstra et al. 2006) and the 3 out of the 4 deg² of the deep part (Semboloni et al. 2005).

Apart from those ground-based observations, cosmic shear was successfully detected with the

Hubble Space Telescope (HST), using parallel archival data from the cameras STIS (Space Telescope Imaging Spectrograph; Hämmerle et al. 2002, Miralles et al. 2005, Rhodes et al. 2004), and WFPC2 (Wide Field Planetary Camera 2; Rhodes et al. 2001, Refregier et al. 2002, Casertano et al. 2003). Further HST cosmic shear results came from the Galaxy Evolution From Morphology And SEDs (GEMS) survey (Heymans et al. 2005, Schrabback et al. 2007).

Those early observations were done in only one optical filter, and the photometric redshift distribution $n(z)$ of source galaxies (Sect. 6.5) could not be measured from the data themselves. To estimate $n(z)$, external data were used by matching the survey depths. Those data were typically very deep but covered a very small area, such as the Hubble Deep Field (HDF) with 6.5 arcmin^2 , and the adopted redshift distribution suffered from a large cosmic variance (Van Waerbeke et al. 2006). A notable exception were cosmic shear results from the COMBO-17 survey observed with WFI at MPG/ESO 2.2m, (Brown et al. 2003), for which accurate photometric redshifts were available from 5 broad- and 12 narrow-band filters, with a precision of $\sigma_z/(1+z) = 0.02$ at $R = 23$ (Wolf et al. 2003). From a convergence band-power (2PCF) estimate using the method of Hu & White (2001), the constraints $\sigma_8(\Omega_m/0.3)^{0.49} = 0.72(0.75) \pm 0.09$ were obtained (Brown et al. 2003). Intrinsic alignment contaminations to this result were estimated to amount to 0.03, one third of the statistical errors (Heymans et al. 2004). Note that some of the five COMBO-17 fields were not selected randomly, but included the very empty CDFS (Chandra Deep Field South), and A901 with the $z = 0.16$ super-cluster Abell 901/902.

By 2006, there was a small but systematic tension in the fluctuations amplitude parameter σ_8 between different cosmic shear results. Some of the above-mentioned surveys such as GaBoDS, CFHTLS, and COSMOS yielded values of σ_8 of around 0.85, systematically higher than the CMB result from WMAP3 of $\sigma_8 = 0.76 \pm 0.05$ (Spergel et al. 2007). Other surveys such as COMBO-17 and the 75-deg² survey were in agreement with WMAP3. The scatter of σ_8 between cosmic shear results was larger than the statistical errors, which were typically between 0.05 and 0.15 (for a fixed $\Omega_m = 0.3$), see Hettterscheidt et al. (2007) for a compilation of pre-2007 results. These differences spurred a lot of activity into finding possible lensing systematics. The comparison and calibration of shape measurement methods had already started a few years earlier. The STEP project (Sect. 6.4), albeit using somewhat idealised simulations showed that cosmic shear could be measured with current methods to better than the statistical uncertainties (Heymans et al. 2006).

Many of those early surveys were clearly systematics-dominated, in some cases showing significant PSF residuals and B-modes, or using incorrect shear calibrations, resulting in biased measurements. In addition, the cosmological interpretation of these measurements requires the knowledge of the source galaxy redshift distribution. This turned out to be one of the main causes of bias to cosmological weak-lensing results. These problems were largely resolved in subsequent years, as is discussed in the following section.

7.1.2. Consolidating era, 2007 - 2012 The main advancement during these years was the improved estimation of the source galaxy redshift distribution. Large samples of multi-band observations resulted in accurate photometric redshifts that were calibrated using deep spectroscopic data from surveys that overlapped with the weak-lensing data. Furthermore, more realistic error estimates were included in cosmic shear analyses.

The third data release of the wide part of the Canada-France-Hawaii Telescope Legacy Survey (CFHTLS) with an observed area of 53 deg^2 provided 2D cosmic shear results out to very large, linear scales, (7.7 degrees, corresponding to 170 Mpc at the mean lens redshift of 0.5; Fu et al. 2008). This enabled cosmological constraints using large scales only, thereby reducing uncertainties from non-linear and baryonic physics on small scales. Using $\langle M_{\text{ap}}^2 \rangle(\theta)$ on scales $\theta > 85'$ the authors obtained

$\sigma_8(\Omega_m/0.25)^{0.53} = 0.837 \pm 0.084$. Simultaneously, the third-release CFHTLS data was combined with the previously completed surveys GaBoDS, RCS, and VIMOS-DESCART into the 100 deg^2 survey (Benjamin et al. 2007), doubling the area that was available from CFHTLS at that time. Both these studies used the photometric redshifts from the deep part of CFHTLS (Ilbert et al. 2006), taking into account sampling variance. The deep fields have an area of 4 square degrees, an increase of nearly a factor 2500 over the HDF.

The space-based COSMOS (COSmological Evolution Survey; Scoville et al. 2007) was a significant contribution to the field. This wide (1.64 deg^2) and very deep ACS (Advanced Camera for Surveys)/HST survey provided a density of source galaxies of about a factor of four larger compared to the deepest ground-based surveys (e.g. COMBO-17). A large number of multi-band follow-up observations from the ground allowed for accurate photometric redshifts. A first analysis was presented in 2007 (Leauthaud et al. 2007, Massey et al. 2007b). Using 15-band photo- z 's (Mobasher et al. 2007), the evolution of the shear signal between three redshift bins was demonstrated, although with estimated relative calibration errors of 5%. An independent re-analysis of the weak-lensing data (Schrabback et al. 2010) used improved photo- z 's from twice the number of bands (Ilbert et al. 2009). Due to the low number of high- S/N stars in ACS fields, and temporal instabilities of HST, the PSF model was obtained by PCA of the PSF pattern from dense stellar fields. This work presented a five-bin tomographic analysis, leading to constraints on the deceleration parameter $q_0 = -\ddot{a}a/\dot{a}^2 = \Omega_m/2 - \Omega_\Lambda$, with a detection of acceleration ($q_0 < 0$) at 94.3% confidence, including additional priors on h and Ω_b . The same data were used in Tereno et al. (2011) to verify the consistency with GR.

By that time, ground-based surveys had become large enough to enable detailed residual systematics tests. For CFHTLS, Kilbinger et al. (2009) as well as first multi-colour observations (Fu 2008) revealed an anomalous shear amplitude scaling with source redshift and a variance between MegaCam pointings larger than expected.

7.1.3. Survey era, 2013 - present The survey era provided measurements that relied on independently cross-checked photometric redshifts, and a robust estimate of residual systematics on weak-lensing shear correlations (Sect. 6.6). In these studies, the residual sytematics analysis were done completely independently from the cosmological parameters analysis, in order not to bias the cosmological results.

A milestone for cosmic shear represented the CFHT lensing survey (CFHTLenS; Erben et al. 2013). Photometric redshifts for each source galaxy were obtained in Hildebrandt et al. (2012), the robustness of which was verified using spectroscopic redshifts, COSMOS 30-band photo- z s, and a cross-correlation analysis (Benjamin et al. 2013). Galaxy shapes were measured on individual exposures with *lensfit* and calibrated using two independent suites of image simulations (Miller et al. 2013). An excess correlation between star and galaxy shapes (58) was found on 25% of the observed fields, which in turn were discarded from the cosmological analysis (Heymans et al. 2012). Two-dimensional cosmic shear correlation functions from CFHTLenS were presented in Kilbinger et al. (2013). A two-bin tomographic analysis was performed by Benjamin et al. (2013). The same tomographic data were used to place constraints on modified gravity (Simpson et al. 2013). Further, a six-bin tomographic analysis was performed where cosmological and intrinsic-alignment parameters were constrained simultaneously (Heymans et al. 2013). Late-type galaxies were found to not show any significant intrinsic alignment, while for early type galaxies IA was detected at about 2σ .

Cosmic shear results from the very deep, 20 deg^2 wide DLS (Deep Lens Survey) were presented in Jee et al. (2013), observed with the two 4 m telescopes Kitt Peak and Blanco. The PSF model was obtained using PCA, and calibrated by minimizing correlations between PSF residuals and PSF

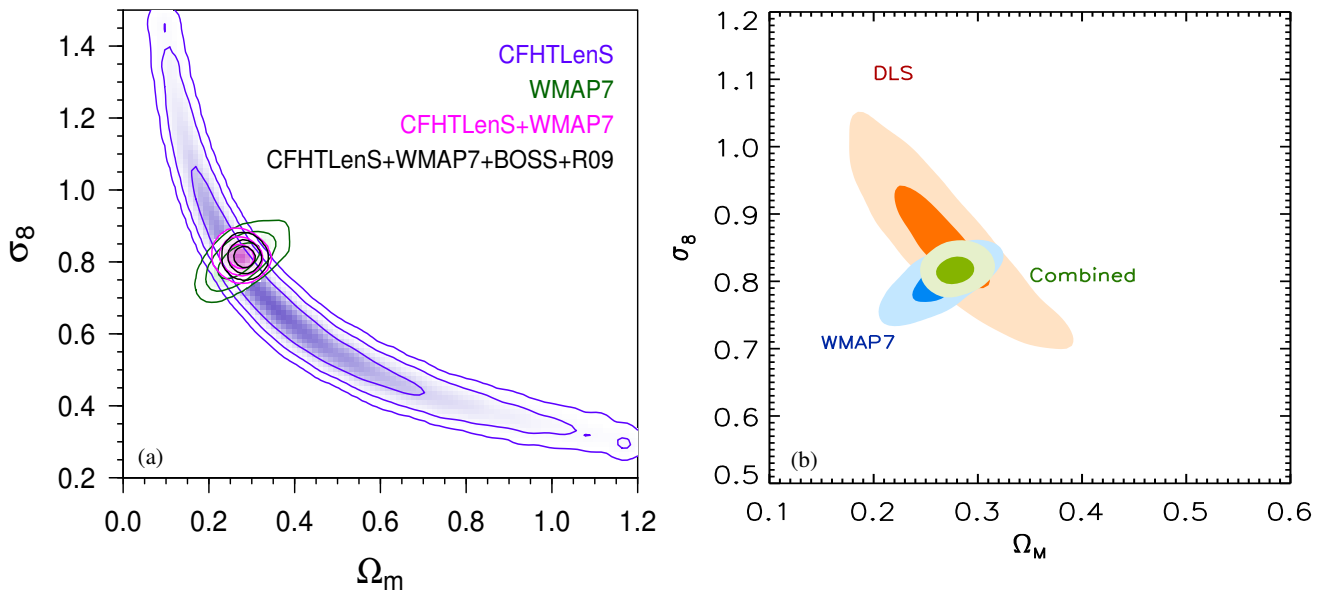
Flat Λ CDM

Figure 8. The near-orthogonality of Ω_m and σ_8 constraints from 2D cosmic shear and CMB. (a) CFHTLenS, WMAP7, BAO from BOSS (Anderson et al. 2012), and a HST H_0 prior (Riess et al. 2009, ‘R09’). From Kilbinger et al. (2013). (b) DLS including tight priors on Ω_b and H_0 . From Jee et al. (2013). Figure used with permission from Jee et al. (2013), *ApJ*, **765**, 74. Copyright 2013 IOP.

model (Rowe 2010).

Cosmic shear results were also obtained by SDSS (Sloan Digital Sky Survey). SDSS observations on 250 square degrees (168 after masking) of the Stripe-82 area are very shallow, with only 2 lensing galaxies per arc minute, and suffer from a large and strongly varying PSF (between 0.8 and 3.2 arcsec; Huff et al. 2014b). Despite these challenges, cosmic shear results were obtained from stacked images, presented in Lin et al. (2012) and Huff et al. (2014a)

For a Λ CDM cosmology, cosmic shear constrains a combination of Ω_m and σ_8 that is perpendicular to the one obtained from CMB (Contaldi et al. 2003). Adding cosmic shear to WMAP (Wilkinson Microwave Anisotropy Probe) results in typical reduction of error bars on Ω_m and σ_8 of up to 50%, similar to other low- z cosmological probes such as Baryonic Acoustic Oscillations (BAO). For example, the WMAP7 constraints of $\Omega_m = 0.273 \pm 0.03$ and $\sigma_8 = 0.811 \pm 0.031$ (Komatsu et al. 2011) get tightened when adding CFHTLenS, resulting in $\Omega_m = 0.274 \pm 0.013$ and $\sigma_8 = 0.815 \pm 0.016$ (Kilbinger et al. 2013). Similar constraints were obtained with DLS + WMAP7 + tight priors on h and Ω_b , with $\Omega_m = 0.278 \pm 0.018$ and $\sigma_8 = 0.815 \pm 0.020$ (Jee et al. 2013; see Fig. 8). Planck’s cosmological findings from temperature anisotropies (together with CMB lensing and WMAP polarization) correspond to a higher matter density and normalization compared to most previous probes, with $\Omega_m = 0.315 \pm 0.017$ and $\sigma_8 = 0.829 \pm 0.012$, or $\sigma_8(\Omega_m/0.27)^{0.46} = 0.89 \pm 0.03$ (Planck Coll. 2014a). This is consistent with CFHTLenS at the 2σ level, see Fig. 9. Further, Planck’s counts of Sunyaev-Zel’dovich (SZ) clusters results in a lower normalization of $\sigma_8(\Omega_m/0.27)^{0.3} = 0.78 \pm 0.01$ (Planck Coll. 2014b). Sect. 7.3 discusses whether adding extra-parameters such as massive neutrinos are needed to reconcile recent high- and low- z data.

A model with variable curvature does not change the cosmic-shear constraints on Ω_m and σ_8 by a lot. Pre-Planck CMB data alone cannot constrain the curvature of the Universe, and adding other probes such as measurements of H_0 or weak lensing are required. Planck and high-resolution ground-based millimetre-wavelength radio telescopes of similar sensitivity and resolution such as SPT (South

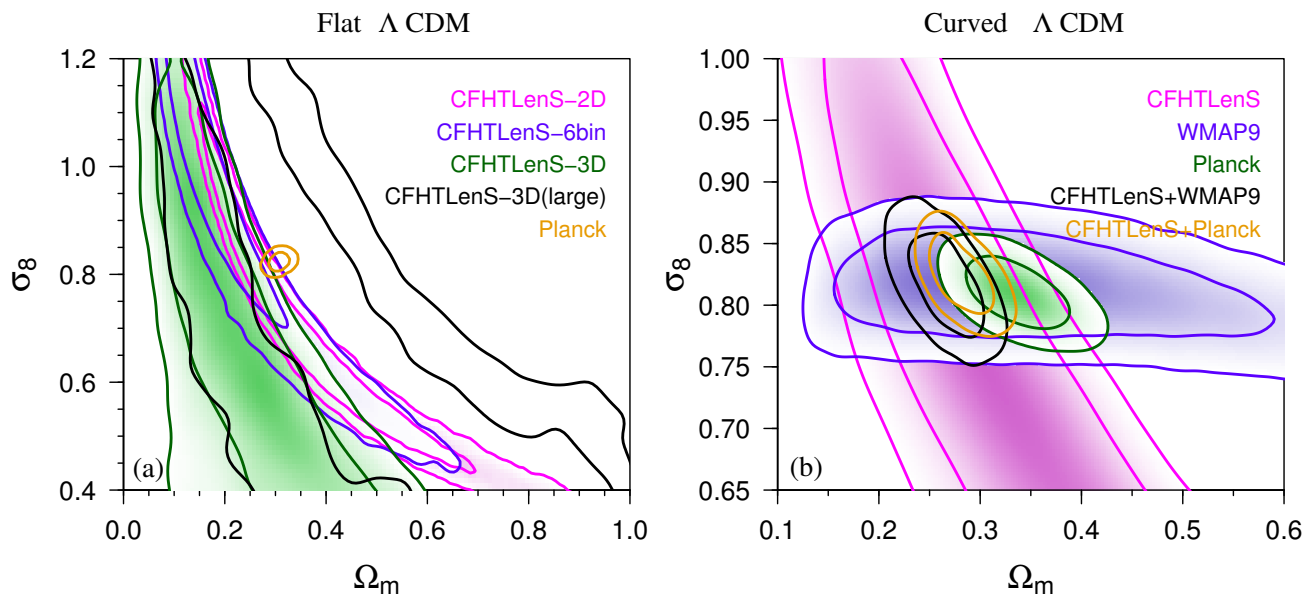


Figure 9. Cosmic shear and CMB 68.3% and 95.5% confidence levels for Ω_m and σ_8 in a Λ CDM universe. (a) Assuming flatness. CFHTLenS 2D, 6-bin tomography, 3D, and 3D from large scales only are compared to Planck constraints. (b) With free curvature, showing CFHTLenS (joint second- and third-order), WMAP9, Planck, CFHTLenS + WMAP9, and CFHTLenS + Planck constraints, from Fu et al. (2014). Figure used with permission from Fu et al. (2014), *MNRAS*, **441**, 2725. Copyright 2014 Oxford University Press.

Pole Telescope) and ACT (Atacama Cosmology Telescope) have detected weak-lensing of the CMB by large-scale structures (*CMB lensing*), which helps to break the geometrical degeneracy. This results in tight constraints on Ω_K from CMB alone (Sherwin et al. 2011, van Engelen et al. 2012, Planck Coll. 2014a). Fig. 9 shows joint cosmic shear and CMB constraints for a free-curvature model.

The dark-energy parameter of state w_0 has been measured with cosmic shear already in 2006 (Hoekstra et al. 2006, Semboloni et al. 2005). However, since the effect of dark energy on the suppression of the growth of structure is relatively small, 2D weak lensing is not very sensitive to dark energy, and 68% confidence intervals on w_0 are typically of order unity, which furthermore is degenerate with other parameters such as σ_8 . However, weak lensing can rule out some combinations of parameter values, and substantially reduce the allowed region of parameter space when combined with other probes. Fig. 10 shows how CMB constraints from WMAP7 — with an additional prior on H_0 from (Riess et al. 2011) — are reduced by CFHTLenS six-bin tomography. The parameters Ω_m and w_0 are measured to better than 10% accuracy, for both a flat and free-curvature w CDM model. The improvement is similar to adding Baryonic Acoustic Oscillation (BAO) data from the SDSS-III Baryon Oscillation Spectroscopic Survey (BOSS; Anderson et al. 2012) to CMB data.

Constraints on modified gravity using the parametrization in (7, 8) showed consistency with GR (Simpson et al. 2013). A simple model was considered where Σ and μ did not vary spatially, and at early times tend towards GR, so that deviations of GR are allowed at late times where the accelerated expansion happens. The present-day values of those two parameters were measured to be $\Sigma_0 = 0.00 \pm 0.14$, and $\mu_0 = 0.05 \pm 0.25$, combining CFHTLenS weak-lensing tomographic data (Benjamin et al. 2013), redshift-space distortions from WiggleZ (Blake et al. 2012) and 6dFGS (Beutler et al. 2012), WMAP7 CMB anisotropies from small scales, $\ell \geq 100$ (Larson et al. 2011), and the Riess et al. (2011) H_0 prior (see Fig. 11).

All measurements presented so far are based on real-space second-order shear correlations, with

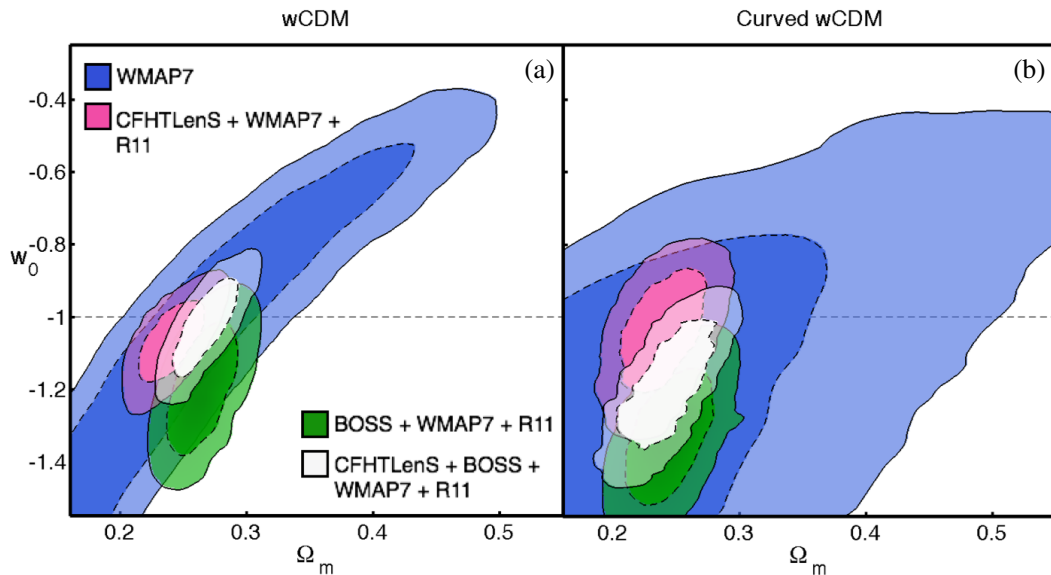


Figure 10. Combined constraints on Ω_m and w_0 from cosmic shear, CMB, and BAO. The model is a w CDM universe with flat (free) curvature in panel (a) (b). Cosmic shear is six-bin tomography from CFHTLenS. The CMB and BAO data are the same as in Fig. 8. The HST H_0 prior is replaced with an updated version (Riess et al. 2011). From Heymans et al. (2013). Figure used with permission from Heymans et al. (2013), *MNRAS*, **432**, 2249. Copyright 2013 Oxford University Press.

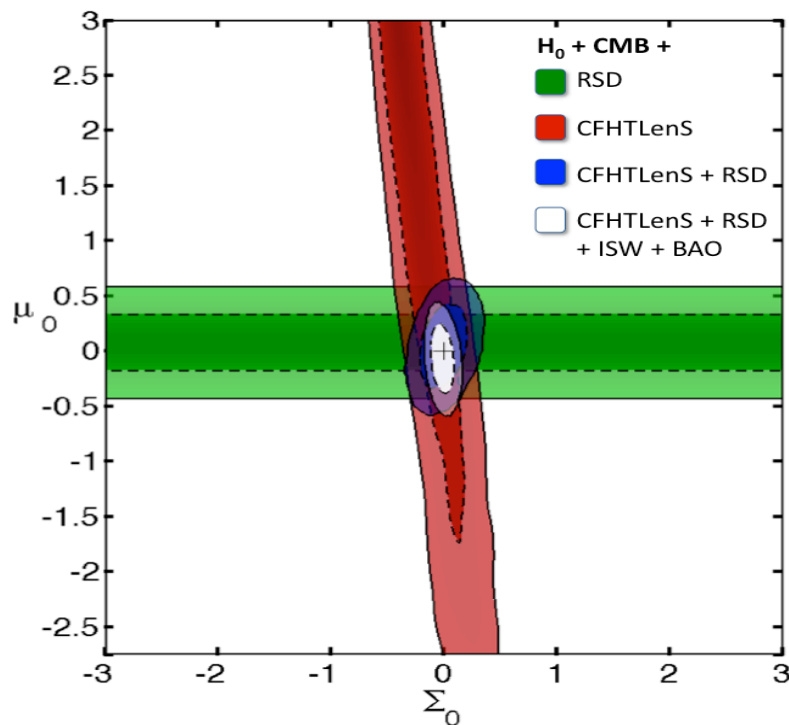


Figure 11. Combined constraints on the present-day modified-gravity parameters Σ_0 and μ_0 , from redshift-space distortions (RSD), cosmic shear (CFHTLenS), and their combination, including the case of additional BAO (Anderson et al. 2012) and large-scale WMAP7 (ISW) data. All data are combined with a H_0 prior and small-scale CMB data, see text. From Simpson et al. (2013). Figure used with permission from Simpson et al. (2013), *MNRAS*, **429**, 2249. Copyright Oxford University Press.

the exception of Brown et al. (2003) who directly estimated the shear power spectrum from the data. In the following sections, we present results from higher-order shear and other, non-traditional lensing statistics.

7.2. Third-order correlations

The motivation behind higher-order shear statistics has been argued for in Sect. 3.13. Even though the measurement is challenging and the overall signal-to-noise ratio is low, several significant detections of third-order shear correlations have been made.

The first detection of a third-order cosmic shear correlation was obtained with the VIRMOS-DESCART survey (Bernardeau et al. 2002), using a specific high signal-to-noise projection of the 3PCF (Bernardeau et al. 2003). The aperture-mass skewness $\langle M_{\text{ap}}^3 \rangle$ was measured subsequently in VIRMOS-DESCART (Pen et al. 2003) and the 75 deg² survey (Jarvis et al. 2004).

The first space-based measurement of $\langle M_{\text{ap}}^3 \rangle$ was presented in Semboloni et al. (2011*b*), based on the reanalysed HST COSMOS weak-lensing data (Schrabback et al. 2010). Their cosmological constraints were consistent with the WMAP7 best-fit cosmology.

Several higher-order measurements resulted from CFHTLenS. Van Waerbeke et al. (2013) measured the skewness of reconstructed convergence maps and found good agreement with WMAP7 predictions. After validating the data for shear residual third-order correlations, Simon et al. (2015) performed a cosmological analysis of the aperture-mass skewness exploring a non-Gaussian likelihood. Fu et al. (2014) combined the second- and third-order aperture-mass combined with WMAP9 and Planck to obtain cosmological results, including models of intrinsic alignment and source-lens clustering as astrophysical systematics.

7.3. Follow-up publications

Past cosmic shear results have been subsequently used in a large number of follow-up publications, often by people outside of the original collaboration. In many cases, these works profited from public releases of the science products of the cosmic shear survey in question. At a minimum, this includes the shear correlation function, its covariance, and the source redshift distribution. This is particularly important when new models are to be tested, for which simply using the original cosmological constraints as priors, for example the mean and error on $\Omega_{\text{m}}\sigma_8^g$ as Gaussian prior, might not be valid. In the following, we point out some outstanding results.

Using the CFHTLS-T0003 data (Fu et al. 2008), which was available on request, models of modified gravity (Sect. 2.3) were tested in Thomas et al. (2009). This work included potential systematics in the weak-lensing data (Kilbinger et al. 2009), and uncertainties on small scales to reduce the uncertainty of non-linear model predictions and baryonic physics. Further follow-up tests of modified gravity were performed using data from COSMOS (Massey et al. 2007*b*) and CFHTLS-T0003 (Zhao et al. 2010, Daniel et al. 2010, Song et al. 2011). However, those analyses did not take into account the anomalous redshift-scalings found for both surveys. Weak-lensing tomographic data have been used to test models of modified gravity, for example with the reanalysed COSMOS data (Schrabback et al. 2010) in Dossett et al. (2011), and CFHTLenS data (Benjamin et al. 2013) in Dodelson & Park (2014).

The cosmological constraints from CMB temperature anisotropies measured by the Planck satellite (Planck Coll. 2014*a*) were in slight tension with other probes. In particular, Planck found a higher power-spectrum normalisation σ_8 . Several works proposed massive neutrinos to alleviate the tension with low- z probes such as weak lensing: Massive neutrinos are still relativistic at recombination and do not significantly influence the CMB anisotropies. They become however non-relativistic at late time, and dampen the growth of structure, therefore reducing the low- z clustering power. Joint analyses including massive neutrinos from Planck and CFHTLenS weak-lensing data (Kilbinger et al. 2013) were found to improve parameter constraints with detections of non-zero neutrino masses (Battye & Moss 2014, Beutler et al. 2014), but the evidence still favors a Λ CDM

model without additional parameters for massive neutrinos (Leistedt et al. 2014). Further, one has to note that for a reliable interpretation of small-scale lensing correlations, baryonic suppression has to be accounted for, the effect of which is somewhat degenerate with massive neutrinos (Harnois-Déraps et al. 2014). Earlier constraints on neutrino masses were obtained using data from Benjamin et al. (2007) in Gong et al. (2008), and using data from Fu et al. (2008) in Tereno et al. (2009).

Galaxy-galaxy lensing has been measured with CFHTLenS source galaxies and BOSS (Sloan Digital Sky Survey III Baryon Oscillation Spectroscopic Survey) lens galaxies (More et al. 2014). The addition of galaxy number counts and galaxy clustering helped in independently constraining galaxy bias and cosmological parameters.

7.4. Convergence and mass maps

Mass maps from weak-lensing observations have been produced since the 1990s for massive galaxy clusters, to study the total matter distribution, and the relation between galaxies, hot intra-cluster gas, and dark matter (e.g. Bonnet et al. 1994, Squires et al. 1996). Reconstructing the projected mass (or related quantities such as the density or the lensing potential) in large, blind fields, where the shear is an order of magnitude smaller than for galaxy clusters, is more challenging.

Wilson et al. (2001) constructed κ maps on UH8K/CFHT data, which were correlated with galaxy light to infer mass-to-light ratios on large scales. Convergence maps from one of the DLS fields (Wittman et al. 2006) were confronted in Geller et al. (2005) with a velocity dispersion map from 10,000 galaxy spectra obtained with Hectospec/MMT (Magnum Mirror Telescope). A strong correlation between the two was found, indicating that the lensing signal was produced by groups and clusters.

Taylor et al. (2004) and Simon et al. (2012) presented a reconstruction of the 3D potential (Taylor 2001, Bacon & Taylor 2003) and 3D density (Simon et al. 2009), respectively, in the Abell 901/2 super-cluster field of COMBO-17, revealing new background structures behind A902. Auto- and cross-correlation functions between the potential and galaxy density and luminosity were found to be consistent with a halo and HOD (halo occupation distribution) modeling.

The weak-lensing measurements in COSMOS (Leauthaud et al. 2007) were transformed into a convergence map using a non-linear, wavelet-based method (Starck et al. 2006). Thanks to the wealth of multi-wavelength observations over the same sky area, the mass maps could be compared to various baryonic tracers such as stellar mass, optical and IR galaxy density, and hot gas from X-rays. Cross-correlation factors between total mass and baryons out to large scales between 0.3 and 0.5 were obtained. The redshift evolution of structures was traced by splitting the background source galaxy population into redshift bins. Finally, a full 3D reconstruction of the potential and mass was obtained using again the method of Bacon & Taylor (2003). Further 2D mass maps were obtained, with the addition of galaxy position information in COSMOS (Amara et al. 2012).

CFHTLenS convergence maps were reconstructed and analysed in Van Waerbeke et al. (2013). Moments of κ up to order five were in agreement with N -body simulations (see also Sect. 7.2). The maps were cross-correlated with stellar-mass maps, and common over- and also under-densities could well be identified.

7.5. 3D lensing

Kitching et al. (2007) applied 3D lensing as a proof of concept to two out of five fields of 0.26 deg² size each, from the COMBO-17 survey (Wolf et al. 2003). Constraints on Ω_m, σ_8 and w_0 were obtained with error bars consistent with expectations. A more refined analysis was performed on the CFHTLenS survey (Kitching et al. 2014). This included conservative cuts directly in k -space,

to limit the uncertainty of models of non-linear and baryonic physics on small scales. Cuts in k of 1 and $5 h \text{ Mpc}^{-1}$, respectively, were considered, and, for the latter, the phenomenological halo model with baryonic effects from (Semboloni et al. 2011a) was included. Constraints including small scales were in better agreement with the large-scale result when baryonic damping was taken into account. Moreover, early-type galaxies were excluded from the analysis to minimise the contamination from intrinsic alignment.

Dark-energy models beyond a constant parameter w_0 were considered as well in Kitching et al. (2014) but the resulting constraints did not represent an improvement compared to Planck + BAO.

7.6. Other weak-lensing techniques in a cosmological context

7.6.1. Shear-ratio geometry test The variation with redshift of weak gravitational shear produced by a given foreground structure depends on distances between observer, lens, and source galaxy. By taking the ratio of shears at different background redshifts, the dependence on the properties of the foreground structures at fixed redshift, even in the highly non-linear regime, cancels out. This *shear ratio test* is thus a purely geometrical probe of cosmology (Jain & Taylor 2003, Bernstein & Jain 2004, Taylor et al. 2007).

Since the shear ratio involves ratios of angular distances, which are very slowly varying functions of redshift and cosmology, it is a relatively insensitive probe. Even though shear enters in linear order in the background shear - foreground position correlations, and, similar to galaxy-galaxy lensing (Sect. 3.12) and peak counts (Sect. 8.6) many PSF residuals may cancel from circular averaging, this method is all the more sensitive to redshift-dependent systematics, e.g. in the measured shapes. Further, the quality of photometric redshifts must be excellent not to dilute the shear ratio.

Kitching et al. (2007) obtained cosmological constraints using the shear ratio behind three massive Abell clusters at $z = 0.165$ in the A901/A902 super-cluster field, observed with COMBO-17. Taylor et al. (2012) measured the shear-ratio from 129 COSMOS groups for a source galaxy sample for which redshifts were as accurate as $\sigma_z = 0.018(1 + z)$, at a very high mean redshift of $\bar{z} = 0.95$.

7.6.2. Galaxy-galaxy lensing Cosmological results from GGL have been obtained by combining GGL and galaxy clustering. The ratio of combinations of those observables measures the ratio b/r of the bias and correlation coefficient between galaxies and total matter (Van Waerbeke 1998, Schneider 1998). This has been measured early on with RCS (Hoekstra et al. 2001). Cosmic shear adds an additional observable to allow for an independent measure of both b and r , with only little dependence on cosmology (Fan 2003). However, it also sets more stringent demands on image quality, and is more prone to systematics. Using all three observables, b and r have been measured as functions of scale and redshift in RCS+VIMOS-DESCART (Hoekstra et al. 2002a), GaBoDS (Simon et al. 2007), and COSMOS (Jullo et al. 2012).

Third-order correlations between mass and galaxies (*galaxy-galaxy-galaxy lensing*), introduced in Schneider & Watts (2005), has been measured in Simon et al. (2013). This technique allows to quantify the excess mass around pairs of galaxies, probing the joint environment of correlated galaxies.

Baldauf et al. (2010) introduced an estimator of clustering and GGL that removes small scales, retaining only information on mass coming from an annulus. This leads to a measure that is not sensitive to the non-linearity and stochasticity of bias. Mandelbaum et al. (2013) applied this method to SDSS data and, by marginalising over non-linear bias parameters, obtained results $\sigma_8(\Omega_m/0.25)^{0.57} = 0.80 \pm 0.05$.

Reyes et al. (2010) used the same estimator and added redshift space distortions to 2D clustering and GGL. They formed a combined quantity that is (near-)independent of cosmology and galaxy

bias, and probes relations between the Bardeen potentials (1). GR was tested and confirmed, and interesting constraints on certain types of $f(R)$ and TeVeS modified gravity theories were obtained.

7.7. Intrinsic alignment

To measure intrinsic alignment, one can use a galaxy sample for which GG is a subdominant contribution compared to GI or II (Sect. 3.11). This can be a very shallow survey where GI is the dominant signal, or a very narrow redshift bin for which II is large. Other techniques consist of nulling out GG (Joachimi & Schneider 2008, Joachimi & Schneider 2009), or a joint measurement of $GG + GI + II$ together with a joint model-fitting of the three components (King 2005). Additional observations of galaxy-galaxy lensing and galaxy clustering helps to separate the different components (Joachimi & Bridle 2010, Zhang 2010).

II has been measured early on using digitized photographic plates from the very shallow 10,000 deg² SuperCOSMOS survey (Brown et al. 2002), by noting an order-of-magnitude excess of shape correlations compared to cosmic shear predictions at low redshift. In a more model-independent way, II has been detected from physically close pairs in COMBO-17 with its very accurate redshifts (Heymans et al. 2004).

A further method to estimate GI is the measurement of the correlation between intrinsic ellipticity ε^s and galaxy number density. This can be achieved by correlating two galaxy samples with overlapping redshift ranges, one of which has shape information, and which can be a sub-set of the full sample. Knowing the galaxy bias, e.g. from measuring the galaxy spatial correlation function, one can relate this correlation to the intrinsic shear – density correlation. Using a model of intrinsic alignment to infer ε^s in terms of the density (Hirata & Seljak 2004), one then writes the observed correlation in terms of the density power spectrum.

This correlation has been measured in SDSS (Hirata et al. 2004, Mandelbaum et al. 2006a, Hirata et al. 2007, Okumura & Jing 2009, Joachimi et al. 2011a, Blazek et al. 2012) and Wiggle-Z (Mandelbaum et al. 2011), both from spectroscopic and photometric redshift samples. Significant signals have been obtained for luminous red galaxy (LRG) samples. Faint red galaxies and blue galaxies show a GI correlation consistent with zero. This is consistent with the theoretical expectation that mainly bright, central cluster galaxies are aligned with the cluster potential. IA on large, super-cluster scales is produced by the alignment of clusters with each other and with the surrounding dark matter.

A 2σ detection of intrinsic alignment from early-type galaxies was obtained by jointly fitting cosmology and the Hirata et al. (2004) linear IA model to CFHTLenS cosmic shear tomographic data (Heymans et al. 2013). Fig. 12 shows a systematic lower amplitude of shear correlation for cross-redshift correlations compared to the cosmic-shear prediction, as expected from a negative GI contribution. No detection was found for the late-type sample.

Satellite galaxies are expected to be radially aligned towards the host cluster centre. This follows from tidal-torque interactions with the cluster potential, and has been observed in the past for a small cluster samples, e.g. Pereira & Kuhn (2005). A recent measurement using a much larger sample from SDSS (Singh et al. 2014) detects radial alignment on small scales. However, other measurements of cluster satellite galaxies are consistent with no alignment, using spectroscopic galaxies in massive clusters (Sifón et al. 2015), and photometric samples in groups and clusters (Chisari et al. 2014).

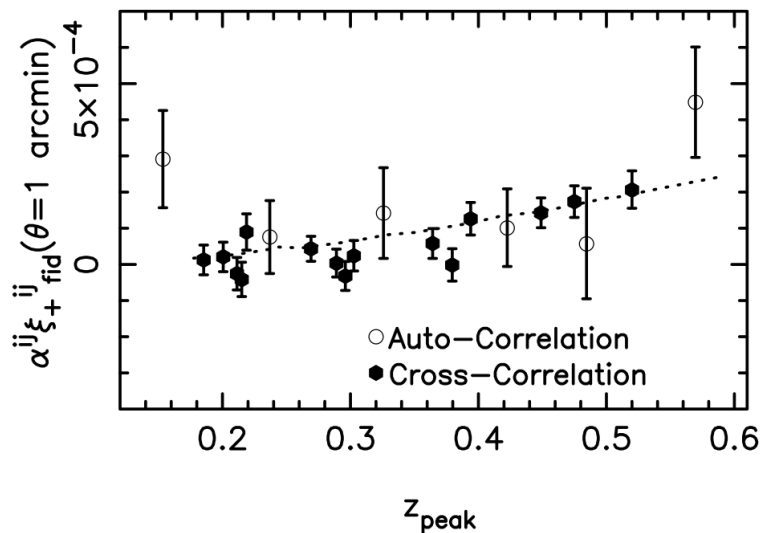


Figure 12. Amplitudes of tomographic measures of ξ_+ at $\theta = 1$ arcmin for redshift bins (ij), against peak lensing efficiency redshift z_{peak} for early-type galaxies, from CFHTLenS. The free parameters α^{ij} multiplied with a WMAP7 fiducial GG model $\xi_{+\text{fid}}$ were fitted to ξ_+ and ξ_- , simultaneous for all redshift bins and angular scales. At low z , the auto-correlations ($i = j$, open circles) lie above the fiducial dashed line ($\alpha^{ij} = 1$), as expected for a $II > 0$ contribution. The cross-correlations ($i \neq j$, filled circles) lie systematically below the prediction, indicating a $GI < 0$ contamination. From Heymans et al. (2013). Figure used with permission from Heymans et al. (2013), *MNRAS*, **432**, 2433. Copyright Oxford University Press.

8. Future cosmic shear expectations and forecasts

8.1. Upcoming and future surveys

New instruments, either cameras, telescopes, or both, are being designed and built specifically for the purpose of weak-lensing observations. Their design is driven by the goal to provide superb image quality with very small, uniform, and well-understood image distortions. The pixel scale is chosen to sufficiently sample the PSF. In view of the enormous costs of new experiments, in particular space missions, the instruments have to be thoroughly and carefully designed to guarantee the desired scientific outcome, for example, the measurement of dark-energy properties with a given accuracy.

An instrument designed for weak lensing allows at the same time pursuing other scientific goals, for example the search for exoplanets via micro-lensing (Gould 2010), or supernovae surveys, with the caveat that detecting transient objects requires a specific survey strategy that is most likely not optimal for weak lensing. Further cosmological probes and techniques can be explored using photometric redshifts from a weak-lensing survey such as galaxy clustering, galaxy clusters, and strong lensing. Last but not least, a lensing survey offers a huge legacy value, providing high-resolution multi-band images of galaxies at high redshift.

8.1.1. Ground-based surveys An order-of-magnitude increase in area compared to current surveys is being undertaken since 2012 by the Kilo Degree Survey (KiDS; de Jong et al. 2013). 1,500 square degrees are being mapped with the recently commissioned wide-field camera OmegaCAM on VST (VLT Survey Telescope). Four optical bands are complemented by five deep IR bands observed at VISTA (Visible and Infrared Survey Telescope for Astronomy) within the survey VIKING (VISTA Kilo-degree Infrared Galaxy survey), providing excellent photometric redshifts. The VST mirror with its 2.6 m diameter is on the small side to carry out a large survey. This is however compensated by the small PSF and excellent observing conditions at the Cerro Paranal site. With a projected

limiting magnitude of $i = 24.2$ †, KiDS is shallower than CFHTLS-WIDE ($i = 24.5$). Note however that weak-lensing galaxy shapes are measured in the r band, which is observed longer and in better seeing conditions, leading to $r = 25.2$.

The Dark Energy Survey (DES; The Dark Energy Survey Collaboration 2005), started in 2013 will observe 5,000 square degrees in the South, using the newly constructed 3 deg^2 field-of-view DECam at the 4 m Blanco telescope. The seeing at Cerro Tololo is larger compared Cerro Paranal, and the planned depth of DES with $i = 24.5$ (10σ extended source) is similar to CFHTLenS. The survey area overlaps with many observations in other wavelengths, e.g. with the South Pole Telescope (SPT), and the (shallow) infrared Vista Hemisphere Survey (VHS).

A smaller area but significantly deeper limiting magnitude is provided the recently built HyperSuprimeCam (HSC) on the 8.2 m Subaru telescope. Around 1,500 square degrees with excellent image quality in multiple optical bands will be used for weak lensing, with a very high planned depth down to $i = 26$ (Miyazaki et al. 2012)‡.

These current and near-future surveys will be followed by the next generation of experiments that will cover most of the extragalactic sky of 15,000 square degrees and more. From the ground, the 8.4 m Large Synoptic Survey Telescope (LSST; LSST Science Collaboration et al. 2009) will provide extremely deep images down to $r = 28$. Since individual exposures are very short, on the order of 15 seconds to discover transient objects, they will have to be stacked or otherwise combined to do weak-lensing measurements.

8.1.2. Space-based surveys Going to space offers the two major advantages: Escaping atmospheric turbulence leads to a stable and small PSF, and infrared observations provide photo- z s to significantly higher redshifts than from the ground.

About 15,000 deg^2 will be observed from space with the ESA satellite mission Euclid (Laureijs et al. 2011). The two main science drivers for Euclid are cosmic shear and galaxy clustering, which will be observed using three instruments, an optical imager, a near-infrared imager, and a near-infrared slitless spectrograph. The optical imager on board Euclid is designed to have a very stable PSF, both spatially as well as in the time domain. To collect enough galaxy light from billions of high-redshift galaxies (30 arcmin^{-2}), the transmission curve is very broad, corresponding to the combined $R + I + z$ filters, with a required depth of $R + I + z = 24.5$. This poses new challenges to overcome, in particular galaxy colour gradients and PSF calibrations (Sect. 6.3.2). Further obstacles unique to space-based observations will have to be tackled (Cropper et al. 2013): For example, the very small PSF will be undersampled by the pixels of size 0.1 arcsec. From these undersampled stellar images, a reliable, high-resolution PSF model has to be reconstructed. Furthermore, the detector degrades with time due to the bombardment with cosmic rays, and the shapes of objects get distorted by the so-called *charge transfer inefficiency* (CTI). Corrections as function of time, position on chip, and brightness of the objects have to be applied (Massey et al. 2010, Massey et al. 2014).

A space mission proposed by NASA is WFIRST–AFTA (Wide-Field Infrared Survey Telescope – Astrophysics Focused Telescope Asset; Spergel et al. 2013). WFIRST–AFTA uses a 2.4 m mirror with near-infrared imaging and spectroscopy capabilities. Around 2,400 square degrees will be imaged for weak lensing in the near infrared, with 50 galaxies per square arcmin, corresponding to $J = 25.7$. The smaller area but higher depth compared to Euclid will probably result in a similar expected performance of WFIRST–AFTA with respect to constraining cosmological parameters. Apart from weak lensing, WFIRST–AFTA will measure galaxy clustering and SNe as cosmological

† if not stated otherwise, all limiting magnitudes quoted in this section correspond to a 5σ extended source, measured in the AB system

‡ see also the (unpublished) HSC white paper www.astro.princeton.edu/~strauss/hsc_main.pdf

probes, and exoplanets will be hunted for with microlensing and coronagraphy, using a coronagraph as additional instrument.

8.1.3. Further ideas Further non-space-based proposals have been put forward to reduce the atmospheric influence but not going into orbit. These include the balloon-borne experiment High Altitude Lensing Observatory (HALO; Rhodes et al. 2012), which can fly above 99.9% of the atmosphere, but which in turn has to solve the problem of limited flight duration and pointing stability. A further possibility is an optical/infra-red telescope at the South Pole. This site offers nearly space-based observing conditions, once the boundary layer turbulence with a height of 30 – 40 m above the ground is surpassed, with seeing as small as 0.3 arcsec at optical wavelengths (Lawrence et al. 2009). The main obstacles to a survey telescope in Antarctica are the missing infrastructure and difficult access for a ground-based facility.

8.2. Radio lensing

Weak gravitational lensing from radio wavelengths was measured for the first time in Chang et al. (2004). Shapes of galaxies were obtained using the shapelet method applied to interferometric radio data (Chang & Refregier 2002). Compared to the optical, the number density of current radio surveys is much smaller, typically by two to three orders of magnitude, leading to a very low detection significance in particular for small survey areas (Patel et al. 2010). Moreover, the redshift distribution of radio galaxies is not known accurately, making the interpretation of the measurement very challenging. However, radio weak lensing offers several advantages: PSF effects are much smaller, since there is virtually no atmospheric stochastic blurring. Well-known and stable beams of radio interferometers facilitate accurate PSF models. Furthermore, radio galaxies are typically at much higher redshifts than galaxies from wide-field optical surveys.

Future radio surveys such as the Low-Frequency Array for Radio Astronomy (LOFAR) and the Square Kilometre Array (SKA) will reach a sufficient sensitivity to resolve radio emission of ordinary galaxies and therefore provide a large number density ($\geq 100 \text{ arcmin}^{-2}$ for SKA), at a resolution corresponding to optical observations from space. Furthermore, source redshifts will be available, although not at high redshifts, from HI 21 cm line observations (e.g. Blake et al. 2004).

Observations in polarized light can help to reduce the noise due to the intrinsic ellipticity of galaxies: Gravitational lensing does not change the position angle of the polarization emission of a galaxy. Since there exists a relatively strong correlation between polarization and galaxy morphology, for example from magnetic fields that are aligned with the disk, the measurement of polarized emission is an estimator of the unlensed galaxy orientation (Brown & Battye 2011). Moreover, a prior on the unlensed orientation, together with an unpolarized shear estimator, helps to correct for intrinsic alignments.

8.3. 3D mass reconstruction

Weak-lensing reconstructions of the potential and mass distribution in three dimensions are possible albeit very challenging. Even though the 3D information is present in the shear field in the presence of photometric redshifts, the lensing kernel is very broad, which makes it difficult to estimate the redshift of the lensing structures. 3D potential or mass reconstructions from shear data are ill-posed inverse problems, and to solve them, a regularization scheme or prior has to be introduced. A commonly used regularization for linear methods is Wiener filtering (Hu & Keeton 2002, Bacon & Taylor 2003, Simon et al. 2009). This increases the signal-to-noise ratio of the reconstruction, but also introduces systematic biases by shifting and elongating the structures along the redshift direction.

These biases are general limitations of linear methods, and are also found using other regularisation schemes such as singular value decomposition (SVD; VanderPlas et al. 2011). Non-linear methods are able to significantly reduce those biases (Leonard et al. 2012*a*, Leonard et al. 2014).

A 3D mass map allows for detailed comparison between dark matter and baryonic tracers, including redshift evolution, and could serve as a direct cosmological probe of the halo mass function.

8.4. Magnification

Gravitational lensing conserves surface brightness, a consequence from Liouville's theorem which holds in any passive optical system. Since the apparent size of resolved background objects change, their flux changes as well. These two effects are manifestations of *gravitational magnification*, and can be used as weak-lensing observables in addition to the deformation (shear) of galaxy shapes.

Two competing effects are at play: Lensing not only changes the object sizes, but stretches the region of sky behind a lens, thereby on the one hand reducing the number density of source galaxies. On the other hand, for a flux-limited galaxy sample which is the case for most optical surveys, the flux of background objects are pushed above the limit, thereby increasing the local number density. Whether the first, purely geometrical dilution effect wins over the second, astrophysical effect depends on the intrinsic slope α § of the cumulative flux distribution. The larger the ratio of faint to bright objects in the sample, the steeper the distribution, and the stronger is the number density increase.

The magnification of an object is defined as the ratio of the lensed to the unlensed flux. An object's flux can be obtained by integrating over the 2D brightness distribution. The magnification μ is therefore the determinant of the inverse Jacobian \mathbf{A}^{-1} (18),

$$\mu = \det \mathbf{A}^{-1} = [(1 - \kappa)^2 - |\gamma|^2]^{-1} \approx 1 + 2\kappa; \quad (59)$$

the latter approximation holds in the limit of weak lensing.

Magnification comes for free from any weak-lensing survey, since fluxes have to be measured with high accuracy anyway, to determine photometric redshifts. The requirements on image quality are similar for measuring shapes, sizes, or fluxes.

The signal-to-noise ratio of flux magnification for an ensemble of galaxies is lower than the one for shear (Bartelmann & Schneider 2001, van Waerbeke 2010), since the former signal scales with $|\alpha - 1|$, which typically is not much larger than unity, even for very steep flux distributions. Size magnification is expected to have slightly smaller signal-to-noise ratio than shear: A parameter r describing the size of a galaxy, for example its half-light radius, scales as $r \sim 1 + \kappa$, therefore an estimator of the convergence is $\log r/r_0 \approx \kappa$, where r_0 is the unlensed size. Its intrinsic distribution has a width of $\sigma_{\log r} \approx 0.3 - 0.5$ (Shen et al. 2003), slightly higher than the intrinsic ellipticity dispersion $\sigma_\epsilon \approx 0.3 - 0.4$.

Flux measurement however can be made on galaxies that are too small or faint for accurate shape measurements, and therefore reach higher redshifts. Magnification suffers from different systematics which makes the two techniques complementary.

There are several difficulties of the measurement and interpretation of magnification compared to cosmic shear:

- Contrary to ellipticity, the expectation value of the unlensed magnitude or size does not vanish. This results in a challenge to interpret *cosmic magnification* which, analogous to cosmic shear is the correlation of galaxy magnitudes in blind fields.
- The analogue to intrinsic alignment are intrinsic magnitude and size correlations, which are caused by the clustering of galaxies. Intrinsic magnitude correlations are about a factor of 10

§ not to be confused with the deflection angle (10)

larger than IA, whereas size correlations are probably smaller (Heavens et al. 2013 and references therein).

- Non-lensing contributions to number density fluctuations are dust absorption, and crowded fields for example near cluster centres. The first contamination can be corrected for in principle by measuring a colour-dependent magnification signal (Ménard et al. 2010).

Several of the above difficulties can be mitigated by correlating background to foreground tracers of dark matter, analogous to galaxy-galaxy lensing for shear. One either correlates the background magnitude (or size) around low- z galaxies, or computes the angular number count cross-correlation function. For faint background samples, the corresponding shallow slope s causes a negative number count correlation which is a very distinct sign for gravitational magnification. In the absence of gravitational lensing, this correlation vanishes.

Due to photometric redshift errors, catastrophic outliers scatter objects between the foreground and background sample, which can produce a physical, intrinsic size and magnitude correlation that is an order of magnitude larger than the gravitational magnification. To prevent this contamination, background galaxy samples with very confident and well-controlled photometric redshifts have been employed in prior robust detections of magnification, such as Lyman Break Galaxies (LBG; Hildebrandt et al. 2009, Ford et al. 2012, Morrison et al. 2012). Other work found a magnification signal from foreground X-ray groups in COSMOS from a large background sample, however, it is unclear how strongly contaminated the measurement was from physical clustering due to photo- z errors (Schmidt et al. 2012).

8.5. Cosmic flexion

Flexion denotes the second-order distortion terms in the expansion of the lens equation (13). Whereas shear parametrizes first-order, linear distortions (18), flexion is given as third derivatives of the lensing potential. It has two (complex) components that can be written as the derivatives of the shear field. While shear gives rise to elliptical images with two-fold symmetry, the two flexion components produces images with one- and three-fold symmetry, respectively. The combined effect of shear and flexion is a skewed, arc-like image (Goldberg & Natarajan 2002, Irwin & Shmakova 2006, Goldberg & Bacon 2005, Okura et al. 2007, Schneider & Er 2008, Bacon & Schäfer 2009).

Flexion measures local changes of the shear field and is significant only on small, non-linear scales. On larger scales, cosmic flexion has a lower S/N ratio than cosmic shear (Bacon et al. 2006). For that reason, the usefulness of cosmic flexion is doubtful, since it requires models of the LSS on very small, non-linear scales. Moreover, contrary to shear, flexion is more sensitive to photon pixel noise than to the intrinsic galaxy shape dispersion. This leads to a strong increase of the measurement uncertainty towards low S/N where photon Poisson noise becomes high. It also adds to the highly non-Gaussian distribution of flexion components, which are difficult to parametrize (Rowe et al. 2013).

8.6. Peak statistics

In weak-lensing data one can identify projected over-densities by isolating regions of high convergence, or enhanced tangential shear alignments. The statistics of such weak-lensing *peaks* are a potentially powerful probe of cosmology, since peaks are sensitive to the number of halos and therefore probe the halo mass function, which strongly depends on cosmological parameters, (e.g. Kaiser 1986, Peebles et al. 1989, Evrard 1989). A *shear-selected* sample of peaks is a tracer of the total mass in halos, and does not require scaling relations between mass and luminous tracers, such as optical richness, SZ or X-ray observables.

The relation between peaks and halos is complicated because of projection and noise. Several small halos in projection or filaments along the line of sight can produce the same lensing alignment as one larger halo. Noise in the form of intrinsic galaxy ellipticities produces false detections, and alters the significance of real peaks (Schirmer et al. 2007). Because the number of halos strongly decreases with mass, noise typically results in an up-scatter of peak counts towards higher significance, which has to be carefully modeled.

Numerical simulations have shown a large potential of peak counts to constrain cosmological parameters (Kratochvil et al. 2010, Marian et al. 2012). Shear peaks single out the high-density regions of the LSS, and therefore probe the non-Gaussianity of the LSS. Despite peak counts being a non-linear probe of weak lensing, they require the measurement only to first order in the observed shear, an similar to galaxy-galaxy lensing (Sect. 3.12) this technique potentially suffers from less systematics than higher-order shear correlations. Peak counts are complementary to second-order statistics, and both probes combined are able to lift parameter degeneracies (Dietrich & Hartlap 2010, Pires et al. 2009*a*, Yang et al. 2011, Pires et al. 2012). In addition to peak counts, the two-point correlation function of lensing peaks carries cosmological information (Marian et al. 2013).

Theoretical predictions for peak counts are difficult to obtain, in particular at high signal-to-noise. Recent approaches are based on Gaussian random fields (Fan et al. 2010, Maturi et al. 2010), but more work is needed to interpret weak-lensing peak count data in a cosmological framework. A new, flexible model of peak counts is based on samples of halos drawn from the mass function, which can be generated very quickly without the need to run time-consuming N -body simulations (Lin & Kilbinger 2015).

The first measurement of weak-lensing peaks including their counts and angular correlation function was obtained in Shan et al. (2014). The observed peak counts in the CFHT/MegaCam Stripe-82 survey (CS82) were found to be in good agreement with the theoretical prediction from Fan et al. (2010). Two groups have obtained cosmological constraints from peak counts, from CFHTLenS (Liu, Petri et al. 2015) and Stripe-82 (Liu, Pan et al. 2014) data.

8.7. Outlook

In 2000, cosmic shear was first measured over a few square degrees of observed sky, from some ten thousand galaxies. Fifteen years later, surveys have increased these numbers by a factor of 100, imaging a few million galaxies over $\mathcal{O}(100)$ square degrees. Many challenges were met to analyse these data, taking years of work. This resulted in constraints on cosmological parameters that are competitive compared to other cosmological probes.

In another ten years, upcoming and future experiments will cover a substantial fraction of the entire sky, measuring billions of galaxies. This signifies yet another data volume increase of a factor of 100, not to mention the data quality improvement due to instruments dedicated to weak lensing. The formidable challenge here is reducing systematic errors to an acceptable level when analysing these large data sets. New, unprecedented difficulties have to be overcome, for example CTI for Euclid, and blended galaxy images for LSST. To fully exploit those surveys, large follow-up programs are needed to obtain the necessary large samples of photometric and spectroscopic redshifts. In addition, to interpret the results of those surveys, the accuracy of theoretical predictions of the non-linear power spectrum including baryonic physics need to be significantly improved.

If all these challenges can be overcome, weak cosmological lensing has the great potential to advance our understanding of fundamental physics. It can explore the origin of the recent accelerated expansion of the Universe, and distinguish between dark energy models and theories of modified gravity. Cosmic shear can measure initial conditions of the primordial Universe, constrain the mass of neutrinos, and measure properties of dark matter. Not only that, the study of intrinsic galaxy

alignments has provided insights into the formation and evolution of high-redshift galaxies in their dark-matter environment, proving that cosmic shear does not only probe cosmology, but influences and enriches other areas of astrophysics. Thus, over the last fifteen years, weak cosmological lensing has established itself as a major tool in understanding our Universe, and with upcoming large surveys, it will continue to be of great value for astrophysics and cosmology.

Acknowledgments

I am very grateful to Catherine Heymans, Chieh-An Lin, Peter Schneider, and Melissa Thomas for their detailed comments that helped to improve the manuscript. I would further like to thank Jean Coupon, James Jee, Fergus Simpson, and Massimo Viola for helpful discussions, and Ludo van Waerbeke for valuable contributions to early stages of this article. The comments of the two anonymous referees helped to improve the review, and I am very thankful for their diligence. Two figures in this review were generated using data that were kindly provided by Liping Fu and Tom Kitching. Several figures were taken from work published elsewhere, and I am thankful to the authors and publishers for authorizing the reproduction of the original figures.

References

- Albrecht A, Bernstein G, Cahn R, Freedman W L, Hewitt J & al. 2006 *arXiv:astro-ph/0609591* .
- Alejandro Plazas A & Bernstein G 2012 *PASP* **124**, 1113–1123.
- Amara A, Lilly S, Kováč K, Rhodes J, Massey R & al. 2012 *MNRAS* **424**, 553–563.
- Amara A & Réfrégier A 2007 *MNRAS* **381**, 1018–1026.
- Amara A, Réfrégier A & Paulin-Henriksson S 2010 *MNRAS* **404**, 926–930.
- Amendola L, Kunz M & Sapone D 2008 *JCAP* **4**, 13.
- Anderson L, Aubourg E, Bailey S, Bizyaev D, Blanton M & al. 2012 *MNRAS* **427**, 3435–3467.
- Anderson T W 2003 *An introduction to multivariate statistical analysis* third edn Wiley-Interscience.
- Andrae R, Melchior P & Jahnke K 2011 *MNRAS* **417**, 2465–2477.
- Angulo R E, Chen R, Hilbert S & Abel T 2014 *MNRAS* **444**, 2925–2937.
- Asgari M, Schneider P & Simon P 2012 *A&A* **542**, A122.
- Aubert D, Amara A & Metcalf R B 2007 *MNRAS* **376**, 113–124.
- Bacon D J, Goldberg D M, Rowe B T P & Taylor A N 2006 *MNRAS* **365**, 414–428.
- Bacon D J, Massey R J, Refregier A R & Ellis R S 2003 *MNRAS* **344**, 673–685.
- Bacon D J, Réfrégier A R & Ellis R S 2000 *MNRAS* **318**, 625–640.
- Bacon D J & Schäfer B M 2009 *MNRAS* **396**, 2167–2175.
- Bacon D J & Taylor A N 2003 *MNRAS* **344**, 1307–1326.
- Baldauf T, Smith R E, Seljak U & Mandelbaum R 2010 *Phys. Rev. D* **81**(6), 063531.
- Bardeen J M, Bond J R, Kaiser N & Szalay A S 1986 *ApJ* **304**, 15–61.
- Bartelmann M 2010 *Classical and Quantum Gravity* **27**(23), 233001–+.
- Bartelmann M & Schneider P 2001 *Phys. Rep.* **340**(4-5), 297–472.
- Battye R A & Moss A 2014 *Physical Review Letters* **112**(5), 051303.
- Becker M R 2013 *MNRAS* **435**, 115–132.
- Benabed K & Scoccimarro R 2006 *A&A* **456**, 421–432.
- Benítez N 2000 *ApJ* **536**, 571–583.
- Benjamin J, Heymans C, Semboloni E, Van Waerbeke L, Hoekstra H & al. 2007 *MNRAS* **381**, 702–712.
- Benjamin J, Van Waerbeke L, Heymans C, Kilbinger M, Erben T & al. 2013 *MNRAS* **431**, 1547–1564.
- Benjamin J, Van Waerbeke L, Ménard B & Kilbinger M 2010 *MNRAS* **408**, 1168–1180.
- Bergé J, Pcaud F, Réfrégier A, Massey R, Pierre M & al. 2008 *MNRAS* **385**, 695–707.
- Bergé J, Price S, Amara A & Rhodes J 2012 *MNRAS* **419**, 2356–2368.
- Bernardeau F 1998 *A&A* **338**, 375–382.
- Bernardeau F, Bonvin C & Vernizzi F 2010 *Phys. Rev. D* **81**(8), 083002.
- Bernardeau F, Mellier Y & Van Waerbeke L 2002 *A&A* **389**, L28–L32.
- Bernardeau F, Nishimichi T & Taruya A 2014 *MNRAS* **445**, 1526–1537.

- Bernardeau F & Schaeffer R 1992 *A&A* **255**, 1–25.
- Bernardeau F, Van Waerbeke L & Mellier Y 1997 *A&A* **322**, 1–18.
- Bernardeau F, Van Waerbeke L & Mellier Y 2003 *A&A* **397**, 405–414.
- Bernstein G & Huterer D 2010 *MNRAS* **401**, 1399–1408.
- Bernstein G & Jain B 2004 *ApJ* **600**, 17–25.
- Bernstein G M 2009 *ApJ* **695**, 652–665.
- Bernstein G M 2010 *MNRAS* **406**, 2793–2804.
- Bernstein G M & Armstrong R 2014 *MNRAS* **438**, 1880–1893.
- Bernstein G M & Jarvis M 2002 *AJ* **123**, 583–618.
- Beutler F, Blake C, Colless M, Jones D H, Staveley-Smith L & al. 2012 *MNRAS* **423**, 3430–3444.
- Beutler F, Saito S, Brownstein J R, Chuang C H, Cuesta A J & al. 2014 *MNRAS* **444**, 3501–3516.
- Blain A W 2002 *ApJ* **570**, L51–L54.
- Blake C A, Abdalla F B, Bridle S L & Rawlings S 2004 *New Astron. Rev.* **48**, 1063–1077.
- Blake C, Brough S, Colless M, Contreras C, Couch W & al. 2012 *MNRAS* **425**, 405–414.
- Blandford R & Narayan R 1986 *ApJ* **310**, 568–582.
- Blazek J, Mandelbaum R, Seljak U & Nakajima R 2012 *JCAP* **5**, 41.
- Bolzonella M, Miralles J M & Pelló R 2000 *A&A* **363**, 476–492.
- Bonnet H, Mellier Y & Fort B 1994 *ApJ* **427**, L83–L86.
- Bradač M, Schneider P, Lombardi M, Steinmetz M, Koopmans L V E & al. 2004 *A&A* **423**, 797–809.
- Bridle S, Balan S T, Bethge M, Gentile M, Harmeling S & al. 2010 *MNRAS* **405**, 2044–2061.
- Bridle S & King L 2007 *New Journal of Physics* **9**, 444–+.
- Bridle S, Shawe-Taylor J, Amara A, Applegate D, Balan S T & al. 2009 *Annals of Applied Statistics* **3**, 6–37.
- Brown M L & Battye R A 2011 *MNRAS* **410**, 2057–2074.
- Brown M L, Taylor A N, Bacon D J, Gray M E, Dye S & al. 2003 *MNRAS* **341**, 100–118.
- Brown M L, Taylor A N, Hambly N C & Dye S 2002 *MNRAS* **333**, 501–509.
- Calabrese E, de Putter R, Huterer D, Linder E V & Melchiorri A 2011 *Phys. Rev. D* **83**(2), 023011.
- Capranico F, Merkel P M & Schäfer B M 2013 *MNRAS* **435**, 194–206.
- Cardone V F, Martinelli M, Calabrese E, Galli S, Huang Z & al. 2014 *MNRAS* **439**, 202–220.
- Casertano S, Ratnatunga K U & Griffiths R E 2003 *ApJ* **598**, L71–L74.
- Castro P G, Heavens A F & Kitching T D 2005 *Phys. Rev. D* **72**(2), 023516.
- Catelan P, Kamionkowski M & Blandford R D 2001 *MNRAS* **320**, L7–L13.
- Chang C, Kahn S M, Jernigan J G, Peterson J R, AlSayyad Y & al. 2013 *MNRAS* **428**, 2695–2713.
- Chang T C & Refregier A 2002 *ApJ* **570**, 447–456.
- Chang T C, Refregier A & Helfand D J 2004 *ApJ* **617**, 794–810.
- Chevallier M & Polarski D 2001 *International Journal of Modern Physics D* **10**, 213–223.
- Chisari N E, Mandelbaum R, Strauss M A, Huff E M & Bahcall N A 2014 *MNRAS* **445**, 726–748.
- Clifton T, Ferreira P G, Padilla A & Skordis C 2012 *Phys. Rep.* **513**, 1–189.
- Codis S, Gavazzi R, Dubois Y, Pichon C, Benabed K & al. 2015 *MNRAS* **448**, 3391–3404.
- Coles P & Lucchin F 1996 *Cosmology: The Origin and Evolution of Cosmic Structure* John Wiley & Sons.
- Collister A A & Lahav O 2004 *PASP* **116**, 345–351.
- Contaldi C R, Hoekstra H & Lewis A 2003 *Physical Review Letters* **90**(22), 221303/1–4.
- Cooray A & Hu W 2001 *ApJ* **548**, 7–18.
- Cooray A & Sheth R 2002 *Phys. Rep.* **372**, 1–129.
- Crittenden R G, Natarajan P, Pen U L & Theuns T 2001 *ApJ* **559**, 552–571.
- Crittenden R G, Natarajan P, Pen U L & Theuns T 2002 *ApJ* **568**, 20–27.
- Croft R A C & Metzler C A 2000 *ApJ* **545**, 561–571.
- Cropper M, Hoekstra H, Kitching T, Massey R, Amiaux J & al. 2013 *MNRAS* **431**, 3103–3126.
- Cypriano E S, Amara A, Voigt L M, Bridle S L, Abdalla F B & al. 2010 *MNRAS* **405**, 494–502.
- Daniel S F, Linder E V, Smith T L, Caldwell R R, Cooray A & al. 2010 *Phys. Rev. D* **81**(12), 123508–+.
- Das S & Bode P 2008 *ApJ* **682**, 1–13.
- de Felice A & Tsujikawa S 2010 *Living Reviews in Relativity* **13**, 3.
- de Jong J T A, Verdoes Kleijn G A, Kuijken K H & Valentijn E A 2013 *Experimental Astronomy* **35**, 25–44.
- Dietrich J P & Hartlap J 2010 *MNRAS* **402**, 1049–1058.
- Dodelson S 2003 *Modern cosmology* Amsterdam (Netherlands): Academic Press.
- Dodelson S & Park S 2014 *Phys. Rev. D* **90**(4), 043535.
- Dodelson S & Schneider M D 2013 *Phys. Rev. D* **88**(6), 063537.
- Dodelson S, Shapiro C & White M 2006 *Phys. Rev. D* **73**(2), 023009–+.
- Dodelson S & Zhang P 2005 *Phys. Rev. D* **72**(8), 083001.

- Dolag K, Borgani S, Schindler S, Diaferio A & Bykov A M 2008 *Space Sci. Rev.* **134**, 229–268.
- Dossett J N, Moldenhauer J & Ishak M 2011 *Phys. Rev. D* **84**(2), 023012.
- Dubois Y, Pichon C, Welker C, Le Borgne D, Devriendt J & al. 2014 *MNRAS* **444**, 1453–1468.
- Dvali G, Gabadadze G & Porrati M 2000 *Physics Letters B* **484**, 112–118.
- Dyson F W, Eddington A S & Davidson C 1920 *Royal Soc. of London Philosoph. Transactions Series A* **220**, 291–333.
- Eifler T 2011 *MNRAS* **418**, 536–544.
- Eifler T, Kilbinger M & Schneider P 2008 *A&A* **482**, 9–19.
- Eifler T, Schneider P & Hartlap J 2009 *A&A* **502**, 721–731.
- Eifler T, Schneider P & Krause E 2010 *A&A* **510**, A7.
- Einstein A 1916 *Annalen der Physik* **354**, 769–822.
- Eisenstein D J & Hu W 1998 *ApJ* **496**, 605.
- Erben T, Hildebrandt H, Miller L, van Waerbeke L, Heymans C & al. 2013 *MNRAS* **433**, 2545–2563.
- Evrard A E 1989 *ApJ* **341**, L71–L74.
- Fan Z 2003 *ApJ* **594**, 33–41.
- Fan Z, Shan H & Liu J 2010 *ApJ* **719**, 1408–1420.
- Fedeli C, Semboloni E, Velliscig M, Van Daalen M, Schaye J & al. 2014 *JCAP* **8**, 28.
- Feroz F & Hobson M P 2008 *MNRAS* **384**, 449–463.
- Ford J, Hildebrandt H, Van Waerbeke L, Leauthaud A, Capak P & al. 2012 *ApJ* **754**, 143.
- Fosalba P, Gaztañaga E, Castander F J & Manera M 2008 *MNRAS* **391**, 435–446.
- Fu L 2008 Very weak lensing in the CFHTLS Wide: Cosmology from cosmic shear in the linear régime PhD thesis
Université Pierre et Marie Curie (Paris VI).
- Fu L & Kilbinger M 2010 *MNRAS* **401**, 1264–1274.
- Fu L, Kilbinger M, Erben T, Heymans C, Hildebrandt H & al. 2014 *MNRAS* **441**, 2725–2743.
- Fu L, Semboloni E, Hoekstra H, Kilbinger M, Van Waerbeke L & al. 2008 *A&A* **479**, 9–25.
- Geller M J, Dell’Antonio I P, Kurtz M J, Ramella M, Fabricant D G & al. 2005 *ApJ* **635**, L125–L128.
- Gentile M, Courbin F & Meylan G 2012 *arXiv:1211.4847*.
- Gentile M, Courbin F & Meylan G 2013 *A&A* **549**, A1.
- Giannantonio T, Porciani C, Carron J, Amara A & Pillepich A 2012 *MNRAS* **422**, 2854–2877.
- Goldberg D M & Bacon D J 2005 *ApJ* **619**, 741–748.
- Goldberg D M & Natarajan P 2002 *ApJ* **564**, 65–72.
- Gong Y, Zhang T J, Lan T & Chen X L 2008 *arXiv:0810.3572*.
- Gould A 2010 *arXiv:1010.0002*.
- Guzik J, Jain B & Takada M 2010 *Phys. Rev. D* **81**, 023503.
- Hahn O, Teyssier R & Carollo C M 2010 *MNRAS* **405**, 274–290.
- Hamana T 2001 *MNRAS* **326**, 326–332.
- Hamana T, Colombi S T, Thion A, Devriendt J E G T, Mellier Y & al. 2002 *MNRAS* **330**, 365–377.
- Hamana T, Miyazaki S, Okura Y, Okamura T & Futamase T 2013 *PASJ* **65**, 104.
- Hamana T, Miyazaki S, Shimasaku K, Furusawa H, Doi M & al. 2003 *ApJ* **597**, 98–110.
- Hamilton A J S 2000 *MNRAS* **312**, 257–284.
- Hamilton A J S, Rimes C D & Scoccimarro R 2006 *MNRAS* **371**, 1188–1204.
- Hämmerle H, Miralles J M, Schneider P, Erben T, Fosbury R A E & al. 2002 *A&A* **385**, 743–760.
- Harnois-Déraps J, van Waerbeke L, Viola M & Heymans C 2014 *arXiv:1407.4301*.
- Hartlap J, Hilbert S, Schneider P & Hildebrandt H 2011 *A&A* **528**, A51.
- Hartlap J, Schrabback T, Simon P & Schneider P 2009 *A&A* **504**, 689–703.
- Hartlap J, Simon P & Schneider P 2007 *A&A* **464**, 399–404.
- Harvey D, Kitching T D, Noah-Vanhoucke J, Hamner B, Salimans T & al. 2014 *Astronomy and Computing* **5**, 35–44.
- Hearin A P, Zentner A R, Ma Z & Huterer D 2010 *ApJ* **720**, 1351–1369.
- Heavens A 2003 *MNRAS* **343**, 1327–1334.
- Heavens A, Alsing J & Jaffe A H 2013 *MNRAS* **433**, L6–L10.
- Heavens A, Réfrégier A & Heymans C 2000 *MNRAS* **319**, 649–656.
- Heitmann K, Higdon D, White M, Habib S, Williams B J & al. 2009 *ApJ* **705**, 156–174.
- Heitmann K, Lawrence E, Kwan J, Habib S & Higdon D 2014 *ApJ* **780**, 111.
- Hettterscheidt M, Simon P, Schirmer M, Hildebrandt H, Schrabback T & al. 2007 *A&A* **468**, 859–876.
- Heymans C, Brown M, Heavens A, Meisenheimer K, Taylor A & al. 2004 *MNRAS* **347**, 895–908.
- Heymans C, Brown M L, Barden M, Caldwell J A R, Jahnke K & al. 2005 *MNRAS* **361**, 160–176.
- Heymans C, Grocutt E, Heavens A, Kilbinger M, Kitching T D & al. 2013 *MNRAS* **432**, 2433–2453.
- Heymans C & Heavens A 2003 *A&A* **339**, 711.
- Heymans C, Van Waerbeke L, Bacon D, Berge J, Bernstein G & al. 2006 *MNRAS* **368**, 1323–1339.

- Heymans C, Van Waerbeke L, Miller L, Erben T, Hildebrandt H & al. 2012 *MNRAS* **427**, 146–166.
- Hilbert S, Hartlap J & Schneider P 2011 *A&A* **536**, A85.
- Hilbert S, Hartlap J, White S D M & Schneider P 2009 *A&A* **499**, 31–43.
- Hilbert S, Marian L, Smith R E & Desjacques V 2012 *MNRAS* **426**, 2870–2888.
- Hildebrandt H, Erben T, Kuijken K, Van Waerbeke L, Heymans C & al. 2012 *MNRAS* **421**, 2355–2367.
- Hildebrandt H, van Waerbeke L & Erben T 2009 *A&A* **507**, 683–691.
- Hinshaw G, Larson D, Komatsu E, Spergel D N, Bennett C L & al. 2013 *ApJS* **208**, 19.
- Hirata C M, Mandelbaum R, Ishak M, Seljak U, Nichol R & al. 2007 *MNRAS* **381**, 1197–1218.
- Hirata C M, Mandelbaum R, Seljak U, Guzik J, Padmanabhan N & al. 2004 *MNRAS* **353**, 529–549.
- Hirata C M & Seljak U 2004 *Phys. Rev. D* **70**(6), 063526–+.
- Hivon E, Górski K M, Netterfield C B, Crill B P, Prunet S & al. 2002 *ApJ* **567**, 2–17.
- Hoekstra H 2004 *MNRAS* **347**, 1337–1344.
- Hoekstra H, Franx M, Kuijken K & Squires G 1998 *ApJ* **504**, 636.
- Hoekstra H & Jain B 2008 *Annual Review of Nuclear and Particle Science* **58**, 99–123.
- Hoekstra H, Mellier Y, Van Waerbeke L, Semboloni E, Fu L & al. 2006 *ApJ* **647**, 116–127.
- Hoekstra H, van Waerbeke L, Gladders M D, Mellier Y & Yee H K C 2002a *ApJ* **577**, 604–614.
- Hoekstra H, Yee H K C & Gladders M D 2001 *ApJ* **558**, L11–L14.
- Hoekstra H, Yee H K C & Gladders M D 2002b *ApJ* **577**, 595–603.
- Hoekstra H, Yee H K C, Gladders M D, Barrientos L F, Hall P B & al. 2002c *ApJ* **572**, 55–65.
- Hu W 1998 *ApJ* **506**, 485–494.
- Hu W 1999 *ApJ* **522**, L21–L24.
- Hu W & Keeton C R 2002 *Phys. Rev. D* **66**(6), 063506.
- Hu W & White M 2001 *ApJ* **554**, 67–73.
- Huff E M, Eifler T, Hirata C M, Mandelbaum R, Schlegel D & al. 2014a *MNRAS* **440**, 1322–1344.
- Huff E M, Hirata C M, Mandelbaum R, Schlegel D, Seljak U & al. 2014b *MNRAS* **440**, 1296–1321.
- Huff E M, Krause E, Eifler T, George M R & Schlegel D 2013 *arXiv:1311.1489* .
- Huterer D & Takada M 2005 *Astroparticle Physics* **23**, 369–376.
- Huterer D, Takada M, Bernstein G & Jain B 2006 *MNRAS* **366**, 101–114.
- Huterer D & White M 2005 *Phys. Rev. D* **72**(4), 043002–+.
- Ilbert O, Arnouts S, McCracken H J, Bolzonella M, Bertin E & al. 2006 *A&A* **457**, 841–856.
- Ilbert O, Capak P, Salvato M, Aussel H, McCracken H J & al. 2009 *ApJ* **690**, 1236–1249.
- Irwin J & Shmakova M 2006 *ApJ* **645**, 17–43.
- Jain B, Connolly A & Takada M 2007 *JCAP* **3**, 13.
- Jain B & Seljak U 1997 *ApJ* **484**, 560.
- Jain B, Seljak U & White S 2000 *A&A* **530**, 547.
- Jain B & Taylor A 2003 *Phys. Rev. Lett.* **91**, 141302.
- Jain B & Zhang P 2008 *Phys. Rev. D* **78**(6), 063503.
- Jarvis M, Bernstein G & Jain B 2004 *MNRAS* **352**, 338–352.
- Jarvis M, Bernstein G M, Fischer P, Smith D, Jain B & al. 2003 *AJ* **125**, 1014–1032.
- Jarvis M & Jain B 2004 *arXiv:astro-ph/0412234* .
- Jarvis M & Jain B 2008 *JCAP* **1**, 3.
- Jarvis M, Jain B, Bernstein G & Dolney D 2006 *ApJ* **644**, 71–79.
- Jarvis M, Schechter P & Jain B 2008 *arXiv:0810.0027* .
- Jee M J, Tyson J A, Schneider M D, Wittman D, Schmidt S & al. 2013 *ApJ* **765**, 74.
- Jing Y P & Suto Y 2002 *ApJ* **574**, 538–553.
- Jing Y P, Zhang P, Lin W P, Gao L & Springel V 2006 *ApJ* **640**, L119–L122.
- Joachimi B & Bridle S L 2010 *A&A* **523**, A1.
- Joachimi B, Mandelbaum R, Abdalla F B & Bridle S L 2011a *A&A* **527**, A26.
- Joachimi B & Schneider P 2008 *A&A* **488**, 829–843.
- Joachimi B & Schneider P 2009 *A&A* **507**, 105–129.
- Joachimi B, Schneider P & Eifler T 2008 *A&A* **477**, 43–54.
- Joachimi B, Taylor A N & Kiessling A 2011b *MNRAS* **418**, 145–169.
- Jullo E, Rhodes J, Kiessling A, Taylor J E, Massey R & al. 2012 *ApJ* **750**, 37.
- Kacprzak T, Bridle S, Rowe B, Voigt L, Zuntz J & al. 2014 *MNRAS* **441**, 2528–2538.
- Kaiser N 1986 *MNRAS* **222**, 323–345.
- Kaiser N 1992 *ApJ* **388**, 272–286.
- Kaiser N 1998 *ApJ* **498**, 26–42.
- Kaiser N 2000 *ApJ* **537**, 555–577.

- Kaiser N & Squires G 1993 *ApJ* **404**, 441–450.
- Kaiser N, Squires G & Broadhurst T 1995 *ApJ* **449**, 460.
- Kaiser N, Squires G, Fahlman G & Woods D 1994 in ‘Clusters of galaxies, Proceedings of the XIVth Moriond Astrophysics Meeting, Méribel, France’ p. 269.
- Kaiser N, Wilson G & Luppino G 2000 *arXiv:astro-ph/0003338* .
- Kayo I, Takada M & Jain B 2013 *MNRAS* **429**, 344–371.
- Kendall M G & Stuart A 1969 *The Advanced Theory of Statistics* Vol. II London: Griffin.
- Kiessling A, Heavens A F, Taylor A N & Joachimi B 2011 *MNRAS* **414**, 2235–2245.
- Kilbinger M, Benabed K, Guy J, Astier P, Tereno I & al. 2009 *A&A* **497**, 677–688.
- Kilbinger M, Fu L, Heymans C, Simpson F, Benjamin J & al. 2013 *MNRAS* **430**, 2200–2220.
- Kilbinger M & Schneider P 2004 *A&A* **413**, 465–476.
- Kilbinger M & Schneider P 2005 *A&A* **442**, 69–83.
- Kilbinger M, Schneider P & Eifler T 2006 *A&A* **457**, 15–19.
- Kilbinger M, Wraith D, Robert C P, Benabed K, Cappé O & al. 2010 *MNRAS* **405**, 2381–2390.
- King L J 2005 *A&A* **441**, 47–53.
- King L J & Schneider P 2002 *A&A* **396**, 411.
- King L J & Schneider P 2003 *A&A* **398**, 23.
- Kirk D, Rassat A, Host O & Bridle S 2012 *MNRAS* **424**, 1647–1657.
- Kitching T, Amara A, Gill M, Harmeling S, Heymans C & al. 2011a *Annals of Applied Statistics* **5**, 2231–2263.
- Kitching T D, Amara A, Abdalla F B, Joachimi B & Refregier A 2009 *MNRAS* **399**, 2107–2128.
- Kitching T D, Balan S T, Bridle S, Cantale N, Courbin F & al. 2012a *MNRAS* **423**, 3163–3208.
- Kitching T D, Heavens A F, Alsing J, Erben T, Heymans C & al. 2014 *MNRAS* **442**, 1326–1349.
- Kitching T D, Heavens A F & Miller L 2011b *MNRAS* **413**, 2923–2934.
- Kitching T D, Heavens A F, Taylor A N, Brown M L, Meisenheimer K & al. 2007 *MNRAS* **376**, 771–778.
- Kitching T D, Miller L, Heymans C E, Van Waerbeke L & Heavens A F 2008 *MNRAS* **390**, 149–167.
- Kitching T D, Rhodes J, Heymans C, Massey R, Liu Q & al. 2012b *arXiv:1204.4096* .
- Kitching T D, Rowe B, Gill M, Heymans C, Massey R & al. 2013 *ApJS* **205**, 12.
- Komatsu E, Dunkley J, Nolta M R, Bennett C L, Gold B & al. 2009 *ApJS* **180**, 330–376.
- Komatsu E, Smith K M, Dunkley J, Bennett C L, Gold B & al. 2011 *ApJS* **192**, 18.
- Kratochvil J M, Haiman Z & May M 2010 *Phys. Rev. D* **81**(4), 043519.
- Krause E & Hirata C M 2010 *A&A* **523**, A28.
- Krause E, Schneider P & Eifler T 2012 *MNRAS* **423**, 3011–3017.
- Kuijken K 1999 *A&A* **352**, 355–362.
- Kuijken K 2006 *A&A* **456**, 827–838.
- Larson D, Dunkley J, Hinshaw G, Komatsu E, Nolta M R & al. 2011 *ApJS* **192**, 16.
- Laureijs R, Amiaux J, Arduini S, Auguères J, Brinchmann J & al. 2011 *arXiv:1110.3193* .
- Lawrence E, Heitmann K, White M, Higdon D, Wagner C & al. 2010 *ApJ* **713**, 1322–1331.
- Lawrence J S, Ashley M C B, Bunker A, Bouwens R, Burgarella D & al. 2009 *PASA* **26**, 397–414.
- Leauthaud A, Massey R, Kneib J P, Rhodes J, Johnston D E & al. 2007 *ApJS* **172**, 219–238.
- Leistedt B, Peiris H V & Verde L 2014 *Physical Review Letters* **113**(4), 041301.
- Leonard A, Dupé F X & Starck J L 2012a *A&A* **539**, A85.
- Leonard A, Lanusse F & Starck J L 2014 *MNRAS* **440**, 1281–1294.
- Leonard A, Pires S & Starck J L 2012b *MNRAS* **423**, 3405–3412.
- Lewis A & Bridle S 2002 *Physical Review D* **66**, 103511.
- Li B, King L J, Zhao G B & Zhao H 2011 *MNRAS* **415**, 881–892.
- Li B, Zhao G B, Teyssier R & Koyama K 2012 *JCAP* **1**, 51.
- Li Y, Hu W & Takada M 2014 *Phys. Rev. D* **89**(8), 083519.
- Lima M, Cunha C E, Oyaizu H, Frieman J, Lin H & al. 2008 *MNRAS* **390**, 118–130.
- Limber D N 1953 *ApJ* **117**, 134–+.
- Lin C A & Kilbinger M 2015 *A&A* **576**, A24.
- Lin H, Dodelson S, Seo H J, Soares-Santos M, Annis J & al. 2012 *ApJ* **761**, 15.
- Linder E V 2003 *Physical Review Letters* **90**(9), 091301.
- Liu J, Petri A, Haiman Z, Hui L, Kratochvil J M & al. 2015 *Phys. Rev. D* **91**(6), 063507.
- Liu X, Pan C, Li R, Shan H, Wang Q & al. 2014 *MNRAS in press, also arXiv:1412.3683* .
- Loverde M & Afshordi N 2008 *Phys. Rev. D* **78**(12), 123506.
- LSST Science Collaboration, Abell P A, Allison J, Anderson S F, Andrew J R & al. 2009 *arXiv:0912.0201* .
- Luppino G A & Kaiser N 1997 *ApJ* **475**, 20.
- Ma Z, Hu W & Huterer D 2006 *ApJ* **636**, 21–29.

- Mackey J, White M & Kamionkowski M 2002 *MNRAS* **332**, 788–798.
- Mandelbaum R, Blake C, Bridle S, Abdalla F B, Brough S & al. 2011 *MNRAS* **410**, 844–859.
- Mandelbaum R, Hirata C M, Ishak M, Seljak U & Brinkmann J 2006a *MNRAS* **367**, 611–626.
- Mandelbaum R, Rowe B, Bosch J, Chang C, Courbin F & al. 2014 *ApJS* **212**, 5.
- Mandelbaum R, Seljak U, Kauffmann G, Hirata C M & Brinkmann J 2006b *MNRAS* **368**, 715–731.
- Mandelbaum R, Slosar A, Baldauf T, Seljak U, Hirata C M & al. 2013 *MNRAS* **432**, 1544–1575.
- Maoli R, Van Waerbeke L, Mellier Y, Schneider P, Jain B & al. 2001 *A&A* **368**, 766–775.
- Marian L, Smith R E, Hilbert S & Schneider P 2012 *MNRAS* **423**, 1711–1725.
- Marian L, Smith R E, Hilbert S & Schneider P 2013 *MNRAS* **432**, 1338–1350.
- Massey R, Heymans C, Bergé J, Bernstein G, Bridle S & al. 2007a *MNRAS* **376**, 13–38.
- Massey R, Hoekstra H, Kitching T, Rhodes J, Cropper M & al. 2013 *MNRAS* **429**, 661–678.
- Massey R & Refregier A 2005 *MNRAS* **363**, 197–210.
- Massey R, Refregier A, Bacon D J, Ellis R & Brown M L 2005 *MNRAS* **359**, 1277–1286.
- Massey R, Rhodes J, Leauthaud A, Capak P, Ellis R & al. 2007b *ApJS* **172**, 239–253.
- Massey R, Schrabback T, Cordes O, Marggraf O, Israel H & al. 2014 *MNRAS* **439**, 887–907.
- Massey R, Stoughton C, Leauthaud A, Rhodes J, Koekemoer A & al. 2010 *MNRAS* **401**, 371–384.
- Maturi M, Angrick C, Pace F & Bartelmann M 2010 *A&A* **519**, A23.
- Melchior P, Böhnert A, Lombardi M & Bartelmann M 2010 *A&A* **510**, A75.
- Melchior P, Viola M, Schäfer B M & Bartelmann M 2011 *MNRAS* **412**, 1552–1558.
- Ménard B, Scranton R, Fukugita M & Richards G 2010 *MNRAS* **405**, 1025–1039.
- Meyers J E & Burchat P R 2014 *ArXiv e-prints* .
- Miller L, Heymans C, Kitching T D, van Waerbeke L, Erben T & al. 2013 *MNRAS* **429**, 2858–2880.
- Miller L, Kitching T D, Heymans C, Heavens A F & Van Waerbeke L 2007 *MNRAS* **382**, 315–324.
- Miralda-Escude J 1991a *ApJ* **370**, 1–14.
- Miralda-Escude J 1991b *ApJ* **380**, 1–8.
- Miralles J M, Erben T, Hämmerle H, Schneider P, Freudling W & al. 2005 *A&A* **432**, 797–808.
- Miyazaki S, Komiyama Y, Nakaya H, Kamata Y, Doi Y & al. 2012 Vol. 8446 of *SPIE Conference Series*.
- Mobasher B, Capak P, Scoville N Z, Dahlen T, Salvato M & al. 2007 *ApJS* **172**, 117–131.
- More S, Miyatake H, Mandelbaum R, Takada M, Spergel D & al. 2014 *arXiv:1407.1856* .
- Morrison C B, Scranton R, Ménard B, Schmidt S J, Tyson J A & al. 2012 *MNRAS* **426**, 2489–2499.
- Munshi D & Jain B 2001 *MNRAS* **322**, 107–120.
- Munshi D, Kitching T, Heavens A & Coles P 2011 *MNRAS* **416**, 1629–1653.
- Munshi D, Valageas P, Van Waerbeke L & Heavens A 2008 *Phys. Rep.* **462**, 67–121.
- Newman J A 2008 *ApJ* **684**, 88–101.
- Ngan W, van Waerbeke L, Mahdavi A, Heymans C & Hoekstra H 2009 *MNRAS* **396**, 1211–1216.
- Okumura T & Jing Y P 2009 *ApJ* **694**, L83–L86.
- Okura Y & Futamase T 2009 *ApJ* **699**, 143–149.
- Okura Y, Umetsu K & Futamase T 2007 *ApJ* **660**, 995–1002.
- Pace F, Moscardini L, Bartelmann M, Branchini E, Dolag K & al. 2011 *MNRAS* **411**, 595–606.
- Patel P, Bacon D J, Beswick R J, Muxlow T W B & Hoyle B 2010 *MNRAS* **401**, 2572–2586.
- Peacock J A & Dodds S J 1994 *MNRAS* **267**, 1020–1034.
- Peacock J A & Dodds S J 1996 *MNRAS* **280**, L19.
- Peebles P J E 1980 *The Large-Scale Structure of the Universe* Princeton University Press.
- Peebles P J E, Daly R A & Juskiewicz R 1989 *ApJ* **347**, 563–574.
- Pen U L, Zhang T, Van Waerbeke L, Mellier Y, Zhang P & al. 2003 *ApJ* **592**, 664–673.
- Pereira M J & Kuhn J R 2005 *ApJ* **627**, L21–L24.
- Pires S & Amara A 2010 *ApJ* **723**, 1507–1511.
- Pires S, Leonard A & Starck J L 2012 *MNRAS* **423**, 983–992.
- Pires S, Starck J L, Amara A, Réfrégier A & Teyssier R 2009a *A&A* **505**, 969–979.
- Pires S, Starck J L, Amara A, Teyssier R, Réfrégier A & al. 2009b *MNRAS* **395**, 1265–1279.
- Planck Coll. 2014a *A&A* **571**, A16.
- Planck Coll. 2014b *A&A* **571**, A20.
- Planck Coll. 2015 *submitted to A&A, also arXiv:1502.01589* .
- Refregier A 2003 *MNRAS* **338**, 35–47.
- Refregier A & Bacon D 2003 *MNRAS* **338**, 48–56.
- Refregier A, Kacprzak T, Amara A, Bridle S & Rowe B 2012 *MNRAS* **425**, 1951–1957.
- Refregier A, Rhodes J & Groth E J 2002 *ApJ* **572**, L131–L134.
- Refsdal S 1970 *ApJ* **159**, 357.

- Reyes R, Mandelbaum R, Seljak U, Baldauf T, Gunn J E & al. 2010 *Nature* **464**, 256–258.
- Rhodes J, Dobke B, Booth J, Massey R, Liewer K & al. 2012 *Astroparticle Physics* **38**, 31–40.
- Rhodes J, Refregier A, Collins N R, Gardner J P, Groth E J & al. 2004 *ApJ* **605**, 29–36.
- Rhodes J, Refregier A & Groth E J 2000 *ApJ* **536**, 79–100.
- Rhodes J, Refregier A & Groth E J 2001 *ApJ* **552**, L85–L88.
- Riess A G, Macri L, Casertano S, Lampeitl H, Ferguson H C & al. 2011 *ApJ* **730**, 119.
- Riess A G, Macri L, Casertano S, Sosey M, Lampeitl H & al. 2009 *ApJ* **699**, 539–563.
- Romano A, Fu L, Giordano F, Maoli R, Martini P & al. 2010 *A&A* **514**, A88.
- Rowe B 2010 *MNRAS* **404**, 350–366.
- Rowe B, Bacon D, Massey R, Heymans C, Häußler B & al. 2013 *MNRAS* **435**, 822–844.
- Rowe B, Jarvis M, Mandelbaum R, Bernstein G M, Bosch J & al. 2014 *arXiv:1407.7676* .
- Rudd D H, Zentner A R & Kravtsov A V 2008 *ApJ* **672**, 19–32.
- Sato M, Hamana T, Takahashi R, Takada M, Yoshida N & al. 2009 *ApJ* **701**, 945–954.
- Sato M, Ichiki K & Takeuchi T T 2011a *Phys. Rev. D* **83**(2), 023501.
- Sato M & Nishimichi T 2013 *Phys. Rev. D* **87**(12), 123538.
- Sato M, Takada M, Hamana T & Matsubara T 2011b *ApJ* **734**, 76.
- Schaap W E & van de Weygaert R 2000 *A&A* **363**, L29–L32.
- Schäfer B M 2009 *International Journal of Modern Physics D* **18**, 173–222.
- Schäfer B M & Heisenberg L 2012 *MNRAS* **423**, 3445–3457.
- Schirmer M, Erben T, Hettterscheidt M & Schneider P 2007 *A&A* **462**, 875–887.
- Schmidt F, Leauthaud A, Massey R, Rhodes J, George M R & al. 2012 *ApJ* **744**, L22.
- Schmidt F, Rozo E, Dodelson S, Hui L & Sheldon E 2009a *ApJ* **702**, 593–602.
- Schmidt F, Rozo E, Dodelson S, Hui L & Sheldon E 2009b *Physical Review Letters* **103**(5), 051301–+.
- Schneider M D, Hogg D W, Marshall P J, Dawson W A, Meyers J & al. 2014 *ArXiv e-prints* .
- Schneider P 1985 *A&A* **143**, 413–420.
- Schneider P 1996 *MNRAS* **283**, 837.
- Schneider P 1998 *ApJ* **498**, 43–+.
- Schneider P, Ehlers J & Falco E E 1992 *Gravitational Lenses* Springer.
- Schneider P, Eifler T & Krause E 2010 *A&A* **520**, A116.
- Schneider P & Er X 2008 *A&A* **485**, 363–376.
- Schneider P & Hartlap J 2009 *A&A* **504**, 705–717.
- Schneider P & Kilbinger M 2007 *A&A* **462**, 841–849.
- Schneider P, Kilbinger M & Lombardi M 2005 *A&A* **431**, 9–25.
- Schneider P, Kochanek C S & Wambsganss J 2006 *Gravitational Lensing: Strong, Weak and Micro* Springer Berlin Heidelberg.
- Schneider P & Lombardi M 2003 *A&A* **397**, 809–818.
- Schneider P & Seitz C 1995 *A&A* **294**, 411–431.
- Schneider P, Van Waerbeke L, Jain B & Kruse G 1998 *MNRAS* **296**, 873–892.
- Schneider P, Van Waerbeke L, Kilbinger M & Mellier Y 2002a *A&A* **396**, 1–19.
- Schneider P, Van Waerbeke L & Mellier Y 2002b *A&A* **389**, 729–741.
- Schneider P & Watts P 2005 *A&A* **432**, 783–795.
- Schneider P & Weiss A 1988 *ApJ* **330**, 1–15.
- Schrabback T, Erben T, Simon P, Miralles J M, Schneider P & al. 2007 *A&A* **468**, 823–847.
- Schrabback T, Hartlap J, Joachimi B, Kilbinger M, Simon P & al. 2010 *A&A* **516**, A63+.
- Schulz A E 2010 *ApJ* **724**, 1305–1315.
- Scoccimarro R, Zaldarriaga M & Hui L 1999 *ApJ* **527**, 1–15.
- Scoville N, Aussel H, Brusa M, Capak P, Carollo C M & al. 2007 *ApJS* **172**, 1–8.
- Seitz C & Schneider P 1997 *A&A* **318**, 687–699.
- Seitz S & Schneider P 1996 *A&A* **305**, 383.
- Seitz S, Schneider P & Ehlers J 1994 *Classical and Quantum Gravity* **11**, 2345–2373.
- Seljak U 1998 *ApJ* **506**, 64–79.
- Semboloni E, Hoekstra H, Huang Z, Cardone V F, Cropper M & al. 2013a *MNRAS* **432**, 2385–2401.
- Semboloni E, Hoekstra H & Schaye J 2013b *MNRAS* **434**, 148–162.
- Semboloni E, Hoekstra H, Schaye J, van Daalen M P & McCarthy I G 2011a *MNRAS* **417**, 2020–2035.
- Semboloni E, Mellier Y, Van Waerbeke L, Hoekstras H, Tereno I & al. 2005 *A&A* **452**, 51–61.
- Semboloni E, Schrabback T, van Waerbeke L, Vafaei S, Hartlap J & al. 2011b *MNRAS* **410**, 143–160.
- Semboloni E, Tereno I, van Waerbeke L & Heymans C 2009 *MNRAS* **397**, 608–622.
- Semboloni E, Van Waerbeke L, Heymans C, Hamana T, Colombi S & al. 2007 *MNRAS* **375**, L6–L10.

- Seo H J, Sato M, Dodelson S, Jain B & Takada M 2011 *ApJ* **729**, L11.
- Shan H Y, Kneib J P, Comparat J, Jullo E, Charbonnier A & al. 2014 *MNRAS* **442**, 2534–2542.
- Shen S, Mo H J, White S D M, Blanton M R, Kauffmann G & al. 2003 *MNRAS* **343**, 978–994.
- Sherwin B D, Dunkley J, Das S, Appel J W, Bond J R & al. 2011 *Physical Review Letters* **107**(2), 021302.
- Shi X, Joachimi B & Schneider P 2014 *A&A* **561**, A68.
- Shi X, Schneider P & Joachimi B 2011 *A&A* **533**, A48.
- Sifón C, Hoekstra H, Cacciato M, Viola M, Köhlinger F & al. 2015 *A&A* **575**, A48.
- Simon P 2007 *A&A* **473**, 711–714.
- Simon P 2012 *A&A* **543**, A2.
- Simon P 2013 *A&A* **560**, A33.
- Simon P, Erben T, Schneider P, Heymans C, Hildebrandt H & al. 2013 *MNRAS* **430**, 2476–2498.
- Simon P, Hettterscheidt M, Schirmer M, Erben T, Schneider P & al. 2007 *A&A* **461**, 861–879.
- Simon P, Heymans C, Schrabback T, Taylor A N, Gray M E & al. 2012 *MNRAS* **419**, 998–1016.
- Simon P, King L J & Schneider P 2004 *A&A* **417**, 873–885.
- Simon P, Semboloni E, van Waerbeke L, Hoekstra H, Erben T & al. 2015 *MNRAS* **449**, 1505–1525.
- Simon P, Taylor A N & Hartlap J 2009 *MNRAS* **399**, 48–68.
- Simpson F 2006 *ApJ* **647**, L91–L94.
- Simpson F, Heymans C, Parkinson D, Blake C, Kilbinger M & al. 2013 *MNRAS* **429**, 2249–2263.
- Singh S, Mandelbaum R & More S 2014 *submitted to MNRAS*, *arXiv:1411.1755* .
- Skordis C 2009 *Classical and Quantum Gravity* **26**(14), 143001.
- Smith R E, Peacock J A, Jenkins A, White S D M, Frenk C S & al. 2003 *MNRAS* **341**, 1311–1332.
- Song Y S, Zhao G B, Bacon D, Koyama K, Nichol R C & al. 2011 *Phys. Rev. D* **84**(8), 083523.
- Soucail G, Fort B, Mellier Y & Picat J P 1987 *A&A* **172**, L14–L16.
- Spergel D, Gehrels N, Breckinridge J, Donahue M, Dressler A & al. 2013 *arXiv:1305.5422* .
- Spergel D N, Bean R, Doré O, Nolta M R, Bennett C L & al. 2007 *ApJS* **170**, 377–408.
- Squires G & Kaiser N 1996 *ApJ* **473**, 65.
- Squires G, Kaiser N, Babul A, Fahlman G, Woods D & al. 1996 *ApJ* **461**, 572.
- Starck J L, Pires S & Réfrégier A 2006 *A&A* **451**, 1139–1150.
- Sugiyama N 1995 *ApJS* **100**, 281–+.
- Sun L, Fan Z H, Tao C, Kneib J P, Jouvel S & al. 2009 *ApJ* **699**, 958–967.
- Szepietowski R M, Bacon D J, Dietrich J P, Busha M, Wechsler R & al. 2014 *MNRAS* **440**, 2191–2200.
- Takada M & Hu W 2013 *Phys. Rev. D* **87**(12), 123504.
- Takada M & Jain B 2003 *MNRAS* **340**, 580–608.
- Takada M & Jain B 2004 *MNRAS* **348**, 897–915.
- Takahashi R, Oguri M, Sato M & Hamana T 2011 *ApJ* **742**, 15.
- Takahashi R, Sato M, Nishimichi T, Taruya A & Oguri M 2012 *ApJ* **761**, 152.
- Taruya A, Takada M, Hamana T, Kayo I & Futamase T 2002 *ApJ* **571**, 638–653.
- Taylor A, Joachimi B & Kitching T 2013 *MNRAS* .
- Taylor A N 2001 *arXiv:astro-ph/0111605* .
- Taylor A N, Bacon D J, Gray M E, Wolf C, Meisenheimer K & al. 2004 *MNRAS* **353**, 1176–1196.
- Taylor A N, Kitching T D, Bacon D J & Heavens A F 2007 *MNRAS* **374**, 1377–1403.
- Taylor J E, Massey R J, Leauthaud A, George M R, Rhodes J & al. 2012 *ApJ* **749**, 127.
- Tegmark M, Taylor A & Heavens A 1997 *ApJ* **480**, 22.
- Tenneti A, Mandelbaum R, Di Matteo T, Feng Y & Khandai N 2014 *MNRAS* **441**, 470–485.
- Tereno I, Schimd C, Uzan J P, Kilbinger M, Vincent F & al. 2009 *A&A* **712**, 657–665.
- Tereno I, Semboloni E & Schrabback T 2011 *A&A* **530**, A68.
- Tewes M, Cantale N, Courbin F, Kitching T & Meylan G 2012 *A&A* **544**, A8.
- Teyssier R, Pires S, Prunet S, Aubert D, Pichon C & al. 2009 *A&A* **497**, 335–341.
- The Dark Energy Survey Collaboration 2005 *arXiv:astro-ph/0510346* .
- Thomas D B, Bruni M & Wands D 2014 *arXiv:1403.4947* .
- Thomas S A, Abdalla F B & Weller J 2009 *MNRAS* **395**, 197–209.
- Tinker J, Kravtsov A V, Klypin A, Abazajian K, Warren M & al. 2008 *ApJ* **688**, 709–728.
- Tinker J L, Robertson B E, Kravtsov A V, Klypin A, Warren M S & al. 2010 *ApJ* **724**, 878–886.
- Troxel M A & Ishak M 2014 *arXiv:1407.6990* .
- Tyson J A, Wenk R A & Valdes F 1990 *ApJ* **349**, L1–L4.
- Uzan J P 2007 *General Relativity and Gravitation* **39**, 307–342.
- Uzan J P & Bernardeau F 2001 *Phys. Rev. D* **64**(8), 083004.
- Valageas P 2014 *A&A* **561**, A53.

- van Engelen A, Keisler R, Zahn O, Aird K A, Benson B A & al. 2012 *ApJ* **756**, 142.
- Van Waerbeke L 1998 *A&A* **334**, 1–10.
- van Waerbeke L 2010 *MNRAS* **401**, 2093–2100.
- Van Waerbeke L, Benjamin J, Erben T, Heymans C, Hildebrandt H & al. 2013 *MNRAS* **433**, 3373–3388.
- Van Waerbeke L, Mellier Y, Erben T, Cuillandre J C, Bernardeau F & al. 2000 *A&A* **358**, 30–44.
- van Waerbeke L, Mellier Y & Hoekstra H 2005 *A&A* **429**, 75–84.
- Van Waerbeke L, Mellier Y, Pelló R, Pen U L, McCracken H J & al. 2002 *A&A* **393**, 369–379.
- Van Waerbeke L, Mellier Y, Radovich M, Bertin E, Dantel-Fort M & al. 2001 *A&A* **374**, 757–769.
- van Waerbeke L, Mellier Y, Schneider P, Fort B & Mathez G 1997 *A&A* **317**, 303–317.
- Van Waerbeke L, White M, Hoekstra H & Heymans C 2006 *Astroparticle Physics* **26**, 91–101.
- VanderPlas J T, Connolly A J, Jain B & Jarvis M 2011 *ApJ* **727**, 118.
- Velander M, Kuijken K & Schrabback T 2011 *MNRAS* **412**, 2665–2677.
- Viola M, Kitching T D & Joachimi B 2014 *MNRAS* **439**, 1909–1932.
- Voigt L M & Bridle S L 2010 *MNRAS* **404**, 458–467.
- Voigt L M, Bridle S L, Amara A, Cropper M, Kitching T D & al. 2012 *MNRAS* **421**, 1385–1398.
- von Soldner J G 1804 in J. E Bode, ed., ‘Berliner Astron. Jahrb.’ Vol. 29 Lange, G. A. pp. 161 – 172.
- Walsh D, Carswell R F & Weymann R J 1979 *Nature* **279**, 381–384.
- White M 2004 *Astroparticle Physics* **22**, 211–217.
- White M & Hu W 2000 *ApJ* **537**, 1–11.
- Wilking P & Schneider P 2013 *A&A* **556**, A70.
- Wilson G, Kaiser N & Luppino G A 2001 *ApJ* **556**, 601–618.
- Wittman D, Dell’Antonio I P, Hughes J P, Margoniner V E, Tyson J A & al. 2006 *ApJ* **643**, 128–143.
- Wittman D M, Tyson J A, Kirkman D, Dell’Antonio I & Bernstein G 2000 *Nature* **405**, 143–148.
- Wolf C, Meisenheimer K, Rix H W, Borch A, Dye S & al. 2003 *A&A* **401**, 73–98.
- Wolz L, Kilbinger M, Weller J & Giannantonio T 2012 *JCAP* **9**, 9.
- Wraith D, Kilbinger M, Benabed K, Cappé O, Cardoso J F & al. 2009 *Phys. Rev. D* **80**, 023507–023523.
- Wyithe J S B, Winn J N & Rusin D 2003 *ApJ* **583**, 58–66.
- Yang X, Kratochvil J M, Wang S, Lim E A, Haiman Z & al. 2011 *Phys. Rev. D* **84**(4), 043529.
- Yoo J & Watanabe Y 2012 *International Journal of Modern Physics D* **21**, 30002.
- Yu Y, Zhang P, Lin W, Cui W & Fry J N 2012 *Phys. Rev. D* **86**(2), 023515.
- Zaldarriaga M & Scoccimarro R 2003 *ApJ* **584**, 559–565.
- Zentner A R, Rudd D H & Hu W 2008 *Phys. Rev. D* **77**(4), 043507–+.
- Zhan H & Knox L 2004 *ApJ* **616**, L75–L78.
- Zhang J & Komatsu E 2011 *MNRAS* **414**, 1047–1058.
- Zhang P 2010 *ApJ* **720**, 1090–1101.
- Zhang P, Liguori M, Bean R & Dodelson S 2007 *Physical Review Letters* **99**(14), 141302.
- Zhang T J, Yuan Q & Lan T 2009 *New Astron.* **14**, 507–512.
- Zhao G, Giannantonio T, Pogosian L, Silvestri A, Bacon D J & al. 2010 *Phys. Rev. D* **81**(10), 103510–+.
- Zhytnikov V V & Nester J M 1994 *Physical Review Letters* **73**, 2950–2953.
- Zuntz J, Kacprzak T, Voigt L, Hirsch M, Rowe B & al. 2013 *MNRAS* **434**, 1604–1618.